Evaluation of a High-Pole Number Reluctance Synchronous Wind Generator Technology

Jean-Claude Baziruwiha

Thesis presented in partial fulfillment of the requirements for the degree of Master of Engineering (Electrical and Electronic) in the Faculty of Engineering at Stellenbosch University.

Supervisor: Prof M. Kamper
Department of Electrical and Electronic Engineering

December 2022

Declaration

By submitting this thesis electronically, I declare that the entirety of the work contained therein is my own, original work, that I am the sole author thereof (save to the extent explicitly otherwise stated), that reproduction and publication thereof by Stellenbosch University will not infringe any third party rights and that I have not previously in its entirety or in part submitted it for obtaining any qualification.

Date: December 2022

Abstract

Evaluation of a High-Pole Number Reluctance Synchronous Wind Generator Technology

J. C. Baziruwiha

Department of Electrical and Electronic Engineering,
University of Stellenbosch,
Private Bag X1, Matieland 7602, South Africa.

Thesis: MEng (Electrical)

December 2022

The design and performance evaluation of high pole number reluctance synchronous wind generators (RSGs) are addressed in this thesis. A double-salient non-overlap winding reluctance synchronous generator for medium-speed, geared wind generator drives is proposed as a preliminary stage in the evaluation. Due to the difficulty in achieving an acceptable power factor (above 0.5) for the 16-pole reluctance machine, a triple three-phase converter-fed reluctance synchronous wind generator is proposed as an alternative to the conventional three-phase equivalent. Finite element modelling and solution methods are used to analyze the performance, and the coordinate descent (ascent) algorithm is used for the design optimization of such a reluctance generator. The application is ideally suited for large scale fault-tolerant converter wind turbines. This work on multi three-phase RSGs, however, focuses on a small scale sub-2-kW reluctance generator as a first step in the research. When compared to the conventional three-phase reluctance synchronous wind generator, the proposed triple three-phase generator has a significant improvement in power factor and torque ripple.

Additionally, this thesis also explores the design and performance of a reluctance synchronous machine for a 5 MW medium-speed geared wind generator drive-train. As previously stated, achieving an acceptable power factor for high pole number reluctance machines is difficult. As a result, in order to address this issue in the proposed RSGs, a modular epoxy-casted rotor is proposed. Finite element modelling and multi-objective design optimization are used to analyze the performance of such a reluctance rotor synchronous generator. The torque density versus power factor Pareto front performance of the generator was determined using the design optimization approach. This approach provides important information on this rotor generator type. A power factor of 0.72 was attained for the specified generator design with its 16-pole, epoxy-casted reluctance rotor at a reasonably good torque density of 24 kNm/m^3 and efficiency of 98.8%.

Uittreksel

Evaluering van 'n Hoëpool Getal Reluctance Sinchronous Wind Generator Tegnologie

J. C. Baziruwiha

Departement Elektriese en Elektroniese Ingenieurswese,

Universiteit van Stellenbosch,

Privaatsak X1, Matieland 7602, Suid Afrika.

Tesis: MIng (Elektries)

Desember 2022

Die ontwerp en prestasie-evaluering van hoë paalgetal-onwilligheid sinchrone windopwekkers word in hierdie tesis aangespreek. 'n Dubbel-opvallende nie-oorvleueling sinchroniese kragopwekker vir kronkelweerstandigheid vir mediumspoed, geratwindopwekker dryf word voorgestel as 'n voorlopige stadium in die evaluering. As gevolg van die moeilikheid om 'n aanvaarbare arbeidsfaktor (bo 0.5) vir die 16-pool te bereik onwilligheid masjien, 'n drie-fase omsetter-gevoed onwilligheid sinchrone windgenerator word voorgestel as 'n alternatief vir die konvensionele driefase ekwivalent. Eindige element modellering en oplossingsmetodes word gebruik om te analiseer die prestasie en koördinaat afkoms (opstyg) algoritme word gebruik vir ontwerp optimering van so 'n reluksiegenerator. Die toepassing is ideaal geskik vir grootskaalse foutverdraagsame omsetter-windturbines. Hierdie werk op multi drie-fase RSG's fokus egter op 'n klein skaal sub-2-kW onwilligheid kragopwekker as 'n eerste stap in die navorsing. In vergelyking met die konvensionele drie-fase reluksie sinchrone wind kragopwekker, die voorgestelde kragopwekker het 'n aansienlike verbetering in kragfaktor en wringkragrimpeling.

Daarbenewens ondersoek hierdie tesis ook die ontwerp en uitvoering van 'n sinchroniese masjien vir 'n 5 MW mediumspoed-gerat windgenerator dryf-trein. Soos voorheen gesê, die bereiking van 'n aanvaarbare drywingsfaktor vir masjiene met 'n hoë poolgetal is moeilik. As gevolg hiervan, ten einde hierdie kwessie in die voorgestelde RSG'e aanspreek, is 'n modulêre epoksie-gegote rotor voorgestelde. Eindige element modellering en multi-objektiewe ontwerp optimering was gebruik om die werkverrigting van so 'n reluksierotor sinchronies te ontleed kragopwekker. Die wringkragdigtheid versus drywingsfaktor Pareto-voorverrigting van die kragopwekker is met behulp van die ontwerpoptimeringsbenadering bepaal. Hierdie benadering verskaf belangrike inligting oor hierdie rotor generator tipe. 'n Krag faktor van 0.72 is behaal vir die gespesifiseerde kragopwekkerontwerp met sy 16-polige, epoksie-gegote reluksierotor teen 'n redelike goeie wringkragdigtheid van 24 kNm/m^3 en doeltreffendheid van 98.8%.

Acknowledgements

I would like to take this moment to express my heartfelt gratitude to the following people:

- Prof. M. J Kamper. I have never in my life met an individual so knowledgeable yet so humble. You gave me a space to update my thinking skills and knowledge by taking me in as your student. It was an absolute pleasure and honor working with you not just as a supervisor but a father figure, a leader and a God-fearing man. At the start I was extremely nervous and scared but with time I began to understand my task and the process just became beautiful and absolutely enjoyable. Thank you and may you continue to pass on your great knowledge to the future generations.

- Special thanks to my partner, Sune Robertson. I could never be luckier to have you on my side throughout this journey. Not only did you have to put up with my almost not being home most of the time, you also had to put in your best in looking after our beautiful little man, Kai Baziruwiha. I am proud of the woman you have become but most importantly, I am proud of the woman you have the potential to become and congratulations on submitting your version of masters on time regardless of the difficulties we faced the last two years.

- I would also like to take this moment to say Huge thank you to the entire EMLAB especially Dylan Ockhuis and Lucky Dube. What a beautiful mix of different cultures and diversity. Thank you all for your contribution for you made this journey a beautiful process. May you all continue to shine and aim higher than the stars.

- Heartfelt thanks to my family and my extended family (the Robertsons) for your love, encouragement and support and believing in me to be able to carry this through. God bless you all.

- Lastly, Thank you to the man above. You have shaped me to become what I am today, but most importantly, you have given me the power, the courage and resources to equip and prepare myself for what I must become. From the hardships, nights without meals, delivering me from the horrific times in Rwanda to preparing me with sufficient faith to be where I am today. Through this journey, I had the pleasure to learn and discover the two most important days of my life. The day I was born and finally the day I finally realized ”WHY”. May you continue to shine your light on me to be able to find the courage to give back to the community and to continue to do my part to serve you my Lord.

Dedications

**********To my beautiful late paternal grandmother, Josephine, for taking up the role early on in my life and raising me as your own and teaching me to love in abundance and to continue to do good at all cost. My beautiful son, Kai Baziruwiha, for you are my reason I go to bed and wake up in the morning with purpose, with the drive, passion and will to work and be able to actively do my best to prepare and equip you with enough knowledge, resources and guidance to prepare you for this world and all its horrors for I know you shall become the best and better version of yourself.**********

Conference Papers

The research included in this thesis has been presented and some accepted but yet to be presented in various papers at conferences including the following:

1. J. C. Baziruwiha and M. J. Kamper, "Triple Three-Phase High-Pole Number Non-Overlap, Winding Reluctance Synchronous Wind Generator," in 2022 IEEE International Conference on Electrical Machines (ICEM), Spain, Valencia.

2. J. C. Baziruwiha, M. J. Kamper and S. Botha "High Pole Number Epoxy-Casted Rotor Reluctance, Synchronous Wind Generator," IEEE Energy Conversion Congress and Expo (ECCE), Detroit, Michigan, USA, 2022.

Contents

List of Figures

List of Tables

Nomenclature

Variables and functions

A_{cu}	active copper area per stator slot
$d-axis$	direct-axis variable
c	coil pitch in terms of stator slots
w_c	coil width
I_d, I_q	dq-axis currents
λ_d, λ_d	dq-axis flux linkages
L_d, L_d	dq-axis self inductance
A	electric loading
$K_{p(3)}$	end-winding coil pitch factor
$k_{e_{(pr)}}$	end-winding factor for a pr pole-pair machine
f_f	fill-factor
z	number of conductors per stator slot
n_a	number of parallel winding circuits
m	number of phases
W	number of series turns per phase
Q_s	number of stator slots
$q-axis$	quadrature-axis variable
ρ_t	resistivity of copper
J	RMS slot current density
p_r	rotor pole pairs
V_3	shape factor for rectangular shaped coils
q	slot per pole per phase
c, x and y	Steinmetz coefficients
w_t	tooth width
α	transformation angle
K_d	winding distribution factor

List of symbols

k	kilo	10^3
M	mega	10^6
m	milli	10^{-3}

SI Units Prefix

A	ampere
°	degrees
°C	degree Celsius
g	gram
H	henry
Hz	hertz
m	metres
N	newton
Ω	ohm
%	percent
r/min	revolutions per minute
s	second
T	tesla
V	volts
W	watt

Parameters/Variables with Units

l_{end}	average length of a winding end	[m]
θ	current angle	[°]
P_{conv}	conversion power	[W]
P_{cu}	copper losses	[W]
P_c	core losses	[W]
ω_e	electrical angular velocity	$[rad/s]$
T_{em}	electromechanical average torque	[Nm]
L_e	end-winding leakage inductance	[H]
λ	flux linkage	$[Wb - T]$
f_1	fundamental supply frequency	[Hz]
M_t, M_y	mass in the teeth and yoke	[Kg]
T_{max}, T_{min}	maximum and minimum torque	[Nm]
B_t, B_y	maximum flux density in the teeth and yoke	[T]
ϕ_x	power factor angle	[°]
R_s	stator winding resistance	[Ω]
R_s	stator's winding phase resistance	[Ω]
T_δ	Torque ripple	[%]
P_f	power factor	$[p.u]$
ϕ_x	power factor angle	[°]

Acronyms and abbreviations

ac	alternating current
E-RSG	epoxy-casted RSG
FEA	finite element analysis
FEM	Finite Element method
IM	induction motor
MMF	magnetomotive force
NSGA-II	Non-Sorted Genetic Algorithm
PM	permanent magnet
RSG	reluctance synchronous generator
RSM	reluctance synchronous machine
S-RSG	single three-phase winding RSG
2D	two-dimensional
T-RSG	triple three-phase winding RSG
WRSG	wound rotor synchronous generator
dq0	direct, quadrature, zero
SEMFEM	Stellenbosch University Electrical Machine Finite Element Modelling

Chapter 1

Introduction

For several generations, the utilization of coal was related to industrial development and was a key component in fueling many aspects of the economy. Regrettably, due to environmental and social evidence linking continuous greenhouse gas emission to respiratory illnesses, countries took stringent measures to control greenhouse gas emissions within the late 1900s. The ongoing scarcity of fossil fuel stocks, rigorous greenhouse gas emission restrictions, and the threat of global warming have compelled more governments to contemplate alternative renewable sources for generating power. While multiple renewable energy sources are readily accessible, solar and wind power are the preferred energy production options. Wind energy, especially, is currently the foremost popular renewable source, and measures to enhance the generation technology are continuously being explored.

1.1. Background

Globally, the overall energy demand has been increasing dramatically over the past decades. In pursuit of more sustainable and environmentally favorable solutions that address the rising demand for energy, wind energy continues to be among the preferred renewable energy solutions [1]. Despite the growth of the wind industry, researchers and engineers in this field continues to find effective solutions across every aspect of a wind turbine system, especially the wind generator.

Wind generator drivetrains operate at either low, medium or high speeds. Fig. 1.1 shows an example of a wind turbine system consisting of a medium-speed gearbox with a gear ratio of between 25 and 30, and a 16-pole reluctance synchronous generator (RSG) that is connected to the grid by means of a solid-state power converter. Medium-speed wind generators operate at speeds between 100 and 500 r/min, which results in higher pole numbers when compared to high speed drive train generators. In comparison with low-speed direct-drive and high-speed geared drives, medium-speed geared wind generator drives are found to be the best in terms of efficiency, among other factors [2].

The use of permanent magnet (PM) material in wind generators has gained wide popularity due to the high power densities and efficiencies attributed to using PMs. PM rotor generators are currently the preferred generator topology for medium-speed applications. An example of a medium-speed PM generator from industry is the Vestas 9.8 MW drive [3]. However, PM material is expensive and prone to demagnetization.

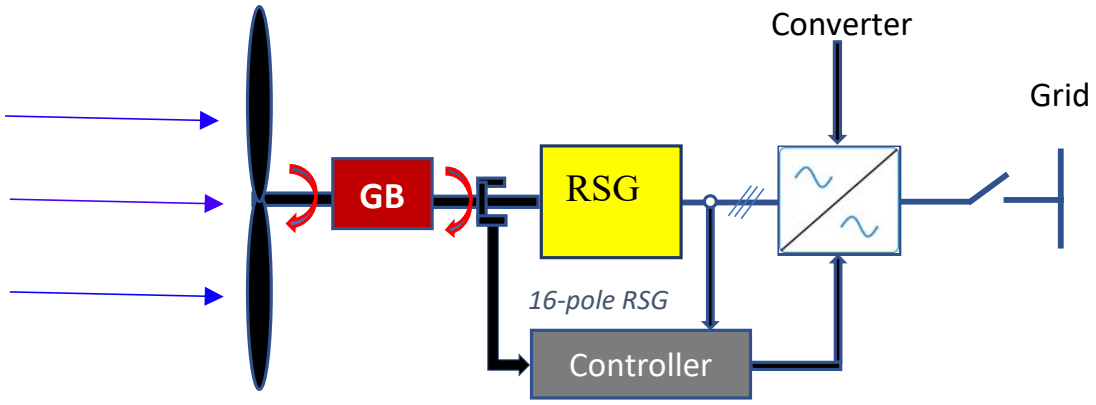

Figure (1.1) Medium-speed geared RSG wind generator drive system studied in this thesis.

Consequently, there is a need to explore non-PM generator alternatives. Among the PM-free generator alternatives, cage, wound-field, doubly-fed and reluctance-rotor generators are among the most promising solutions.

The reluctance-rotor generator is uniquely appealing because of its passive iron rotor, which does not induce additional copper losses in the rotor like the wound, doubly-fed and cage rotors [4–6]. However, reluctance machines are infamous for having poor power factor, which increases the required kVA rating and hence the cost of the power converter. Power factors for four-pole reluctance rotor machines are already poor, typically ranging from 0.7 and 0.8, and the power factor reduces even further with an increase in pole number.

1.2. Background and Operating Principles of RSMs

In this section, the basic operating concept of the reluctance synchronous machine (RSM) as well as the research works that contributed to addressing the primary design issues of the RSM are discussed. In the early 1990s, researchers began looking at RSMs again, uncovering new design issues. Important studies pertaining to the RSM architecture and design techniques are addressed by the pioneering works of [7], [8] and [9]. In particular, in [8] an RSM drive was evaluated with a brushless rare-Earth element, PM machine and an induction machine (IM). It found that RSMs have considerable promise in wind industry since they can produce a high torque density at an economical cost.

The reluctance torque, which is often referred to as the alignment torque, is caused by the forces created when a magnetic material engages with a magnetic field. Without windings or PM excitation, the RSM generates torque due to the rotor's longitudinal and transverse axes having different magnetic permeabilities. The alternating current (ac) that is flowing through the stator windings of the motor generates a revolving magnetic field in the air gap of the motor, which rotates at the synchronous speed. The rotor of the motor follows the magnetic field without actually reaching the magnetic field itself, which is why

the machine is able to produce torque continually.

Furthermore, according to the synchronous dq reference frame description of the reluctance motor, the *d-axis* is defined as the path of the least reluctance, while the *q-axis* is the path of greater reluctance as shown in Fig. 1.2. As a result, the saliency ratio, which can be seen as the ratio of the inductances along the *d*- and *q-axes*, is required to be maximized [10].

In the past, researchers have focused on three primary aspects of the RSM design problems: increasing the average torque [8, 11, 12], minimizing the torque ripple [13–15], and enhancing the power factor [14, 16], as well as comparing the RSMs to other topologies [8, 11, 17, 18].

Tradeoffs related to the RSM torque production, including the maximizing of the anisotropy, the magnetizing flux, and the q-axis current, were first made evident in [9], which highlighted the key issues of the RSM design. Several designs for both the rotor and the stator were studied. The mechanical issue linked with the rotor ribs (as shown in Fig. 1.2) was also emphasized for the first time in this study. The authors in [7] examined the influence of the angular location of the barriers at the air gap on the RSM torque ripple. The notion of the "equal pitch" rotor flux barrier distribution, as depicted in Fig. 1.3, with several iron segments, was initially proposed and investigated. Furthermore, in [19], the authors attempted to lay out a general design strategy for determining the rotor shape that would provide the lowest torque ripple.

The authors in [20] outlined what is now considered to be one of the first approaches of RSMs for optimizing rotor design. The optimization was performed with the primary goal of increasing the power factor. Furthermore, it was shown that a power factor of 0.8 is realistically attainable. Numerous variables impacting the saliency ratio were examined in [21]. It was shown that the design of the rotor, specifically the amount of flux barriers, had the most considerable influence. Even though there is a limitation to the greatest number of rotor flux barriers that may be used, increasing the number of rotor barriers to their maximum capacity does, in fact, enhance the saliency ratio (demonstrated in this thesis).

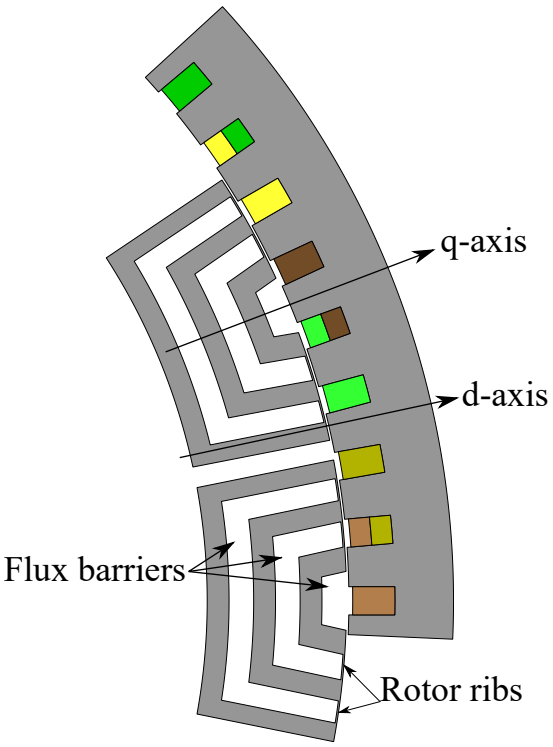

Figure (1.2) Example of a reluctance synchronous machine with flux barriers.

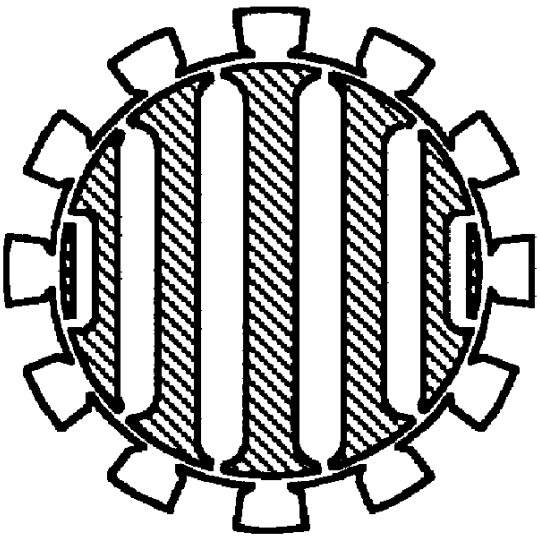

Figure (1.3) Two-pole "Equal pitch" rotor configuration. [7]

1.3. Proposed Topologies and Winding technology

In this section we consider the advantages and disadvantages of RSGs and further give a brief overview of the RSG topologies studied in this thesis. Furthermore, both winding technologies used for the proposed stator windings are given.

1.3.1. Triple Three-phase RSG

This thesis initially proposes a triple three-phase, non-overlapping winding and salient-reluctance rotor for a 16 pole, 375 r/min, sub 2-kW wind generator. The 16 pole number is a popular choice for medium-speed geared wind turbine generators. This is because 16 poles allows one to use a lower medium-speed gear ratio. Moreover, this part of the study was done for experimental, small-scale purposes and compares the performance of the proposed triple three-phase reluctance generator with that of the conventional, equivalent three-phase reluctance generator.

The triple three-phase converter-fed generator system has many advantages, including the removal of the sub- and higher-order magneto motive force (MMF) harmonics of the non-overlap stator winding. The latter has the advantage of improving the power factor, as well as the overall performance of the generator, both of which will be demonstrated later in this thesis. Moreover, the application has converter fault tolerance. If one of the

converters fails due to the current reliability issues experienced with renewable energy converters, there are two remaining. Furthermore, regarding the use of super large power applications, there is a great advantage in terms of cost to use three smaller, mass-produced converters than using one super-large converter that may not be production.

In the initial part of this thesis, we investigated the use of non-overlap windings in such a machine as shown in Fig. 1.4. Non-overlap windings are popular because of their low production costs, lower core losses, and enhanced torque density compared to overlap windings [22]. These windings are frequently used in PM machines, but technological breakthroughs have sparked interest in non-PM synchronous machines as well.

Traditional electric motors and generators make use of overlapping single- or double-layer windings, which have unity or higher slot/pole/phase, q, values, and thus more sinusoidal air-gap magnetomotive forces (MMFs). Because of the sinusoidal air-gap MMF distribution, there is improved overall machine performance.

In contrast, non-overlap windings are known for their high MMF harmonic content, which results in a non-sinusoidal air-gap MMF that reduces the performance of the machine. Recent developments in winding theory have led to the development of several techniques that minimize the harmonic content of non-overlap windings [22–27]. For example, the authors in [23] investigated the reduction of MMF harmonics with a 16/18 pole/slot combination of a 3 MW wound rotor synchronous generator (WRSG). The authors in [23] utilized a phase-shifting method based on star-delta topology as shown in Fig. 1.5. By using this technique, the coil currents were shifted by 30° electrical. The results presented provide improved overall machine performance and hence show the effect canceling the sub- and higher-order harmonics of non-overlap-winding WRSGs, especially in a 16/18 pole/slot combination.

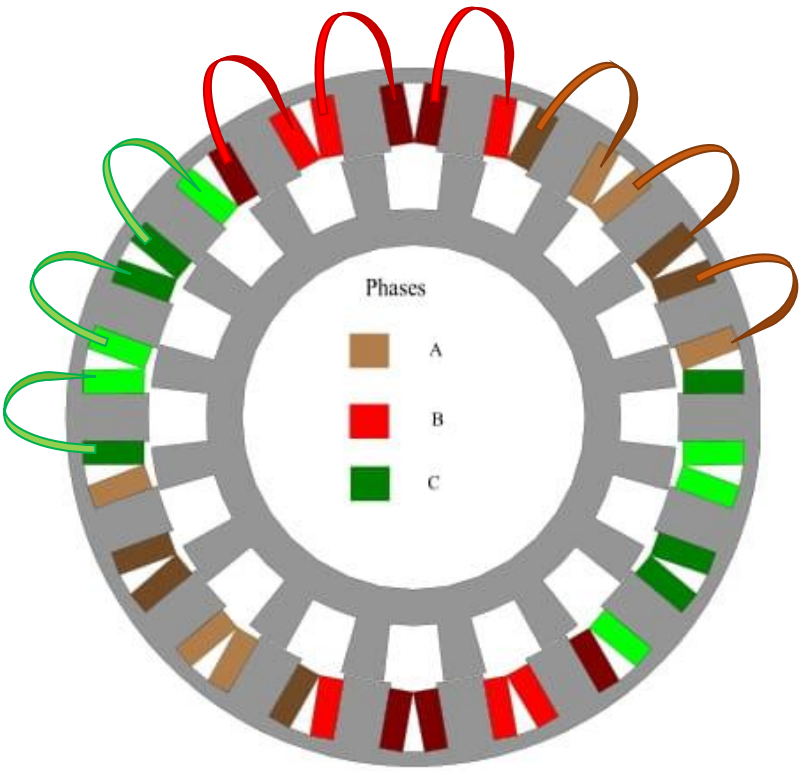

Figure (1.4) Non-overlapping winding layout of S-RSG.

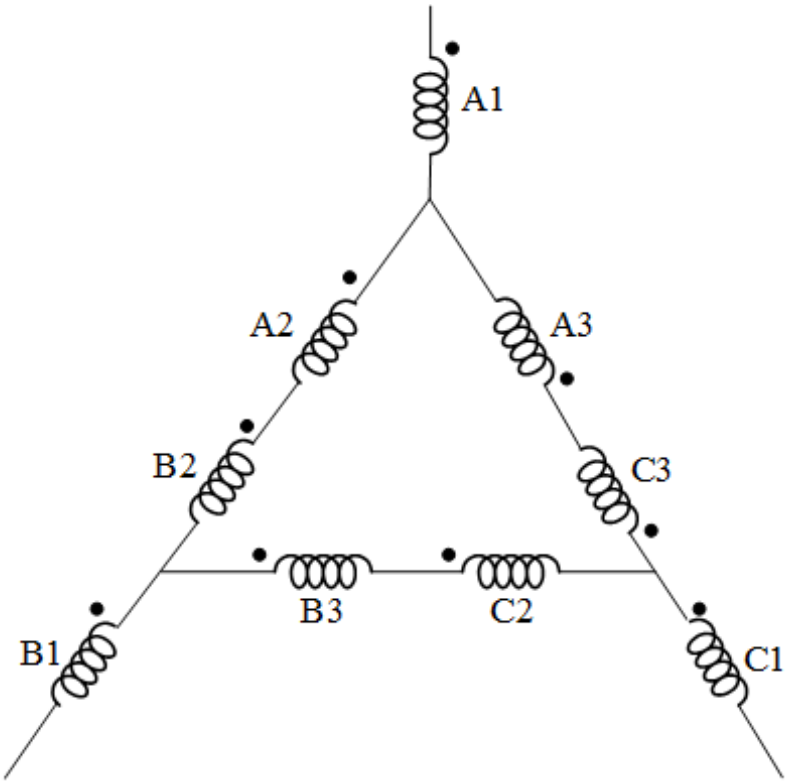

Figure (1.5) An example of a star-delta phase-shifting configuration. [23]

1.3.2. High Pole Number Epoxy-Casted Rotor Reluctance Synchronous Wind Generator

To ensure a reasonable power factor, the second part of this thesis proposes a modular epoxy-casted reluctance rotor for a 16-pole, 375 r/min, 5 MW wind generator. The 5 MW wind generator system is shown in Fig 1.1 and is described in Section 1.1. A fractional-slot stator winding was considered for the 16-pole RSG, which was shown to reduce torque ripple in RSMs [28]. Overlapping windings are known as overlap windings due to their end-winding overlapping. Moreover, when the q (slot/pole/phase) value is high, the MMF of an overlap winding has a closely sinusoidal distribution [29]. It is important to note that improving sinusoidal MMF distribution results in a reduction of some harmonic contents. The latter improves the overall machine performance. Additionally, a higher q value also implies an increased stator slot number, which demands more coils. Therefore, the higher q value is a disadvantage of overlapping windings as it has shown to raise the production unpredictability, cost of labor and an increased copper cost required [30]. Additional downsides with this winding technique include the excessive end-winding length, poor slot filling factors that translates to larger ohmic losses as well as packaging challenges and many more [22].

1.4. Problem Statement

Due to their compact size and light weight, high-speed geared wind generator drivetrains (over 500 r/min) have gained popularity in the wind industry. However, the architecture of their gearboxes is complicated and requires more than three stages [31]. Wind generator drivetrains that operate at low speeds (below 100 r/min) avoid the need for a gearbox, but at the expense of size, weight, and cost [32]. In contrast, medium-speed wind generator drivetrains (100 and 500 r/min) are gaining popularity, particularly in remote regions, due to their ability to reduce complexity and increase efficiency. The authors in [33] demonstrate how medium-speed alternatives with high pole numbers have the potential to increase yearly energy production. In spite of the fact that offshore wind generating systems have witnessed a rise in development over the years, onshore systems continue to be the more popular option.

Research concerning high pole number RSGs especially on a medium-speed range is scarce. Furthermore, there is a lack of detailed studies regarding salient-pole RSGs in the multi-three-phase, medium-speed range. The salient-pole design is easier to implement and more durable than some existing complex flux barrier rotor designs in RSGs. Moreover, the salient-pole rotor design is a far easier and more reliable design than other alternatives such as complex flux barrier rotor designs. Consequently, due to its improved mechanical strength, it has a lower probability of failing as a system and could possibly reduce the

costs associated with its production. Another question raised in this thesis is how could such a simple rotor together with an unconventional non-overlap winding configuration perform? The latter is further looked at with high-pole numbers, which, according to literature, has the potential to reduce power factor in RSGs even further. Therefore, in search for simple RSG rotor designs with increased reliability, we investigate the effect of such a simple design on a multi three-phase level. Also, in terms of reliability, there is a great advantage in reducing converter costs which will be discussed in the later sections. We further ask a question of how could such a simple design perform without altering the generator structure?

Additionally, research concerning high-pole numbers in multi-megawatt wind generator is non-existent. Therefore, with the question in mind on how does such an RSG with high-pole numbers in medium-speed range perform? Furthermore, there exist almost no literature on epoxy-casted reluctance rotors with such high-pole numbers. Therefore, we pose the question of how could such a rotor with the use of a conventional overlap stator winding perform on multi-meggawatt level. Could such a design be feasible mechanically? Also, how does such a design reduce complexity in terms of manufacturing given its already complex geometry. In order to further fill the gap in literature, we make a fair comparison to that of existing designs on the same power level and volume.

1.5. Objectives

This research considers the analysis and further evaluates the performance of a triple three-phase RSGs with high-pole number in medium-speed range. The triple three-phase reluctance rotor makes use of a non-overlapping stator winding and the results are compared to that of a conventional three-phase RSG with the same topology. Additionally, this study evaluates an epoxy-casted rotor with a conventional overlapping winding on a multi-megawatt level. As power factor and torque ripple continue to be a focus area in RSGs, various techniques that could be used to improve and address such an issue in RSGs are investigated. To evaluate the proposed RSGs, finite element analysis (FEA) is used to model the performance and design optimization of the generators. Torque ripple, efficiency, and power factor are analyzed using a 2D FEA model designed with an in-house Python-based tool (*SEMFEM*) [34] and a commercial product (*ANSYS Maxwell*). The focus of this thesis is on:

- Removal of sub- and higher-order MMF harmonics moving from conventional three-phase RSG to triple three-phase RSG.
- To design and optimize the proposed RSGs for best overall performance
- Compare the performance results of a triple three-phase RSG to that of a conventional three-phase RSG (T-RSG).

- Design and analysis of an epoxy-casted RSG on a multi-meggawatt level and compare the performance results to existing technology with the same power level and volume.

The following goals are outlined to support the primary emphasis of the study:

- Application of a coil-current phase shifting technique in the unconventional non-overlapping winding to minimize large sub- and higher order MMF harmonics.
- Design and optimize a 5-MW and sub 2-kW, 16/18 pole-slot combination with epoxy-casted rotors using multi-flux barriers.
- Core loss reduction by means of utilizing multi flux barriers.
- Torque ripple reduction techniques including rotor skewing.
- Power factor improvement by means of rotor rib slitting.
- A mechanical strength analysis is performed on the epoxy-casted rotor to prove stability of the rotor pole pieces.
- Improving power factor by means of rotor rib-slitting techniques.

1.6. Methodology

A design criterion is established for a conventional single three-phase RSG (S-RSG) with an unconventional non-overlap winding and a simple salient 16-pole rotor. Once optimized, a current phase-shifting technique is applied to the optimized three-phase RSG to obtain the triple three-phase RSG (T-RSG). The performance of the final machines are evaluated and compared. Furthermore, in an attempt to improve power factor, an epoxy-casted RSG (E-RSG) is proposed, designed and further investigated. The E-RSG makes use of a 16/18 pole/slot combination and a conventional overlap stator winding. Whilst designing the E-RSG, multiple techniques are used to obtain the best overall machine including multiple flux-barriers and rotor rib-slitting techniques. Simulations throughout the project are done using an in-house Python-based FEA package (*SEMFEM*) and verifications were further done using the commercial package, *ANSYS Maxwell*. To obtain the optimum machines, we make use of an optimization package called *VisualDoc* [35]. Furthermore, simulations are done on a sub 2-kW and the 5-MW power levels throughout this thesis. The final designs are selected based on a set criterion that best achieved the set objectives in terms of torque ripple, power factor, efficiency and output power.

1.7. Thesis Layout

The next chapters of this thesis will have the following structure:
Chapter 2 gives the overview on multi three-phase reluctance generators studied in this thesis. Furthermore, the mathematical modeling of the RSGs are given in Chapter 3. The finite element method (FEM) packages used to carry out simulations are described in Chapter 4. Chapter 5 deals with the simulations of S-RSG and T-RSG. Chapter 6 gives the design optimization used to obtain the optimum designs of the RSGs. Chapter 7 deals with the design and optimization of high pole number epoxy-casted RSG (E-RSG). Finally, Chapter 8 gives the overall conclusions and recommendations.

Chapter 2

Multi Three-phase Reluctance Generators

This thesis evaluates the performance of high pole number RSGs. We make use of two different stator winding topologies for the various 16-pole RSGs studied as explained in the previous chapter. This chapter takes a closer look at the different RSGs studied. Fig. 2.1 shows the layout of the high pole number RSGs studied with the corresponding winding topologies.

The initial part of this thesis determines and compares the overall performance of a conventional single three-phase winding RSG (S-RSG), and triple three-phase winding RSG (T-RSG) in Fig. 2.2. The corresponding coil arrangements for both S-RSG and T-RSG are shown in Figs. 2.3 and 2.4 respectively. By applying the proposed phase shifting techniques at 20°, the wye coil configuration of the S-RSG in Fig.2.3 is transformed into separate three wye coil configurations of the T-RSG in Fig. 2.4. The current phase shift angle of 20° was chosen because it generated maximum torque and further gave the optimum performance in terms of torque, torque ripple, power factor and core losses. This application results in a reduction of the sub- and higher MMF harmonics as shown in Fig. 2.5.

The second part this thesis evaluates the design and performance of a reluctance synchronous machine for a 5-MW, medium-speed geared wind generator drive-train. Since achieving an acceptable power factor for high pole number reluctance machines is challenging, a modular epoxy-casted rotor is proposed. The performance of such a reluctance rotor synchronous generator is evaluated by means of finite element modeling and multi-objective design optimization. Through the design optimization method, the torque density versus power factor Pareto front performance of the generator is determined. This provides insightful information on this type of rotor generator.

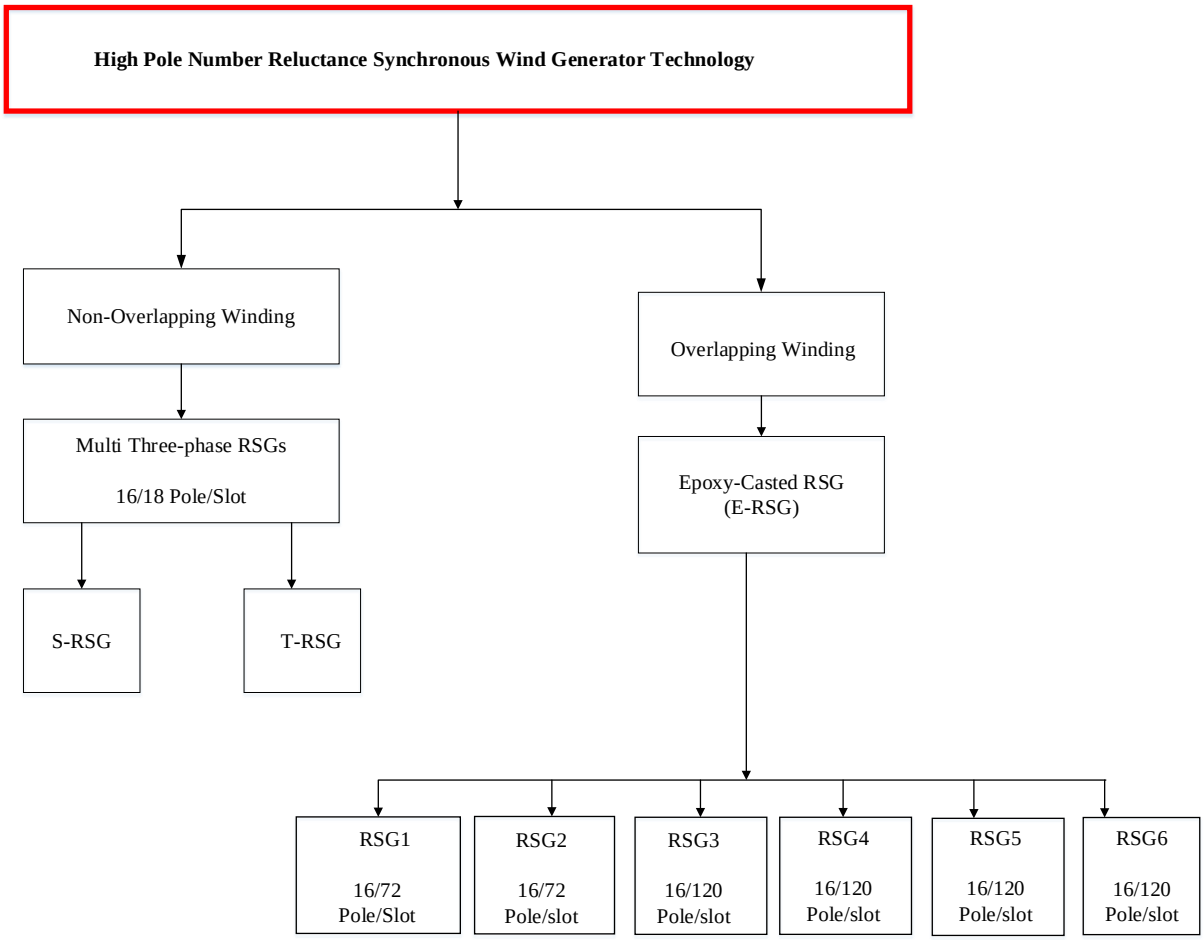

Figure (2.1) High Pole Number RSG design layout.

2.1. Conventional single three-phase RSG (S-RSG)

Fig. 2.2(a). shows the cross-section of the S-RSG studied in this thesis. Additionally, the S-RSG stator coil arrangement used is shown in Fig. 2.3. As shown in Fig. 2.2(a), the S-RSG consists of three phases A, B and C. Each phase consists of three coils connected in series and is symmetrically repeated for the complete machine.

2.2. Triple three-phase winding RSG (T-RSG)

Fig. 2.2(b) shows the cross-section of the T-RSG machine studied in this thesis. The corresponding T-RSG stator coil arrangement used is shown in Fig. 2.4. The T-RSG consists of nine (9) phases which includes phases A1, B1 and C1 up to A3, B3 and C3 as shown in Fig. 2.2(b).

Furthermore, the proposed T-RSG is composed of three three-phase windings connected in wye configuration as shown in Fig. 2.4. With this, three three-phase set of coil currents of the same magnitudes are applied at a phase shift of 20°. This results in the removal of sub- and higher order MMF harmonics as shown in Fig. 2.5. In Fig. 2.5, the per-unit

MMF harmonics versus harmonic order of the S-RSG is shown in blue. From this, the forth harmonics is the working harmonic which produces the main torque. The stator MMF includes several harmonic components in addition to the working harmonic, particularly the fifth harmonic, whose amplitude accounts for the majority of the working harmonic. Furthermore, as it can be seen in Fig. 2.5 (in blue), the first, second, thirteenth, and fourteenth harmonics with longer wavelengths have relatively high amplitudes, which has a significant impact on generator overall performance.

Another important aspect in this study is the ability of each of the triple three-phase RSG coils to maintain the same phase voltage ratings as that of the conventional three-phase RSG. This means that each of the individual coils in Fig. 2.4 has a 230 V phase voltage. This allows only a third of the supply current, (i.e., $|I_{s(S-RSG)}| = 3|I_{s(T-RSG)}|$), at each of the coils to be supplied. Moreover, the number of series turns-per-phase is then increased by a factor of 3. The advantages of having higher number of coil turns in large scale, low voltage machines are reduced coil eddy current loss and increased copper fill factors.

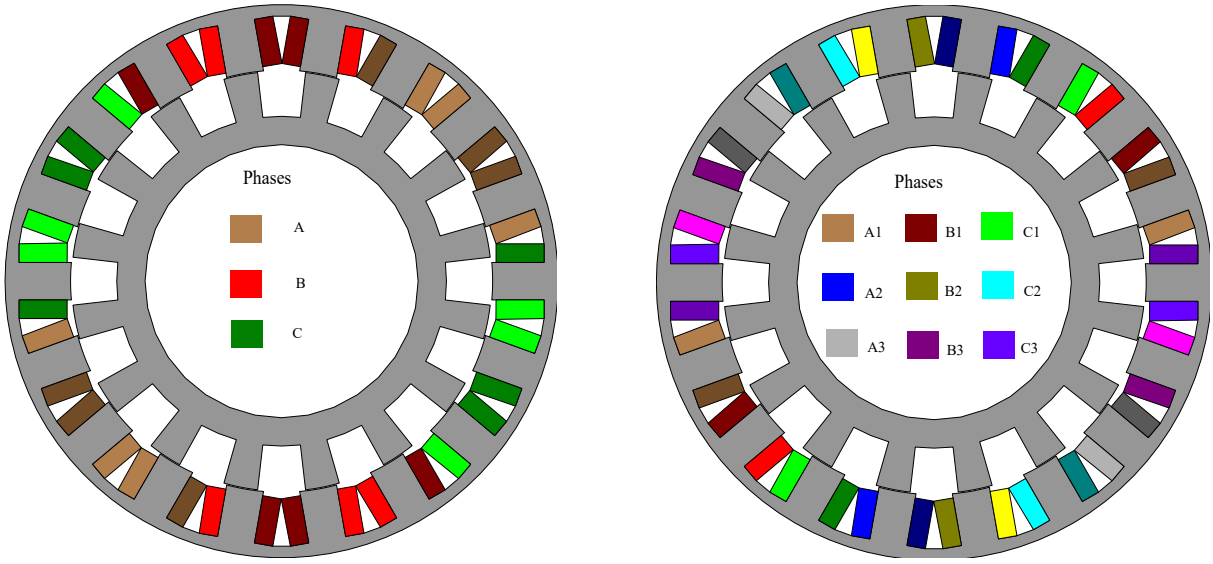

(a) (b)

Figure (2.2) Optimized salient pole RSG machines of (a) conventional single three-phase winding RSG (S-RSG) and (b) triple three-phase winding RSG (T-RSG).

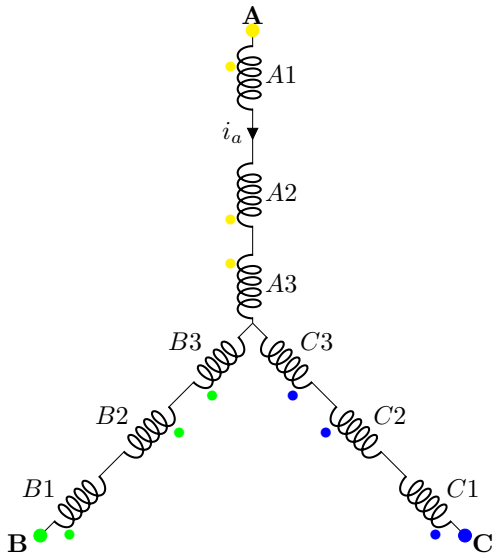

Figure (2.3) Wye coil configuration of the S-RSG.

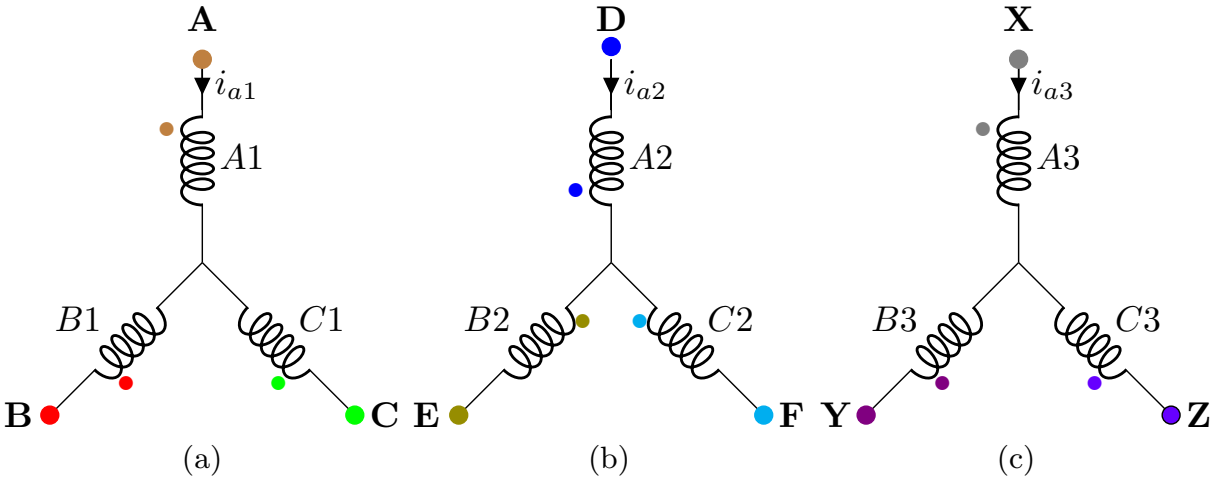

Figure (2.4) Wye coil configuration of the T-RSG.

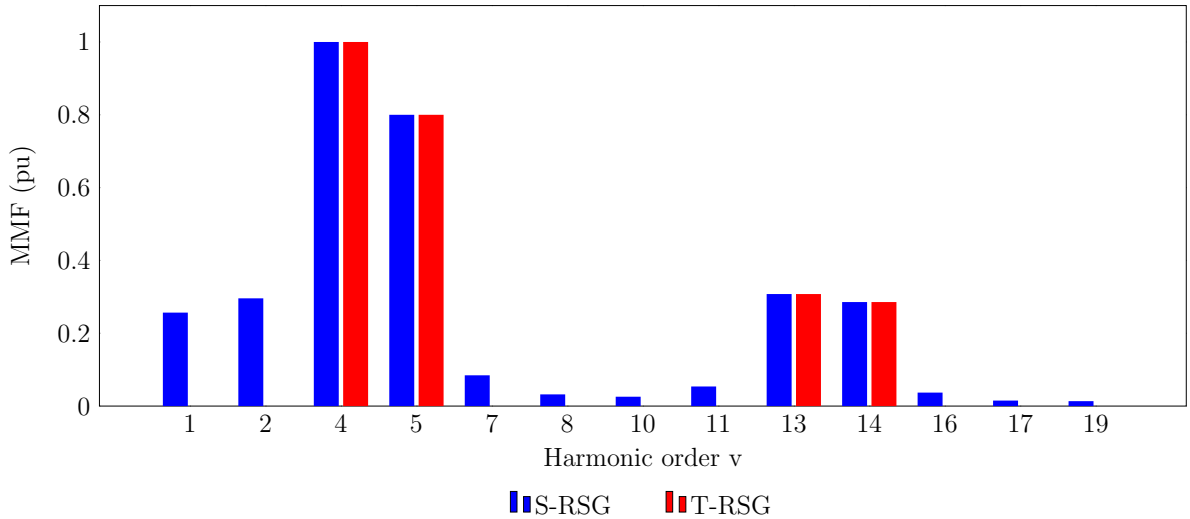

Figure (2.5) MMF harmonics versus harmonic order of the proposed reluctance generators

2.3. High Pole Number Epoxy-Casted Rotor Reluctance Synchronous Wind Generator (E-RSG)

2.3.1. Modular Epoxy-casted Reluctance Rotor

To ensure that the iron magnetic flux guides of the reluctance rotor are magnetically isolated from each other and from the mounting base, they can be separated and molded together by means of an epoxy resin. This would allow a modular epoxy-casted rotor pole section, such as shown in Fig. 2.6.

The casting of the inner epoxy can be done in the lamination stack, ensuring a good bond between the two materials as well as allowing for sectional pieces in terms of length and skewing. The external epoxy should be done with a mold on the outside that allows for surface modifiers, such as woven fiberglass cloth, to be used in conjunction to avoid surface cracking. To ensure stable operation at higher temperatures, the epoxy should be vacuum air extracted when casting and then heat treated. Additional mechanical linking between the epoxy and iron can be obtained by the addition of small dovetail cutouts in the lamination.

Each modular casted pole piece is then slid onto a spoked iron hub, as shown in Fig. 2.6. By mounting all the pole pieces on the hub, a complete reluctance pole hub is obtained, as shown in Fig. 2.7. To further increase saliency, the thin iron ribs at the top of the flux barriers may be machined away.

Casting of a reluctance rotor is not new [36]. What is different in this case is the manufacturing of the modular reluctance pole pieces. This reduces the manufacturing complexity and cost, and the pole pieces can be done in sections, allowing them to be stacked and skewed axially in length. It further allows the pole pieces to be manageable in terms of weight for a 5-MW machine, with a 378 mm long section (taking five sections along the axial stack length of the rotor) with a radial thickness of 152 mm and an average pole pitch of 297 mm weighing only around 80 kg.

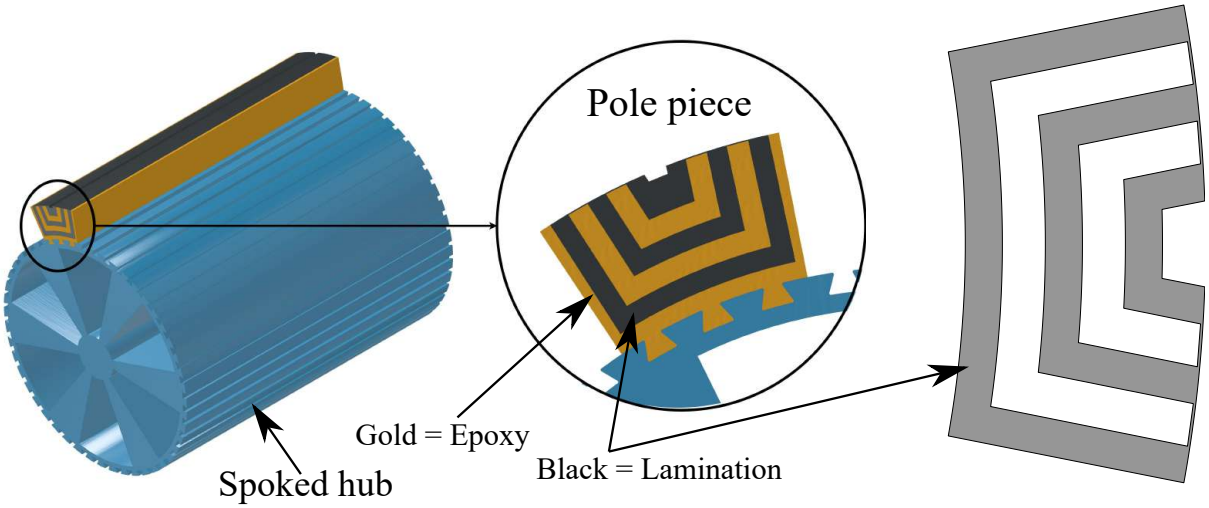

Figure (2.6) Epoxy-casted reluctance pole piece mounted on a spoked hub (left) ,pole piece (middle) (gold color is epoxy and black color is iron lamination) and lamination (right).

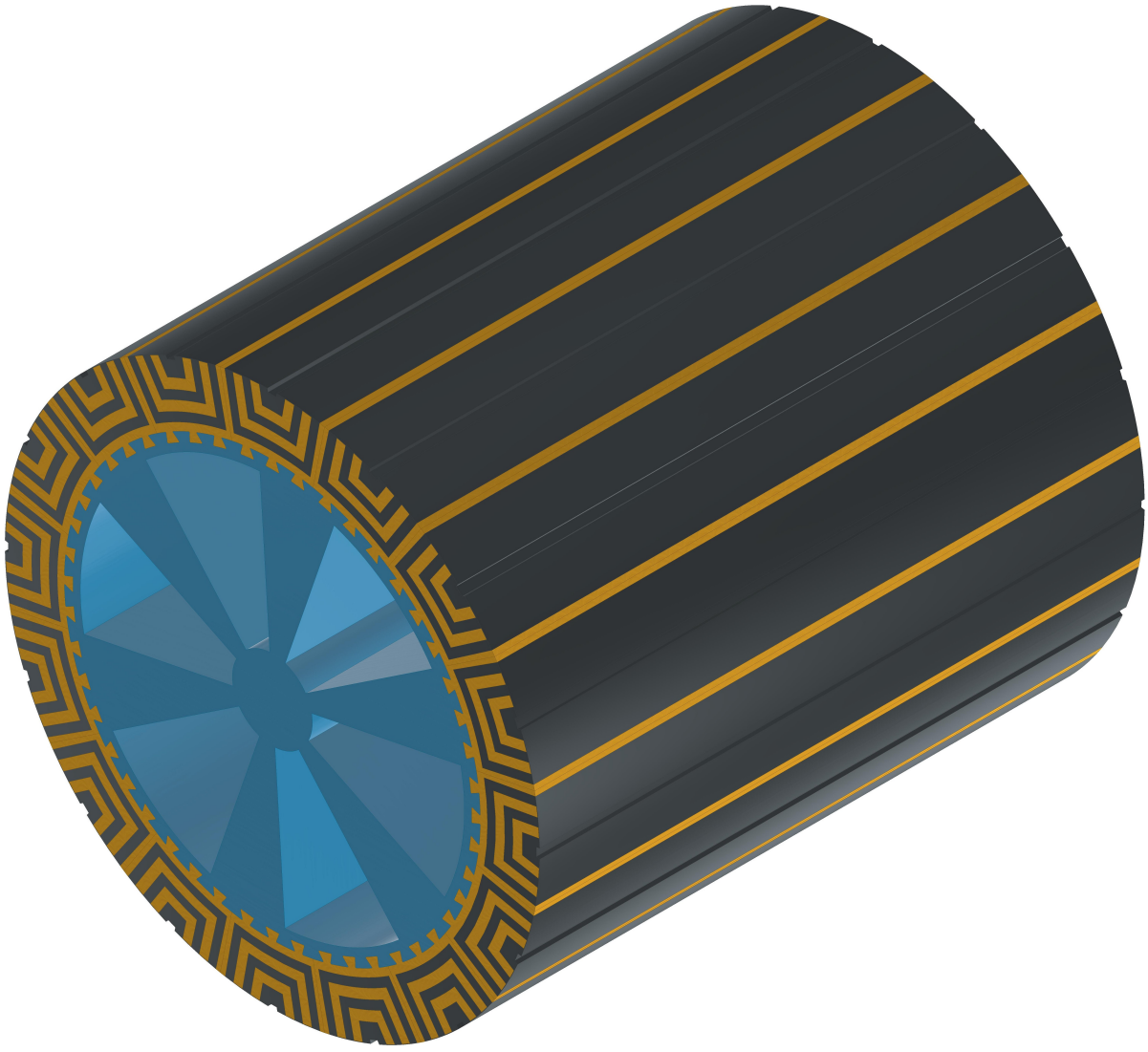

Figure (2.7) Assembled unskewed, epoxy-casted reluctance pole hub.

Chapter 3

Mathematical Modelling of the RSGs

The research question that is proposed in this thesis is addressed using a combination of theoretical analyses, simulations-run utilizing finite element methods, performance validation carried out with the aid of ANSYS Maxwell, and design optimization. In this chapter, the mathematical modelling procedures that are used in the implementation of these designs of the RSGs are laid out in detail.

3.1. Single three-phase RSG (S-RSG and E-RSG)

The performance of the machine was calculated by using classical *dq*-equations in steady state and in generator mode. A static time-stepped finite element (FE) analysis was used to calculate the flux linkages, inductances and torque, while the phase resistance and copper losses were calculated analytically. By deducing a balanced system, we could discard the 0-component from the dq0 transformation as shown by Fig. 3.1(a); here alpha is the transformation angle.

Calculations were performed as if the proposed machines are in generator mode with positive current out. As shown in Fig. 3.2, in order for the proposed machines to be operated as a generator with positive current flowing out, they have to be provided with a negative *d-axis* current, as shown in Fig. 3.3.

In addition, the ϕ_x and θ angles in Fig. 3.3 represent the ideal power factor and the current angles respectively. It is known that RSGs do not have a rotor field component, therefore the equations for the d- and q-axis supply voltages are represented in generator mode as

$$\begin{bmatrix} V_d \\ V_q \end{bmatrix} = \omega_e \begin{bmatrix} -\lambda_q \\ \lambda_d \end{bmatrix} + \omega_e L_e \begin{bmatrix} -I_q \\ I_d \end{bmatrix} + R_s \begin{bmatrix} I_d \\ I_q \end{bmatrix}, \tag{3.1}$$

where R_s is the stator winding resistance, including the main and end windings. The electrical angular velocity is represented by ω_e, with I_d and I_q being the *dq-axis* currents and L_e the end-winding leakage inductance. The end-winding leakage inductance is obtained using the techniques of [37].

In addition, both the main and leakage flux of the RSG are included in the λ_d and λ_q values of the *d*- and *q-axis* flux linkages.

The L_d and L_q self-inductances are defined by

$$L_d = \frac{\lambda_d}{I_d} \text{ and } L_q = \frac{\lambda_q}{I_q}, \tag{3.2}$$

Similarly, the electromechanical average torque is expressed by

$$T_{em} = \frac{3p_r}{4} I_d I_q (L_d - L_q), \tag{3.3}$$

where p_r represents the rotor pole pairs. The torque in (3.3) depends on the inductance difference $(L_d - L_q)$.

The generator ideal power factor is given by the following:

$$P_f = cos(\phi_x), \tag{3.4}$$

where ϕ_x is given by

$$\phi_x = tan^{-1}[\frac{(\frac{L_d}{L_q} + \frac{I_q}{I_d})}{\frac{L_d}{L_q} - 1}]. \tag{3.5}$$

The ideal power factor of the RSG according to (3.4) and (3.5) thus depends on the saliency ratio, $\frac{L_d}{L_q}$. Moreover, the real power factor angle between phasors **V** and **I** in Fig. 3.3, which is used in this thesis, includes the effect of the phase resistance. Given the current densities or phase currents, the *dq* parameters are then deduced using the Park transformation.

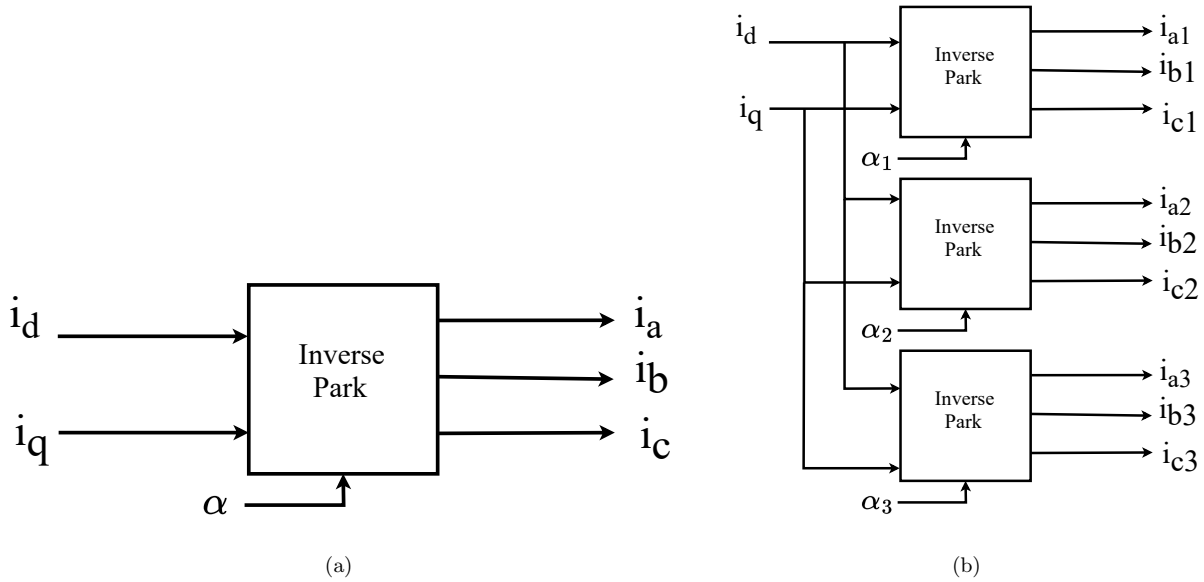

Figure (3.1) (a) S-RSG and (b) T-RSG inverse park transformation

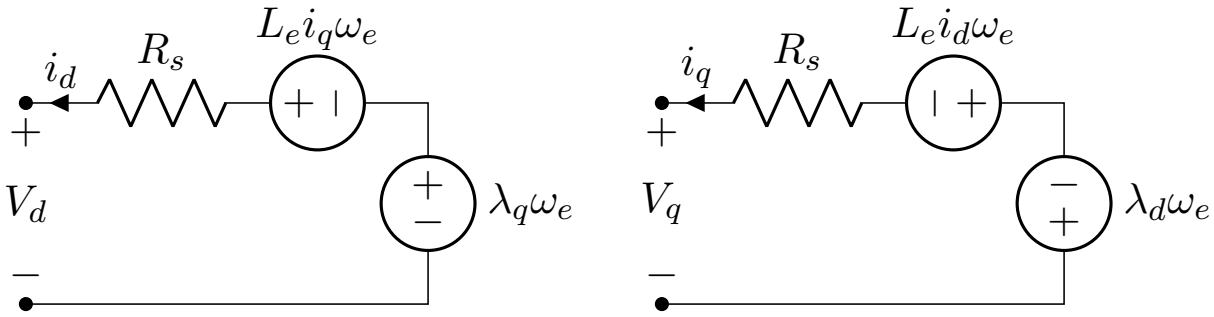

Figure (3.2) Proposed RSG equivalent DQ circuits.

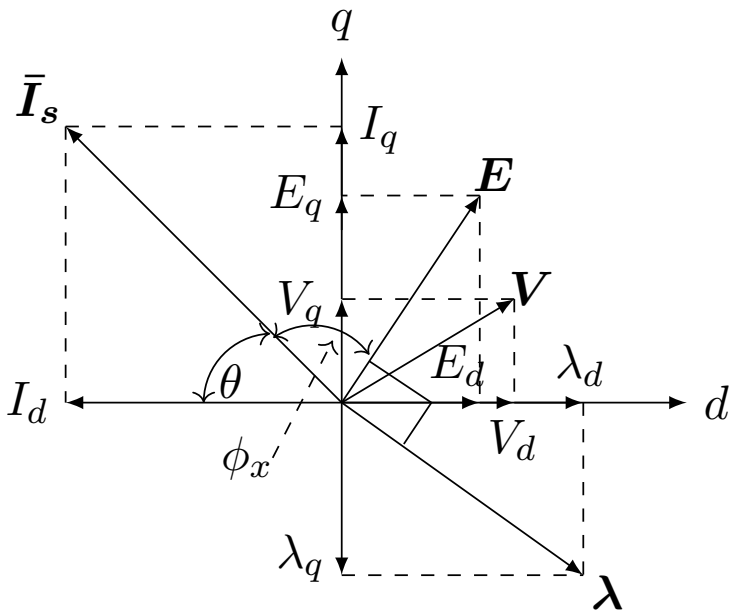

Figure (3.3) Proposed RSG phasor diagram.

3.2. Triple three-phase RSG (T-RSG)

For the triple three-phase RSG, FE analysis was further used to obtain the respective dq flux linkages. The *d-axis* flux linkages, for example, are calculated by

$$\lambda_{d1} = \ell_{d1} i_{d1} + m_{d2} i_{d2} + m_{d3} i_{d3}, \tag{3.6}$$

where ℓ and m are the inductance and mutual inductances of each winding respectively. In (3.6), each winding is supplied with an equal magnitude of dq currents of $i_{d1} = i_{d2} = i_{d3} = I_d$, as shown in Fig. 3.1 (b), thus

$$\lambda_{d1} = (\ell_{d1} + m_{d2} + m_{d3}) I_d. \tag{3.7}$$

The total dq flux linkages and the respective inductances are given by

$$\lambda_{d1} = L_{d1} I_d \tag{3.8}$$

and

$$\lambda_{q1} = L_{q1} I_q \tag{3.9}$$

$$\begin{bmatrix} L_{d1} \\ L_{d2} \\ L_{d3} \end{bmatrix} = \begin{bmatrix} \lambda_{d1} \\ \lambda_{d2} \\ \lambda_{d3} \end{bmatrix} \frac{1}{I_d} \tag{3.10}$$

$$\begin{bmatrix} L_{q1} \\ L_{q2} \\ L_{q3} \end{bmatrix} = \begin{bmatrix} \lambda_{q1} \\ \lambda_{q2} \\ \lambda_{q3} \end{bmatrix} \frac{1}{I_q}. \tag{3.11}$$

As it can be seen in Fig. 3.4, with equal dq currents as shown in Fig. 3.1(b), the average dq flux linkages $\lambda_{d1} = \lambda_{d2} = \lambda_{d3}$ and $\lambda_{q1} = \lambda_{q2} = \lambda_{q3}$. Hence, the respective dq inductances can be expressed as $L_{d1} = L_{d2} = L_{d3}$ and $L_{q1} = L_{q2} = L_{q3}$.

Similarly, in the presence of more than one three-phase winding set as shown in Fig. 2.4, the electromechanical average torque for the multi three-phase generator is

$$T_{em} = \frac{3p_r}{4} I_d I_q \sum_{k=1}^{n} (L_{dk} - L_{qk}), \tag{3.12}$$

where n represents the number of three-phase winding sets.

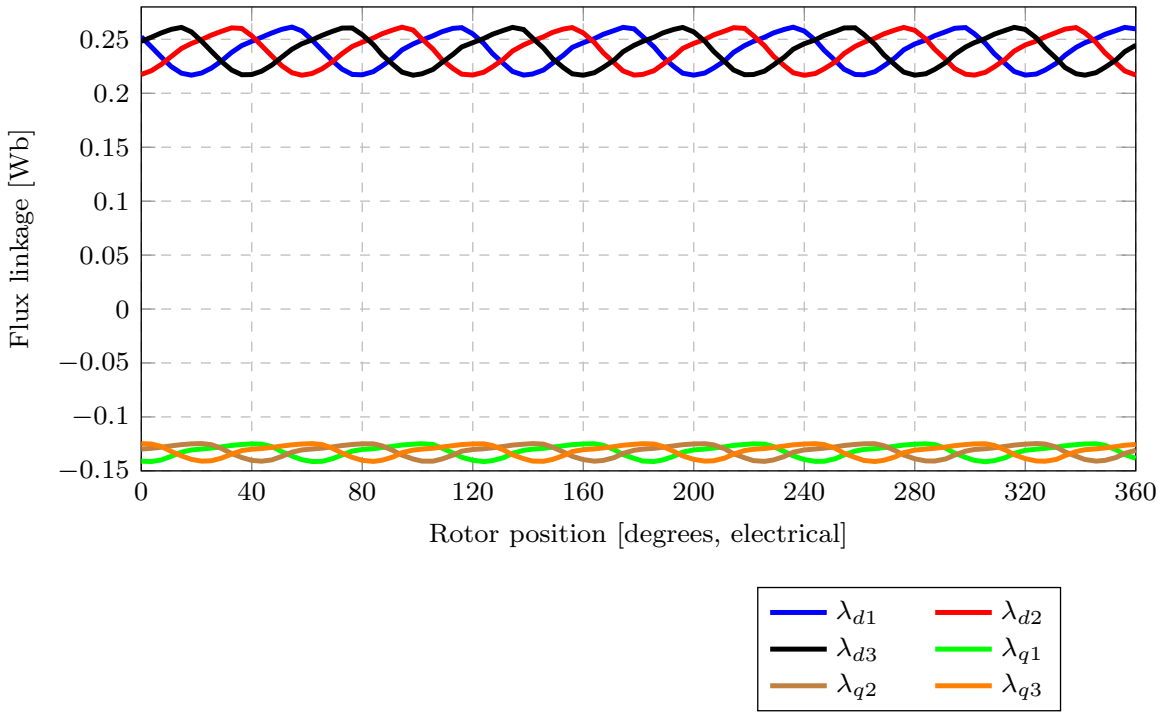

Figure (3.4) T-RSG dq flux linkages versus rotor position

3.3. Torque ripple

RSMs can exhibit high torque ripple. Therefore, to calculate torque ripple percentage, the following equation is used

$$T_\delta = \frac{T_{max} - T_{min}}{T_{em}} \times 100\%, \tag{3.13}$$

where T_{max}, T_{min} and T_{em} are the respective maximum, minimum, and rated average torque result of multiple FEM rotor-step simulations. Previous researchers have shown many techniques to reduce torque ripple. In this thesis, a few of these techniques are used including the use multi-phase, fractional-slot winding technology and rotor skewing.

3.4. Core losses

This section gives the techniques used to obtain the core losses calculated both analytically and by the preferred package, SEMFEM.

3.4.1. Analytical core losses

Based on Steinmetz's core loss equation, an altered version of the equation is used to calculate the core losses, as follows:

$$P_c = \underbrace{c f_0^x [B_{t_0}^y M_{r_0} + B_{y_0}^y M_{y_0}]}_{\text{Rotor}} + \underbrace{c f_1^x [B_{t_1}^y M_{t_1} B_{y_1}^y M_{y_1}]}_{\text{Stator}}. \tag{3.14}$$

In (3.14), B_t and B_y represent the maximum flux density in the teeth and yoke for the corresponding RSG stator and rotor respectively. Similarly, M_t and M_y represent the mass in the teeth and yoke respectively. In (3.14), c, x and y are the Steinmetz coefficients. Readings and loss-frequency curves of laminated steel at the fundamental supply frequency f_1 can be used to find these coefficients.

Furthermore, as a case study, this thesis investigates the core losses for S-RSG and T-RSG in the stator. To achieve this, the actual air-gap flux densities were investigated for both proposed machines, as shown in Fig. 3.5. Using the methods of [38] to relate the maximum flux densities from the air-gap flux density for both the yoke and teeth of the stator, and together with (3.14), a quick estimation of the stator core loss is made and presented later in the thesis.

3.4.2. FE Core losses

Static time-stepped simulations can function without temporal data in most cases. Nevertheless, temporal information is required for the computations involving core loss in the preferred FE package, *SEMFEM*. A time domain formulation of the Steinmetz equation

for core loss is used by *SEMFEM* in the course of the time-stepped simulations that are carried out over a full mechanical period. The core loss as a function of the number of steps is shown in Fig. 3.6. 80 to 100 steps have been decided upon as the optimal amount for which to carry out the *SEMFEM* simulation as part of the thesis in order to achieve an accurate value for the core losses. As can be seen in 3.6, this point (from 80 steps) marks the point at which the core losses begin to stabilize.

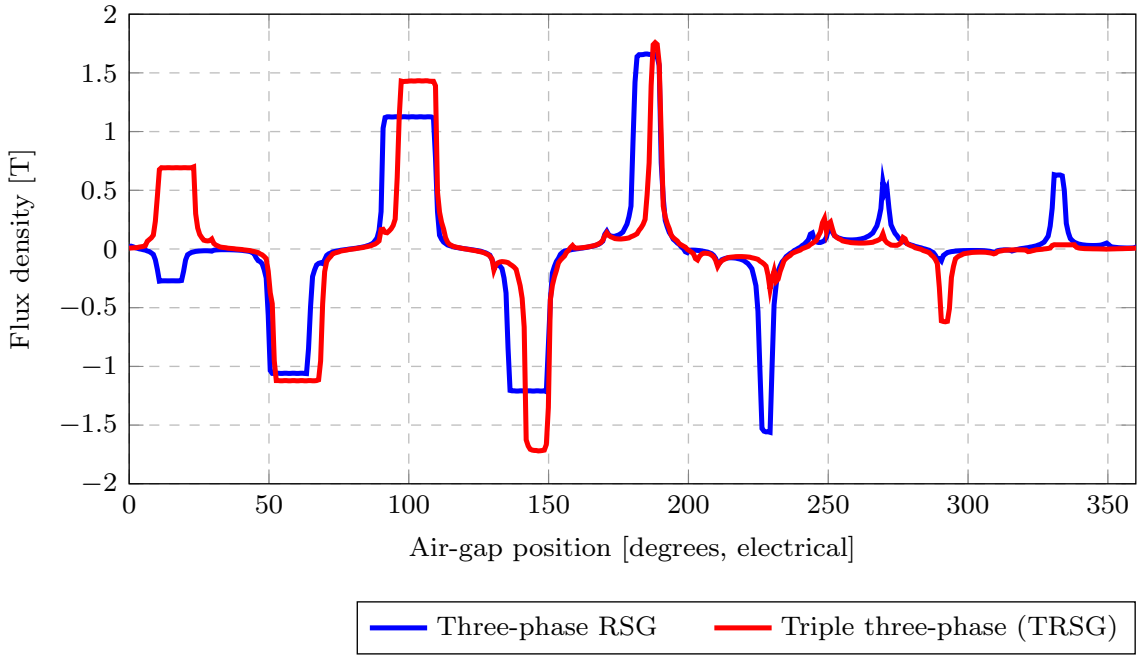

Figure (3.5) FE-calculated full load air-gap flux densities of the S-RSG and T-RSG versus air-gap position.

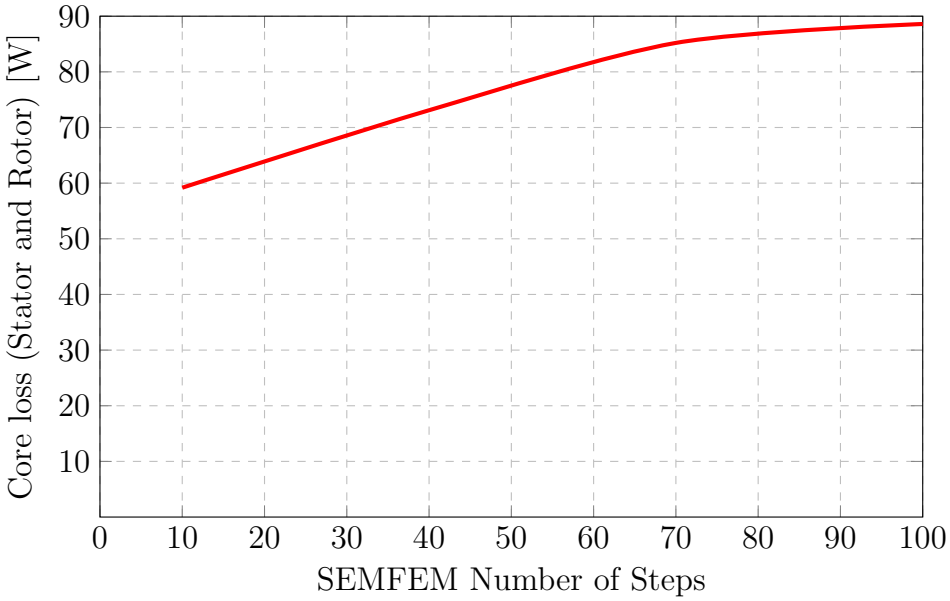

Figure (3.6) Core losses versus *SEMFEM* number of steps.

3.5. Copper losses

The copper losses are given by

$$P_{cu} = \left[\sum_{k=1}^{n} 3I_s R_s\right], \tag{3.15}$$

where R_s is the stator's winding phase resistance as calculated by

$$R_s = \frac{2W\rho_t(l + l_{end})}{f_f(n_a \frac{A_{cu}}{z})}, \tag{3.16}$$

where W = number of series turns per phase, ρ_t = resistivity of copper, l = stack length of the generator, l_{end} = average length of a winding end, f_f = fill-factor, n_a = number of parallel winding circuits, A_{cu} = active copper area per stator slot and z = number of conductors per stator slot.

3.6. End-winding leakage inductance

To calculate the end-winding leakage inductance, we take a look at two different methods of calculations. The first method is used for non-overlap winding and the second being for overlap winding.

3.6.1. Non-overlap winding : End-winding leakage inductance

In 2D-FEA, the inductance of the end windings is not taken into account because it is a 3D component. Therefore, in SEMFEM the end winding inductance calculations must be manually and analytically calculated. Hence, for non-overlapping winding, this thesis consults the methods of [37] to calculate the end-winding inductance which is given by,

$$L_{end(1)}(a = \frac{l_e}{2}, c = w_c, b = h_c) = \frac{1.974}{n_a^2}\left(\frac{2a^2}{b}\right) N_p^2 q_c K, \tag{3.17}$$

$$L_{end(2)}(a = \frac{l_{end}}{2}, c = w_c, b = h_c) = \frac{1.257}{n_a^2} l_{end}\left(\frac{2a}{b}\right) N_p^2 q_c K, \tag{3.18}$$

$$L_e = K_M(L_{end(1)} + L_{end(2)}), \tag{3.19}$$

$$l_{end} = w_c + w_t, \tag{3.20}$$

where w_t is the tooth width, w_c the coil width and h_c the coil height. Additionally, n_a represents the number of parallel circuits. Based on [36], K is defined as a constant with variables a, b, and c, and K_M as a factor for the effect of high mutual phase coupling.

3.6.2. Overlap winding : End-winding leakage inductance

The end-winding leakage inductance used for the overlapping winding with rectangular shaped winding ends is obtained using the methods of [38] and is given by the following:

$$L_e = mS_i \frac{V_3}{2\pi} \left[\frac{WK_dK_{p(3)}}{p_r} \right] k_{e(p_r)*10^{-8}Henry/phase}, \tag{3.21}$$

where V_3, the shape factor for rectangular shaped coils = 1040, $k_{e(p_r)}$ = end-winding factor for a p_r pole-pair machine. Furthermore, m represents the number of phases, S_i = stator inner diameter. Additionally, K_d is winding distribution factor given by,

$$K_d = \frac{sin(\frac{\pi}{6})}{Q_s sin(\frac{\pi}{6Q_s})}, \tag{3.22}$$

where Q_s is the number of stator slots. The end-winding coil pitch factor, $K_{p(3)}$, is obtained with the following equation:

$$K_{p(3)} = \frac{sin(c\pi)}{6Q_s}, \tag{3.23}$$

where c represents the coil pitch in terms of Q_s.

3.7. Electric Loading Parameters

The electric loading, A, and RMS slot current density, J, are important machine parameters for the large RSGs. Also, the AJ value, which is the product of A and J, is an important thermal indicator. The current density was defined and kept constant in the design optimization of the RSGs. The AJ value of the RSG is determined by

$$AJ = \frac{J^2 A_s k_f Q_s}{\pi D_i}. \tag{3.24}$$

In (3.24), A_s is the slot area available for the copper conductors, k_f is the copper fill factor, Q_s the number of stator slots and D_i the stator inner diameter.

3.8. Power and Efficiency

In this section, the computations for the power generated by the RSGs are stated in terms the working principles of a wind turbine, with the input power originating from the rotating of the turbine blades coupled to the rotating shaft through a gearbox. Fig. 3.7 shows the basic power flow diagram for this study. The mechanical input power is given by,

$$P_{in} = P_{conv} + P_c, \tag{3.25}$$

where P_{conv} is the conversion power described by the following:

$$P_{conv} = T_{em}\omega_m. \tag{3.26}$$

The power that is translated from mechanical to electrical form is reduced due to losses incurred by the copper (P_{cu}) and the core (P_c). The contribution of these losses can be summed up by the following:

$$P_l = P_{cu} + P_c, \tag{3.27}$$

We exclude friction, windage, and stray losses since doing so simplifies the calculations and because their relative importance is usually modest. In addition, the inverter switching losses in the RSGs and the medium-speed gearbox losses in the drive-train are disregarded. The output power is given by,

$$P_o = \frac{3}{2}(V_d I_d + V_q I_q). \tag{3.28}$$

The efficiency is given by,

$$\eta = \frac{P_o}{P_{in}} * 100\%. \tag{3.29}$$

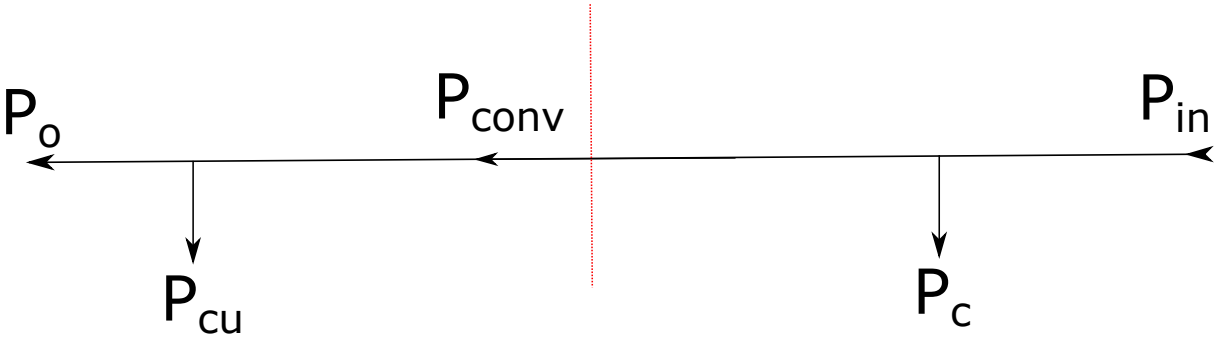

Figure (3.7) Power flow diagram of the proposed RSGs.

Chapter 4

FEM Packages

Chapter 3 describes the equations that characterize the RSGs studied in this thesis. These equations are used to obtain the performance of the RSGs. Furthermore, prior to estimating the Performances, a *FEM* simulation and calculations are done in order to establish the important parameters that are needed to compute the machine performances. Therefore, using an in-house, python-based program, called *SEMFEM*, this chapter describes how the *FEM* simulations and computations are handled. Further, we make use of a commercial *FEM* package, called *Ansys Maxwell* to verify the results obtained in *SEMFEM*.

4.1. SEMFEM

SEMFEM version 3.8.1 was used for modeling the electric machines of the proposed RSGs in this thesis. The *FEM* package is an in-house product that includes a number of libraries and programs that allows for the simulation of electrical machines. In comparison to commercial *FEM* packages such as *Ansys Maxwell* and *MagNet*, *SEMFEM* has gained its popularity among Stellenbosch University's electrical machine lab (*EMlAB*), since it is quick and versatile while maintaining high accuracy. Furthermore, SEMFEM is reported to offer features that *MagNet* does not, although it is limited to only static 2D finite element simulations [34]. By developing multi-stage static simulation approaches, [34] expands the functionality of our finite element simulation to achieve certain outcomes that would require temporary solvers otherwise.

Originally known as *Cambridge package*, *SEMFEM* is an improved version of it. Simulations are performed in time-stepped, 2D mode in this program. As *SEMFEM* has evolved from its original development by Dr. Gerber in 2011 to its modified version in the subsequent years, it is now able to model linear machines with tubular, axisymmetric topologies, as well as machines with multiple air-gaps. Additionally, parallelization was also introduced for both the *FEM* simulation and the optimization program, in order to improve the speed of the numerical optimization process [39].

To make use of *SEMFEM*, users employs *SEMFEM* by implementing a Python modeling script. For performance considerations, the bulk of *SEMFEM* functionality is implemented in Fortran and C libraries. The user manual with all important fundamentals is given by

the documentation provided by [34].

The phases involved in the modelling of an electric machine in FEM include pre-processing, processing, and post-processing. Pre-processing describes the stage of the FEM modelling process in which the machine is separated into many areas, including the rotor, air-gap, and stator. It comprises three key tasks: material specification for components/regions, cross-sectional area or volume mesh production; and problem description. It may also entail illustrating the machine's components for aesthetic reasons in certain cases. The appropriate configuration of each component's material parameters is a critical step, particularly for materials with non-linear qualities that execute the BH-curve fit. The suitable material for the suggested RSG designs is *M400-50A*, which is easily available in the material libraries of the preferred FEM packages. Furthermore, if necessary, the FEM packages allowed the user to create a new material or modify an existing material into customized specifications.

Alternatively, in order to improve the accuracy of the FEM solution, the mesh size of the FE must be modified appropriately. This is due to the fact that mesh size not only affects the correctness of the solution, but also determines the computational time. In other words, a finer mesh yields more precise solutions but requires more time to solve. So, to find a middle ground between these two different needs, a finer mesh was used in air gaps and other RSG sections with a large predicted flux gradient, while a coarser mesh was used in sections with less flux variation.

4.1.1. Flux linkage calculation

In *SEMFEM*, the 2D FE package used the total flux linkage calculation assumes that the field remains constant along the z-axis. As a result, the magnetic vector potential of the 2D FE solution is solely z-directed, and is given by

$$\mathbf{A} = A_z \mathbf{z}, \tag{4.1}$$

where $\boldsymbol{A}$ is the magnetic vector potential and $\boldsymbol{z}$ represents the z-directional unit vector. Additionally, with $\boldsymbol{B} = \nabla \times \boldsymbol{A}$ and Stoke's theorem, it is possible to obtain the cumulative magnetic flux linkage of a winding through a given surface S, which can be expressed by means of integration as:

$$\varphi = \int_s \mathbf{B}.d_s. \tag{4.2}$$

The flux linkage for a N-turn coil with each turn coupling a flux and omitting the end-winding area is the sum of the flux for the complete number of coil turns given by

$$\lambda = N_t \int_s \mathbf{B}.d_s, \tag{4.3}$$

where N_t is the number of coil turns.

4.2. Ansys Maxwell FEM

Ansys Maxwell is deemed more convenient than *SEMFEM*. It follows the trend of conventional CAD software by providing the user with a graphical, point-and-click environment instead of a python, script-based interaction. Maxwell provides a wider range of functionalities, particularly when combined with other Ansys family technologies. In this thesis, we make use of *Ansys Maxwell* to confirm the simulated results obtained in *SEMFEM*. For this, we compare the average Torque, torque ripple as well as core losses as shown in the later sections.

4.3. Skewing

As previously mentioned, one of the main issues associated with modeling reluctance machines is torque ripple. A well known method to reduce torque is implemented in this thesis.

In order to skew the rotor, the RSG is broken up into five different submachines in *SEMFEM* so that it may be used to represent a skewed machine. Since a *SEMFEM* simulation is a time-stepped simulation, a single simulation includes several steps even if it is run repeatedly. At each stage of the simulation, from step 1 all the way up to

step k, the performance of the five submachines is assessed. Each phase illustrates the simulated machine after a certain length of time has elapsed. As the machine continues to spin over the course of time, this eventually coincides with a certain rotational position. In the process of skewing, the mean performance of the five submachines is linked to one *SEMFEM* simulation step as opposed to replicating a single machine position at a single simulation phase. The latter is shown in Fig. 4.1. Fig. 4.2 shows the unskewed machine representation with a full submachine. A mechanical angle, α, as shown in Fig. 4.1, corresponding to the skew angle yields the positional rotation of the five submachines, α_{1-5}, as explained by [6] and is given by the following:

$$[\alpha_1 \quad \alpha_2 \quad \alpha_3 \quad \alpha_4 \quad \alpha_5] = \frac{1}{5}[-2\alpha \quad -\alpha \quad 0 \quad \alpha \quad 2\alpha] \tag{4.4}$$

Modification of each current angle of the submachines (α_{1-5}) is further modified by means of adding the respective skew angle, which is first translated to electrical degrees (α_{el}), to the optimal Current angle (θ_{opt}), given by

$$[(\theta_{opt} + \alpha_{el_1}) \quad (\theta_{opt} + \alpha_{el_2}) \quad (\theta_{opt} + \alpha_{el_3}) \quad (\theta_{opt} + \alpha_{el_4}) \quad (\theta_{opt} + \alpha_{el_5})]. \tag{4.5}$$

In order to achieve accurate simulation results, the skewed simulation is run several times at a sufficient number of distinct rotational locations. According to the authors in [40], the results obtained in simulating five submachines yields an accurate enough results. Hence, when increasing the number of sub-machines in a simulation by more than five, there is no discernible change in the outcomes of the simulation results. What is important however, is the desired skew angle which makes a significant impact on the performance results.

This chapter takes a look at the FEM packages used in this thesis to accurately simulate the proposed RSGs. Furthermore, an important technique used to reduce the torque ripple in the epoxy-casted RSGs (E-RSG) is explained. Chapter 7 will further give more details on the skewed machines and the impact that skewing had on the E-RSGs.

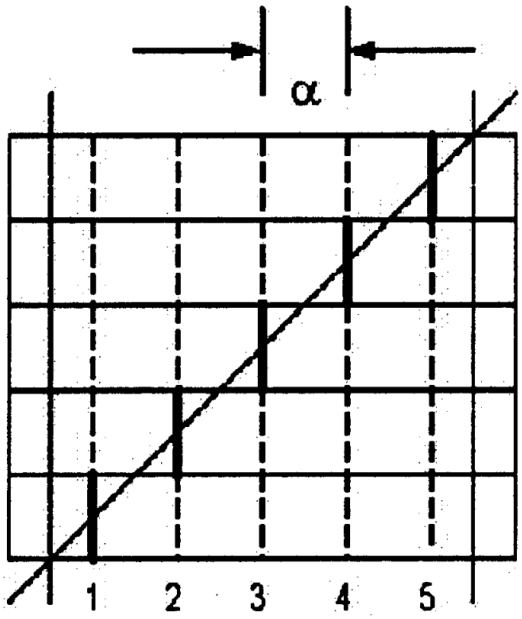

Figure (4.1) Schematic depiction of a skewed machine consisting of five submachines. [40]

.

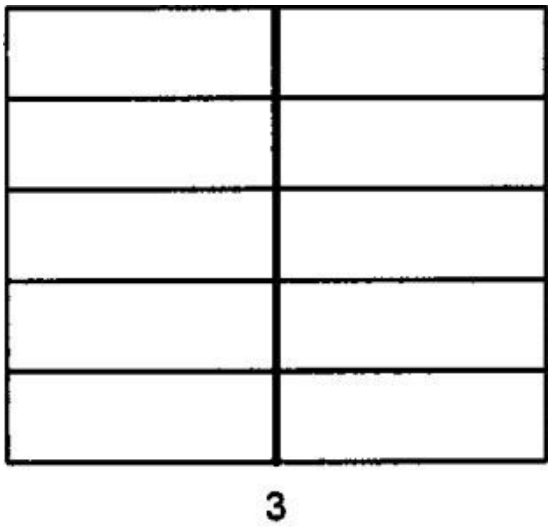

Figure (4.2) Schematic depiction of an unskewed machine consisting of a full submachine. [40]

.

Chapter 5

Simulations (S-RSG and T-RSG)

In the previous chapter, an overview of the preferred FEA packages is explained. With the focus being on *SEMFEM*, this chapter gives the simulation and performance results obtained for S-RSG and T-RSG. Furthermore, a comparison between the S-RSG and the T-RSG is given, and finally a conclusion is drawn. Fig. 5.1 shows the focus for this chapter.

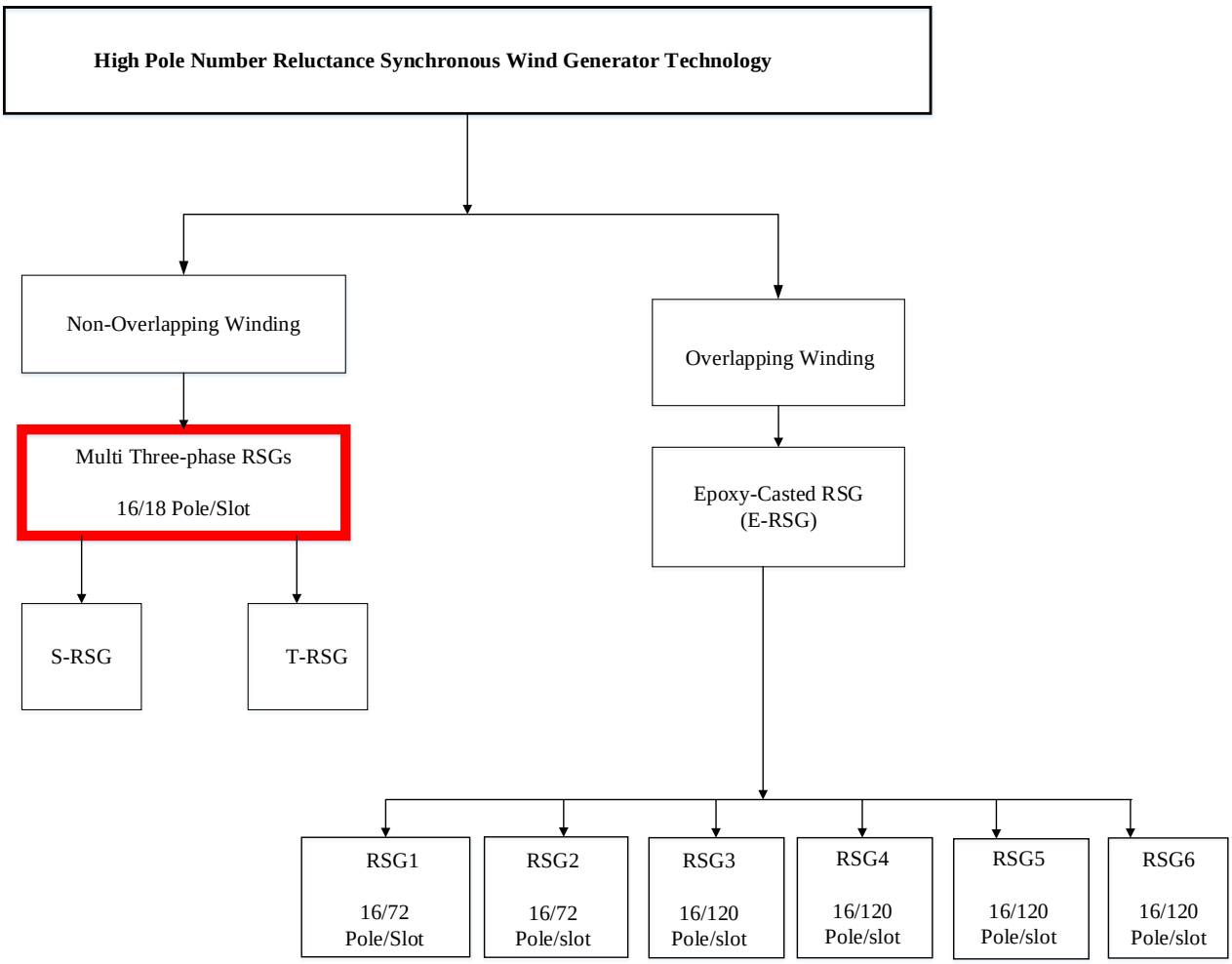

Figure (5.1) High pole number RSG design layout showing the chapter focus.

5.1. FEA Performance Comparison using Ansys Maxwell

With the same 50 Hz abc currents as inputs, the average torque, torque ripple and core losses of the single three-phase winding RSG are determined by time-step FEA using the *SEMFEM* and *Ansys Maxwell* software packages. The results of these calculations are shown in Table 5.1. This shows good comparison in the results of the two packages and, hence, confirms the performance prediction using the preferred *SEMFEM* FEA package.

Table (5.1) FEA PERFORMANCE COMPARISON OF THE S-RSG.

Performance parameter	*SEMFEM* FEA	*ANSYS Maxwell* FEA
Average Torque	35.6 Nm	34.7Nm
Torque Ripple	24.52 %	22.70%
Total core loss	88.62 W	74.76 W
Rated speed	375 rpm	375 rpm
Rated frequency	50Hz	50Hz
Lamination Material	M470-50A	M470-50A
Winding layout	Double-layer	Double-layer

5.2. Torque ripple

Fig. 5.2 shows the waveforms of the simulated torque versus rotor position comparison against two FEM packages, static FE (*SEMFEM*) and transient FE (*ANSYS Maxwell*).

From the FE packages the torque averages and torque ripple percentages calculated by both methods are close enough for comparison purposes. The results of the unskewed RSGs presented indicates that these two packages exhibits a similar behaviour for the proposed generators.

Furthermore, a dramatic torque ripple percentage reduction from the conventional three-phase RSG (S-RSG) with a torque ripple of 24.5% to the T-RSG with a torque ripple of 7.7% is seen in Fig. 5.2. This can further be explained by the reduction of the sub-MMF harmonics.

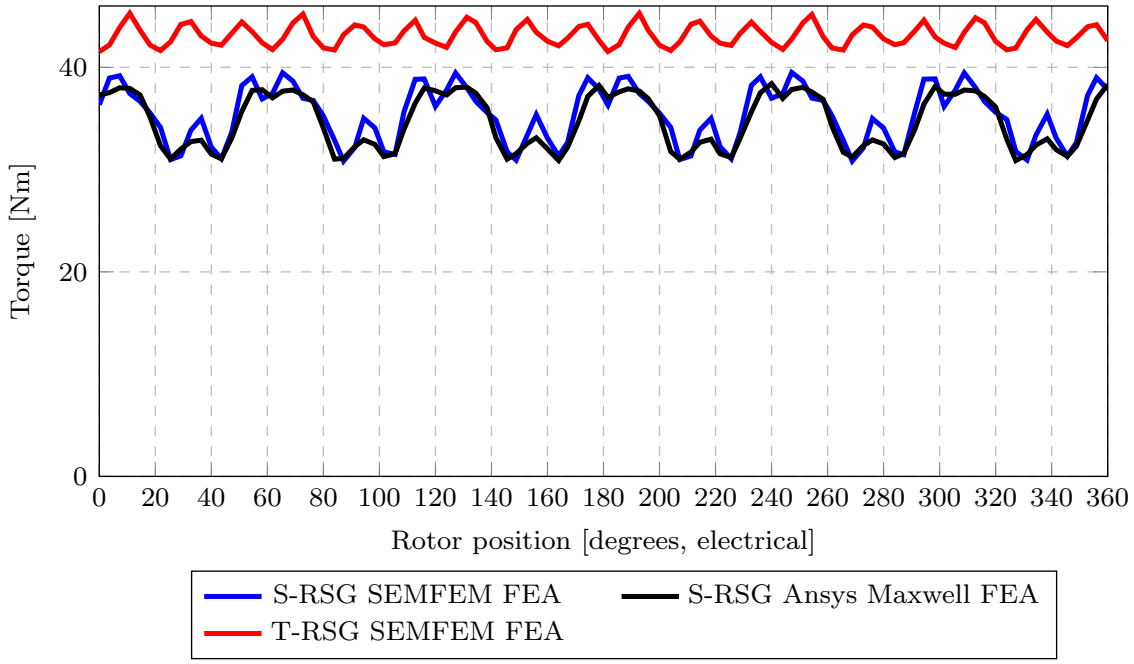

Figure (5.2) Torque versus rotor position comparison against two FEM Packages for the proposed RSGs.

5.2.1. Reduction of core losses

Fig. 5.3 shows the results obtained from the stator core loss study demonstrating a dramatic reduction in the core losses going from the conventional S-RSG to the T-RSG. This once again shows the effect of the reduced MMF harmonics in the T-RSG. Also, the analytically calculated core losses presented in Fig. 5.3 show good comparison with the FEA core-loss calculation as given in Table 5.2. The effect of this core loss reduction on the T-RSG's efficiency is elaborated in the following subsection (section 5.2.2), Table 5.2.

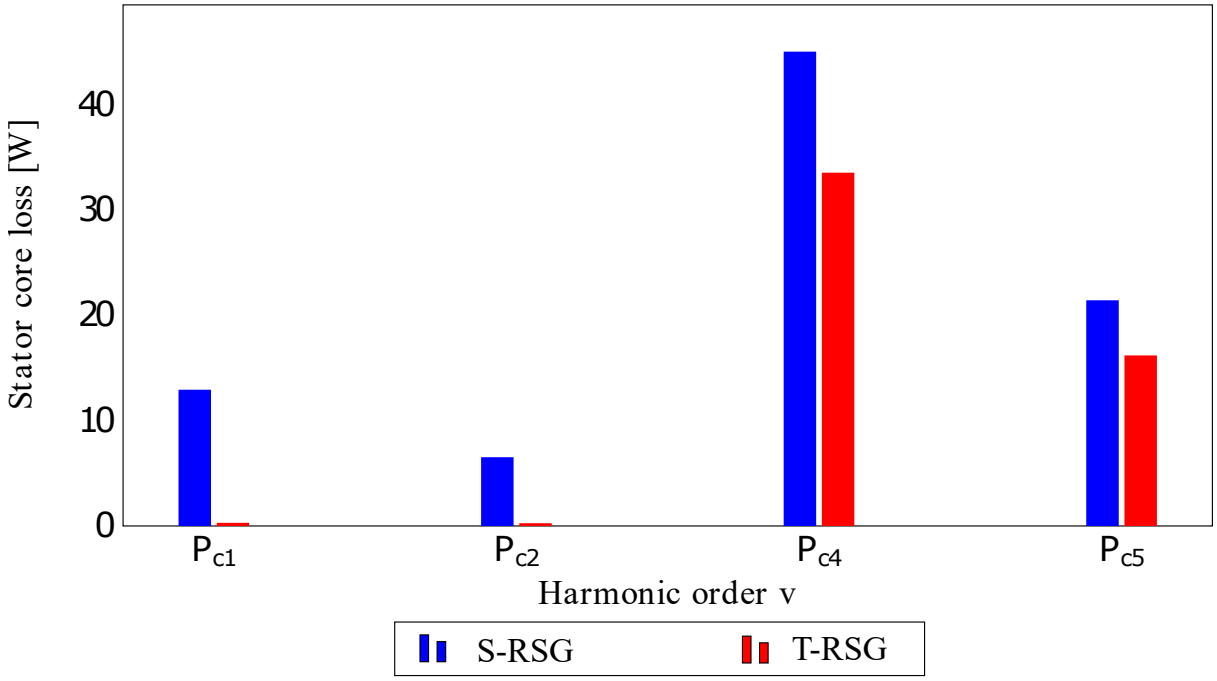

Figure (5.3) Analytically calculated core loss comparison of the S-RSG and T-RSG per harmonic order.

5.2.2. Comparing S-RSG and T-RSG performance

The simulated performance results in Figs. 5.4 and 5.5 shows that the T-RSG compared to S-RSG is the most efficient design option. These results show that an optimum current angle of 47° and 50° at full load is achieved for the S-RSG and T-RSG respectively. These optimal angles are shown to provide the best trade-offs for a good torque and power factor, as well as efficiency in both machines. Furthermore, as shown in Table 5.2, these optimal current angles also give the best overall machine performance for both machines.

Fig. 5.6 summarizes the overall better performance of the T-RSG as the S-RSG. In this per unit performance comparison the base values include a torque 35 Nm, torque ripple of 25%, unity power factor, 100% efficiency and torque density of 5.5 kNm/m^3

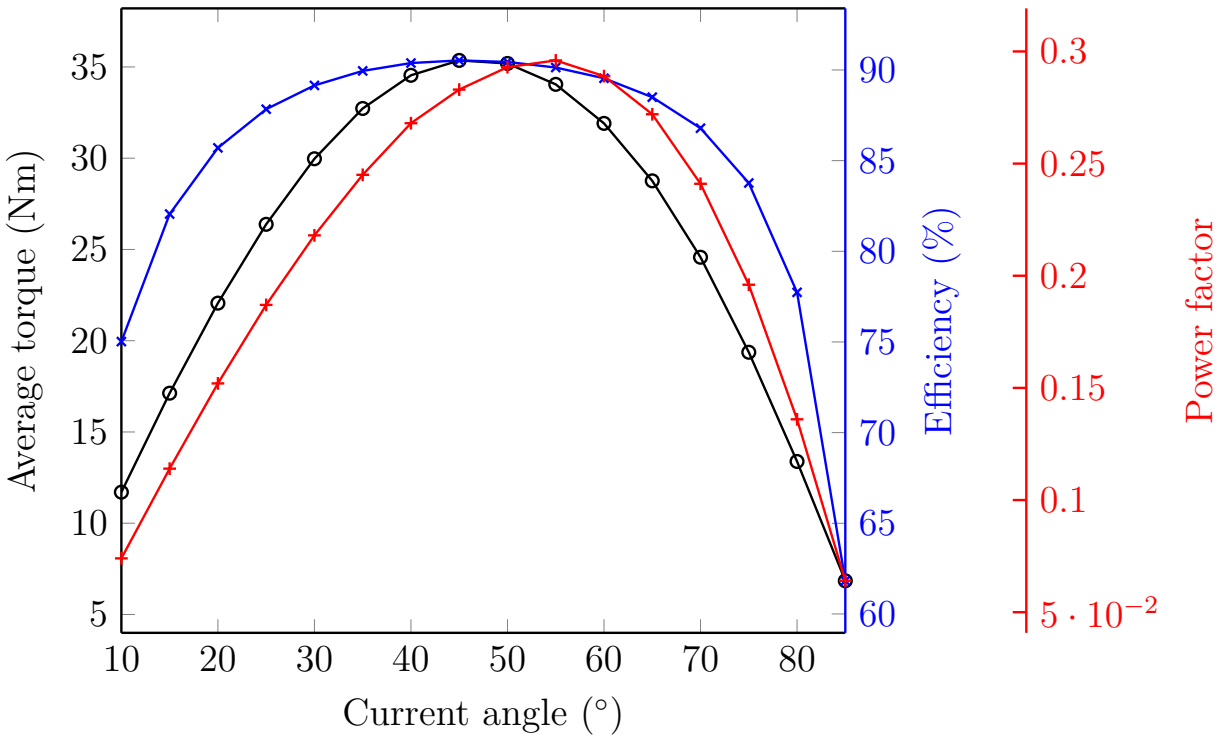

Figure (5.4) S-RSG performance versus current angle.

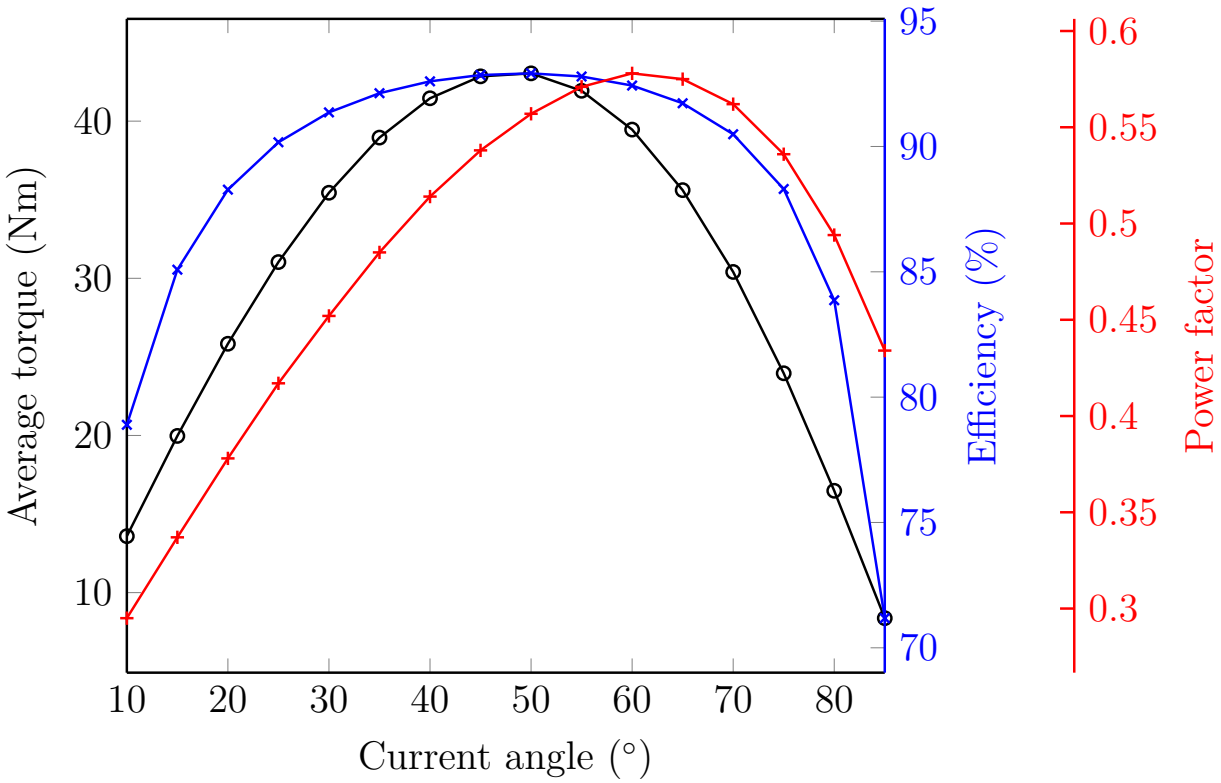

Figure (5.5) T-RSG performance versus current angle.

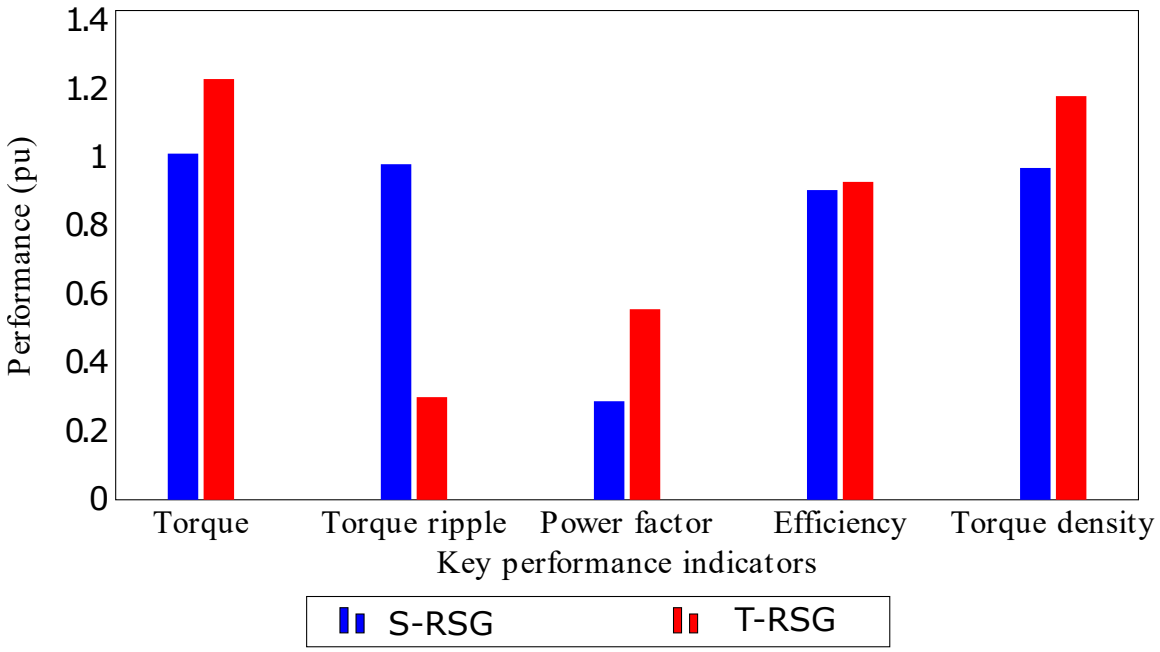

Figure (5.6) Per-unit performance comparison of the S-RSG and T-RSG. The base values include a torque 35 Nm, torque ripple of 25%, unity power factor, 100% efficiency and torque density of 5.5 kNm/m^3.

Table (5.2) S-RSG AND T-RSG PERFORMANCE COMPARISON.

Parameter	Performance		
	Description	S-RSG	T-RSG
P_o (kW)	Power out	1.34	1.64
T_{em} (Nm)	Average torque	35.12	43.04
T_d (kNm.m^{-3})	Torque density	5.33	6.49
η (%)	Efficiency	90.52	92.92
P_f (p.u)	Power factor	0.288	0.55
T_r (%)	Torque ripple	24.52	7.5
P_c (W)	Total SEMFEM core loss	88.98	70.92
P_c (W)	Total ANSYS Maxwell core loss	74.76	56.83
P_c (W)	Analytical core loss (stator only)	85.97	52.13
θ (°)	Current angle	47	50
J (A/mm^2)	Current density	6	6
L_d (mH)	d-axis inductance	222	93
L_q (mH)	q-axis inductance	176	43
L_d - L_q (mH)	Inductance difference	46	50
L_d / L_q	Saliency ratio	1.26	2.16

5.3. Summary

In this chapter, the design and simulations of a 16/18 pole/slot non-overlap winding, multi three-phase RSGs is presented. The results obtained for the proposed S-RSG in *ANSYS Maxwell* and *SEMFEM* indicate good correlation for comparison purposes. This step is important as it verifies that the proposed model has been designed and analyzed correctly. Additionally, a performance comparison is made between S-RSG and T-RSG. The results of T-RSG shows an overall performance improvement compared to S-RSG which is due to the removal of the sub- and higher MMF harmonics.

Chapter 6

DESIGN OPTIMIZATION METHODS

There are numerous ways to produce the best possible designs, and these methods can be used to design electric machines too. There are two distinct methods by which these techniques can be characterized, namely gradient based and non-gradient based. The direction of the search is determined by the gradient of the function at the present position when using gradient-based techniques. When searching for a better point in a space with multiple dimensions, the line search is one technique that can be utilized. The procedure can be expressed by

$$\text{Min or Max} \quad F[\mathbf{X}], \mathbf{X} \in R^n, \tag{6.1}$$

where $F[\mathbf{X}]$ is a reasonably smooth function and $\mathbf{X}$ is an n-vector-matrix comprising n parameters to be optimized. For functions with various parameters, this method is most commonly employed. According to [41, 42], the vast majority of gradient-based approaches struggle when confronted with noisy and discontinuous functions, since they were not developed to cope with discrete variables.

Additionally, according to [41, 42], in order find the minimum or maximum of an objective function in a multidimensional space, non-gradient approaches are utilized. They are used when solving nonlinear optimization problems with unknown derivatives. These techniques are renowned for always locating an optimal solution, whereas gradient methods can become trapped in local minima or maxima. Gradient methods necessitate many iterations from various starting points to determine the position of a global optimum.

Furthermore, for non-gradient based methods, it is possible to develop a viable solution in a short amount of time, but there is no assurance that it will always identify the most optimum answer. Instead, a number of viable options present themselves. Approaches that focus on genetic adaptation and those that emphasize social behaviour make up the other categories for the methods. In the case of electrical machine design, genetic algorithms are among the most common types of optimization approaches employed [43]. According to [44], the *Non-Sorted Genetic Algorithm* (*NSGA-II*) and the *Particle Swarm Objective* (PSO) are two kinds of social behaviour techniques that are commonly used to imitate natural events. Both of these types are social behaviour approaches that mimic natural phenomena. The genetic algorithm and *NSGA-II* have many characteristics in common; however, *NSGA-II* offers a more expedient mechanism for sorting, a more effective way for

managing constraints, and it considers all vectors to be non-dominant. *NSGA-II* is widely applied in the design of electric machines [45, 46]. *Particle Swarm Objective* is used to multi-objective challenges in which the objective function comparison takes into account parameter superiority, but then another optimizer is required to set the parameters [47, 48].

Powell [49] and quasi-Newton [50, 51] are two simple optimization algorithms commonly used in electrical machine designs. Powell's approach is a non-gradient method, whereas quasi-Newton is a gradient method. In this thesis, we use two optimization techniques. We make use of *coordinate descent (accent)* and a well known optimization package, called *VisualDoc* to optimize the proposed RSGs. In *VisualDoc*, we use *NSGA-II* as the optimization algorithm.

6.1. Linking VisualDoc and SEMFEM

The choice of optimization package used in this thesis was initialized by Vanderplaats R&D [35]. It gives us the ability to integrate our Python-based *SEMFEM* simulation with a wide range of optimization techniques. Fig. 6.1 shows the optimization process in simple terms. When making use of *VisualDoc*, the following initial steps are made as shown in Fig.6.1:

- Input initial values for all the design parameters.
- Identify relevant constraints that need to be achieved.
- Describe the optimization objectives.

Moreover, as soon as this procedure for initialization has been finished, *VisualDoc* will initiate the iterative process of altering the design parameters. These are the parameters that direct the actual design of the RSG and are optimized by the optimization method. They regulate how the RSGs should be constructed. These parameters are then saved into a text file referred to as *inputfile.txt* in Fig.6.1, which are then used as inputs for the *SEMFEM* Python script. Every single FE simulation will make use of them. For each iteration, the FEM-simulation generates a file referred to as *outputfile.txt* file with the desired performance data. *VisualDoc* uses these parameters as design requirements and constraints for the current iteration. The optimization will terminate once the objectives are reached, well within constraints, and the solutions have converged. If not, *VisualDoc* alters the design variables sufficiently to restart the loop.

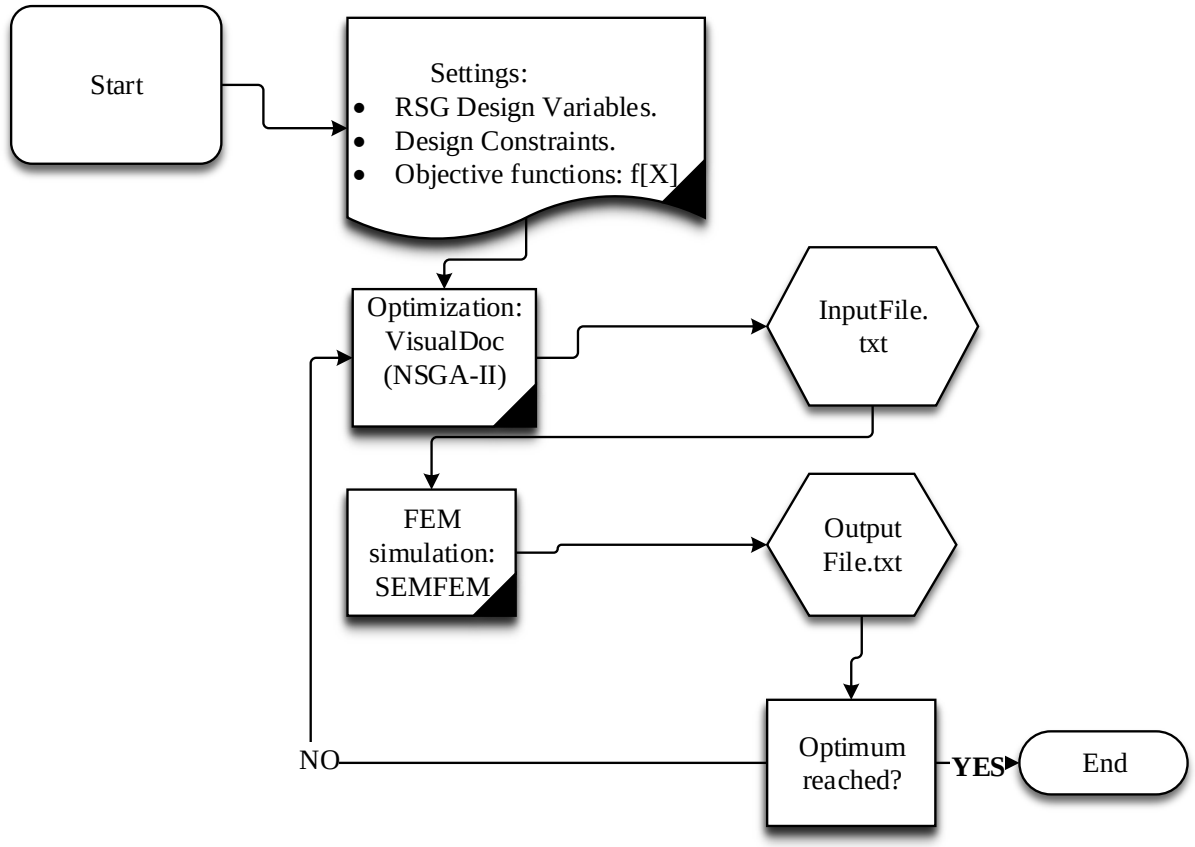

Figure (6.1) Integrating SEMFEM and VisualDoc.

6.2. Design Optimization Using Coordinate Descent

In this study for the multi three-phase design, a reasonable optimum design of the single three-phase winding RSG (S-RSG) is first obtained. This design is then used in the performance comparison between the single- and triple three-phase winding RSGs (T-RSG).

For the design optimization of the S-RSG, the coordinate descent (ascent) optimization method is used. It has been proven in [38] that the coordinate descent approach is particularly quick for minimizing or maximizing performance characteristics of electrical machines, and it constitutes the first stage in Powell's non-gradient method [52]. As a result, the following application of the coordinate descent approach is used to achieve maximum generator torque:

In the optimization the generator is optimized within a given outer stack volume. The dimensional vector [X] of the generator that is optimized is given by

$$[\mathbf{X}] = [R_{tw} \quad R_{yw} \quad R_{th} \quad S_{yh} \quad S_{tw} \quad S_{ir} \quad \phi]^T, \tag{6.2}$$

where the dimensions are explained in Fig. 6.2. Further in the design optimization, the

current density is kept constant at $J = 6\ A/mm^2$, which is a well known rated current density for standard, totally enclosed, small induction machines.

The objective function of the optimization is to maximize the torque of the RSG, that is

$$F[\mathbf{X}] = T[\mathbf{X}]_{max}, \tag{6.3}$$

subject to the following contraints:

$$\begin{bmatrix} \text{Current density} \\ \text{Stator outer diameter} \\ \text{Stack length} \\ \text{Air-gap length} \end{bmatrix} = \begin{bmatrix} J \\ d_o \\ L \\ d_{ag} \end{bmatrix} = \begin{bmatrix} 6 & A/mm^2 \\ 260 & mm \\ 125 & mm \\ 0.45 & mm \end{bmatrix}. \tag{6.4}$$

The torque of (6.3) is calculated by FEA according (3.3). The power factor and torque ripple are also calculated according (3.4 - 3.5) and (3.13) respectively. The power factor and torque ripple are very important performance parameters and hence are monitored during the optimization. The optimum dimensions obtained from optimization for the single three-phase RSG are given in Table 6.1.

In addition, just one parameter of (6.2) is varied at a time in order to find the optimal torque for S-RSG. Fig. 6.3 shows an example of this method for the rotor tooth height (R_{th}) of the S-RSG.

1. To begin, the starting point is determined by the torque that is computed based on the preliminary machine specifications, i.e. ΔT_0.

2. The relevant dimension in (6.2), which is, the R_{th} in this example is then expanded by a discrete value, δ. A new torque is computed, and the result is utilized to select the direction that maximizes torque. Thereby considering whether the new R_{th} should be at $\delta + 1$ or $\delta - 1$.

3. The torque is then determined for each subsequent $R_{th_n} = R_{th} \pm n\delta$ until the absolute maximum torque has been surpassed. Additionally, it is important to note that the later is subject to within the boundaries of the RSG.

4. Knowing that the maximum torque value lies between Δ_{Tn}, Δ_{Tn-1}, and Δ_{Tn-2}, and that these numbers and parameters encompass the maximum solution, a second-degree polynomial can be given by the following expression

   $$f_2(y) = c_x + c_y(y - y_1) + c_z(y - y_1)(y - y_2) \tag{6.5}$$

   Rewriting eqn (6.5) in terms of Δ_T and R_{th} results in the following:

   $$\Delta_T(R_{th}) = c_x + c_y(R_{th} - R_{th_{n-1}}) + c_z(R_{th} - R_{th_{n-1}})(R_{th} - R_{th_{n-2}}), \tag{6.6}$$

   where the coefficients c_x, c_y and c_z are given by

   $$c_x = \Delta_{Tn-2}, \tag{6.7}$$

$$c_y = \frac{\Delta_{Tn-2} - \Delta_{Tn-1}}{R_{th_{n-2}} - R_{th_{n-1}}}, \tag{6.8}$$

and

$$c_z = \frac{c_2}{R_{th_{n-2}} - R_{th_n}} - \frac{\Delta_{Tn-1} - \Delta_{Tn}}{(R_{th_{n-1}} - R_{th_n})(R_{th_{n-2}} - R_{th_n})}. \tag{6.9}$$

5. Using eqn (6.6) to (6.9), the maximum torque, $\Delta_{T_{max}}$, is obtained by

$$\Delta_{T_{max}} = \frac{1}{2}(R_{th_{n-1}} + R_{th_n} - \frac{c_y}{c_z}), \tag{6.10}$$

and subsequently, we determine a new parameter for R_{th}.

6. In order to complete the initial iteration, steps 1 to 5 are repeated for all the variables in eqn (6.2).

7. Finally, to complete the process, each iteration is repeated until the maximum torque, Δ_T, converges to a maximum value.

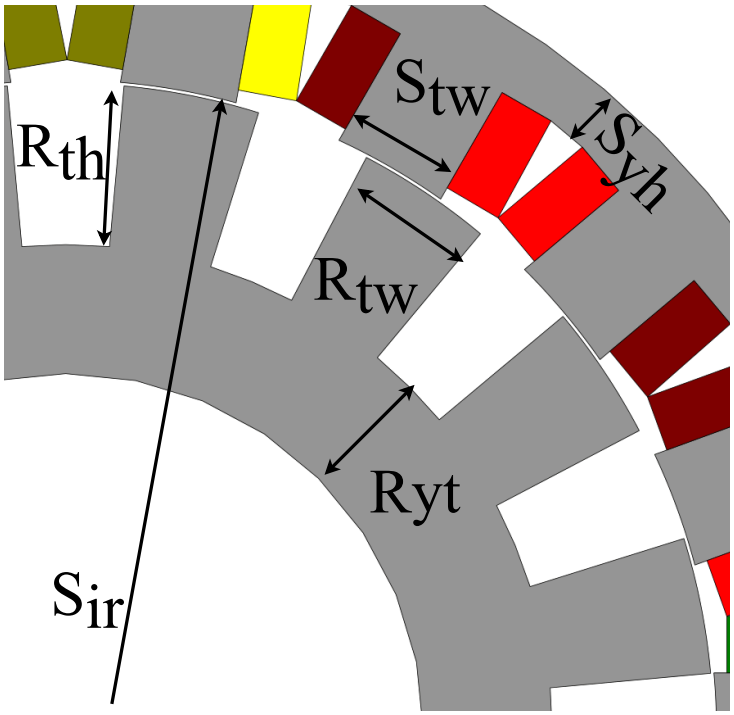

Figure (6.2) Cross-section of the proposed RSG showing optimization design parameters.

Table (6.1) OPTIMUM DIMENSIONS.

Variable	Description	Value (mm)
R_{tw}	Rotor tooth width	16.98
R_{yw}	Rotor yoke width	13.313
R_{th}	Rotor tooth height	21.2
R_{ir}	Rotor inner radius	64.163
S_{yh}	Stator yoke height	6.3125
S_{tw}	Stator tooth width	17.81
S_{ir}	Stator inner radius	99.1875

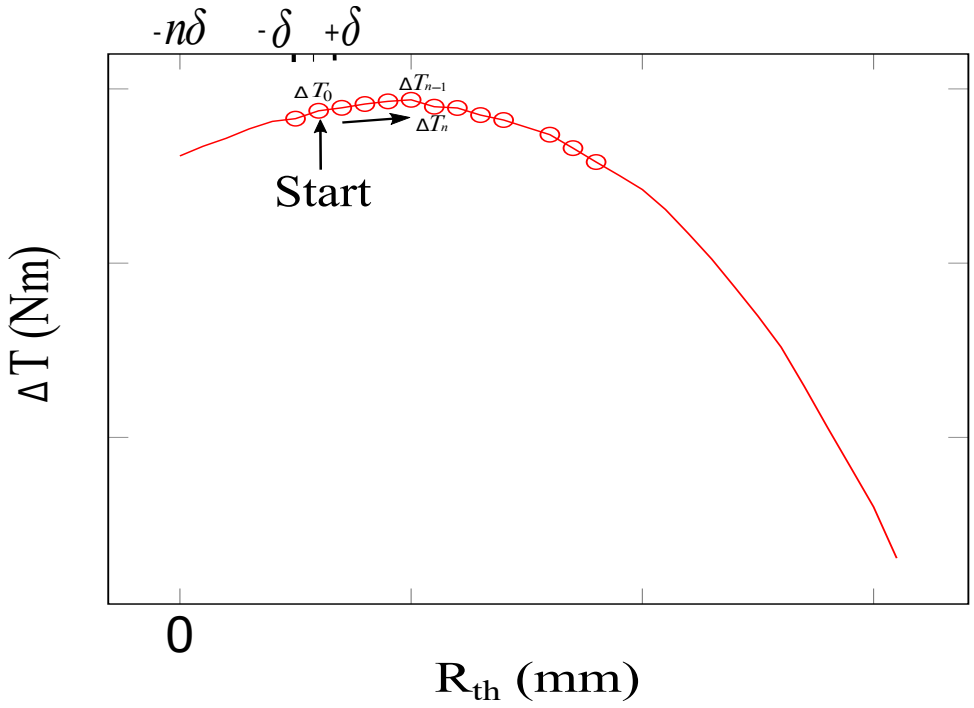

Figure (6.3) Discrete single parameter iteration to maximize torque.

6.3. Design Optimization using NSGA-II (E-RSG)

In this thesis, a commercial optimization software package developed by Vanderplaat R&D, called, *VisualDoc*, was used in the optimization process to optimize the design of the proposed generators (E-RSG). This was done through *VisualDoc* iteratively interacting with the inputs and outputs of the provided python script, which further ran the *SEMFEM* simulations. In order to optimize the RSGs, the multi-objective *NSGA-II* optimization algorithm was used. Furthermore, the optimization of the generators was performed within a given outer stack volume and optimized only the main dimensions [**X**] of the generators, as given by (6.11), shown in Fig. 6.4 and further explained in Table 7.2. The objective function of the design optimization is given by (6.12) and was used to obtain the torque density versus power factor Pareto front.

$$[\mathbf{X}] = [S_{sw} \quad S_{ir} \quad S_{gh} \quad a_r \quad R_{ib} \quad \phi]^T, \tag{6.11}$$

$$f[\mathbf{X}] = \begin{bmatrix} T_{\mathrm{d}} \\ P_{\mathrm{f}} \end{bmatrix}_{max}. \tag{6.12}$$

The objective function is subject to the following constraints:

$$\begin{bmatrix} \text{Current density } (J) \\ \text{Stator outer diameter } (d_o) \\ \text{Stack length } (L) \\ \text{Air-gap length } (d_{ag}) \\ \text{Fill factor } (f_f) \end{bmatrix} = \begin{bmatrix} 4.2\,\mathrm{A/mm^2} \\ 1.89\,\mathrm{m} \\ 1.89\,\mathrm{m} \\ 2.5\,\mathrm{mm} \\ 0.6 \end{bmatrix}. \tag{6.13}$$

In addition, the optimum machine was chosen based on the criteria given by

$$\begin{bmatrix} \text{Efficiency} \\ \text{Power output} \\ \text{Power factor} \\ \text{Torque ripple} \end{bmatrix} = \begin{bmatrix} E_f \\ P_o \\ \phi_x \\ T_r \end{bmatrix} = \begin{bmatrix} \geq\ 98\% \\ \approx\ 5\,\mathrm{MW} \\ \approx\ 0.7 \\ \leq\ 5\% \end{bmatrix}. \tag{6.14}$$

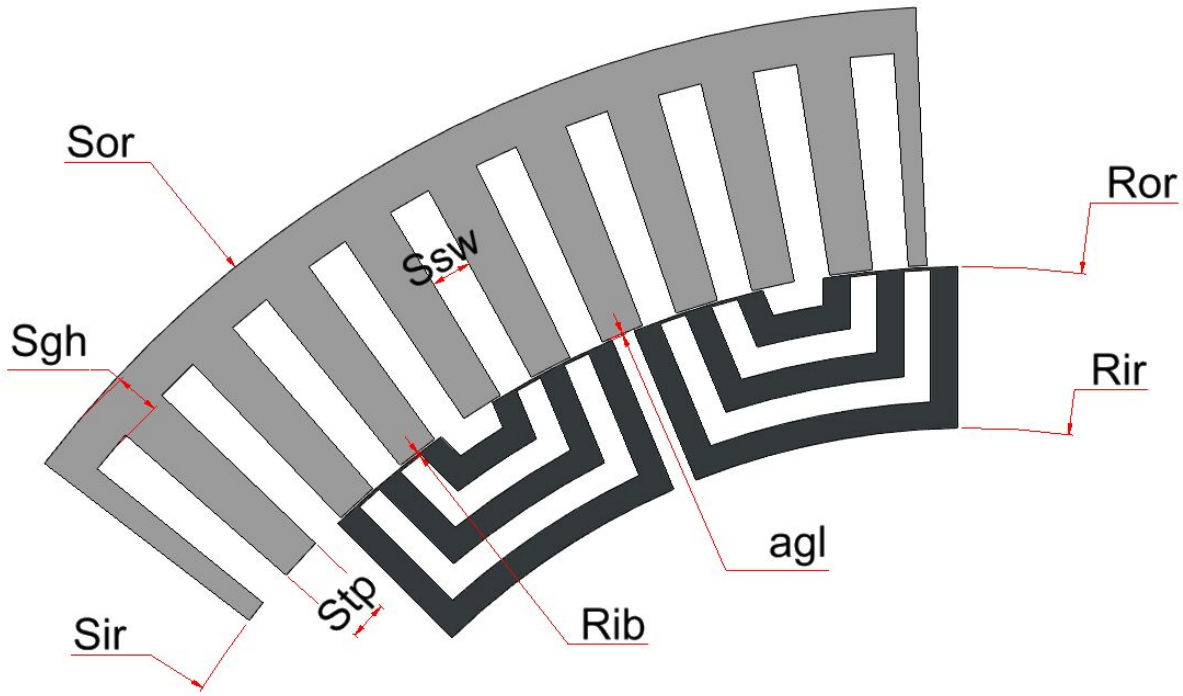

Figure (6.4) Cross-section showing the optimization design parameters.

6.4. Chapter Summary

This chapter describes the optimization techniques and algorithms used in this thesis. The Coordinate descent optimization (used for S-RSG) proved to be simple and extremely fast providing a near optimum, satisfactory design. Moreover, the *VisualDoc* optimization suite that uses the *NSGA-II* is used for the E-RSG, which will be demonstrated in the next chapter.

Chapter 7

High Pole Number Epoxy-Casted Rotor RSGs (E-RSG and SE-RSG)

To ensure a reasonable power factor, this chapter proposes a modular epoxy-casted reluctance rotor (E-RSG) for a 16-pole, 375 r/min, 5-MW wind generator. The 5-MW wind generator system is shown in Fig. 1.1, consisting of a medium-speed gearbox with a gear ratio of between 25 and 30, and a 16-pole RSG that is connected to the grid via a solid-state power converter. A fractional-slot stator winding was considered for the 16-pole RSG, which was shown to reduce torque ripple in RSMs [28].

A critical aspect to determine in the design optimization is the torque density versus power factor characteristic of the RSG. From this, a design was achieved at the highest possible torque density. Fig. 7.1 shows the focus of this chapter.

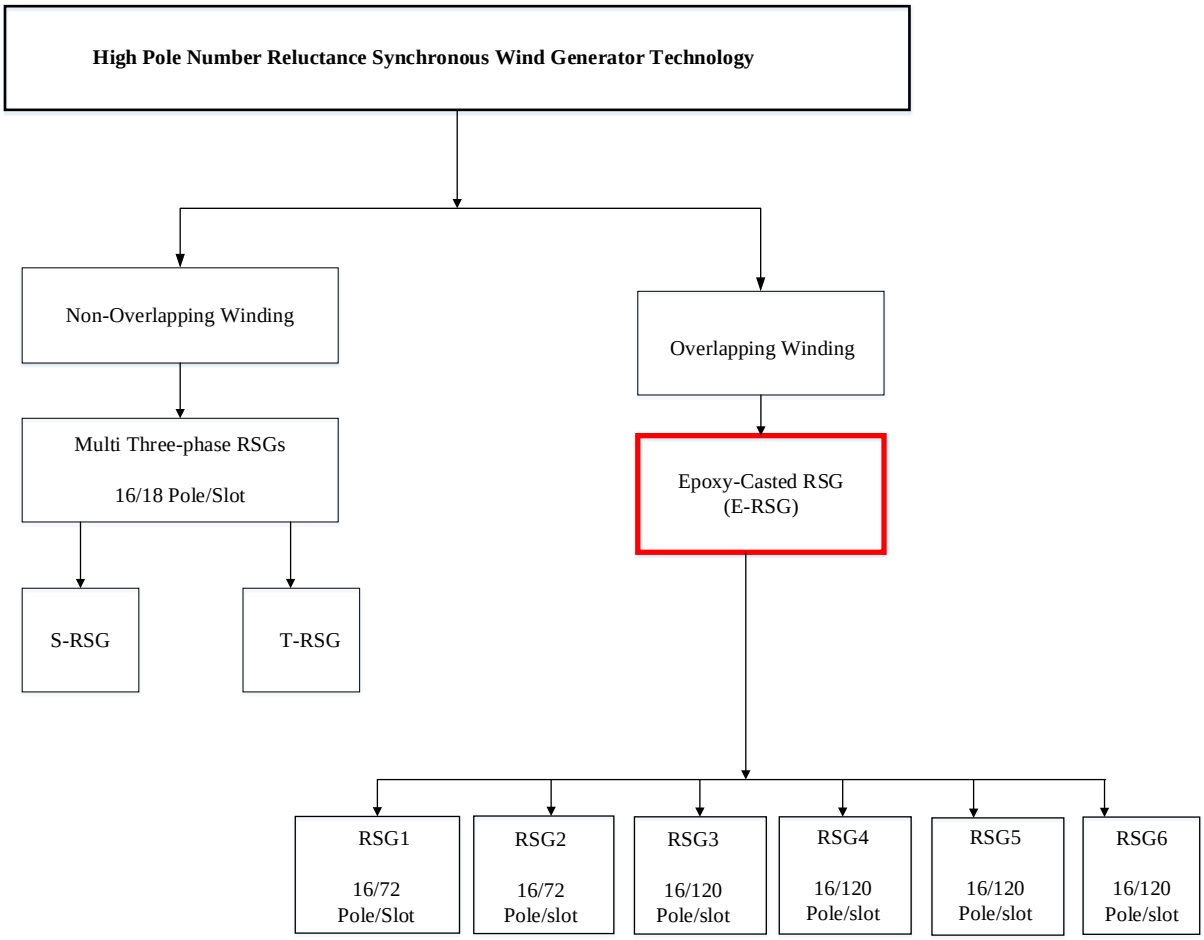

Figure (7.1) High pole number RSG design layout showing the chapter focus.

7.1. Epoxy-casted RSG Design Layout

The cross-sectional design layouts of the initially proposed epoxy-casted rotor RSGs are shown in Fig. 7.2. The RSGs have a double layer, overlapping stator winding configuration with a 16/72 pole/slot combination. The *abc* three-phase slot coils are indicated in Fig. 7.2 by dark and light brown, yellow and green colors respectively. The study took a look at two initial rotor designs, shown in Fig. 7.2(a) and (b). The difference lies in the uneven and even spacing of the iron and epoxy (flux barrier) along the air-gap.

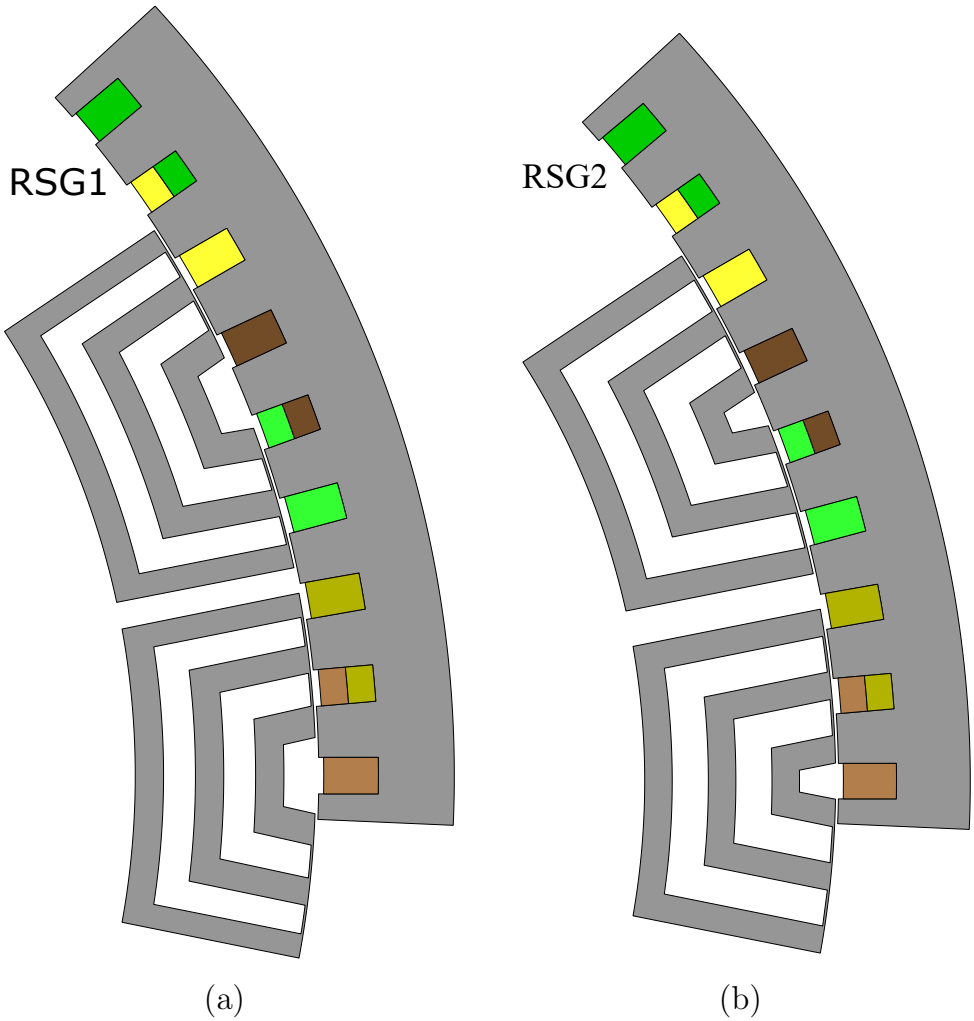

Figure (7.2) FEA cross section 16/72 pole/slot combination RSGs with (a) uneven iron-to-air rotor (RSG1) and (b) even iron-to-air rotor (RSG2).

7.2. Optimum Design and Performance of RSG1 and RSG2

The Pareto front optimization results of RSG1 and RSG2 of Fig. 7.2 are shown in Fig. 7.3. The best machine, RSG1, was selected from the Pareto fronts according to the torque criteria of (6.14), as shown in Fig. 7.3.

Fig. 7.4 shows the waveforms of the torque versus rotor position of the optimum selected unskewed RSG1 using two finite element analysis (FEA) packages, namely the static FE (*SEMFEM*) and transient FE (Ansys Maxwell) packages. As can be seen from Fig. 7.4 and given in Table 7.1, the average torque and torque ripple calculated by both FE packages were comparable. The calculated core losses in Table 7.1 also show good correlation between *SEMFEM* and Ansys-Maxwell. However, the performance results of RSG1 in Table 7.1 show that the criteria, for power factor and torque ripple, of (6.14) were not entirely met.

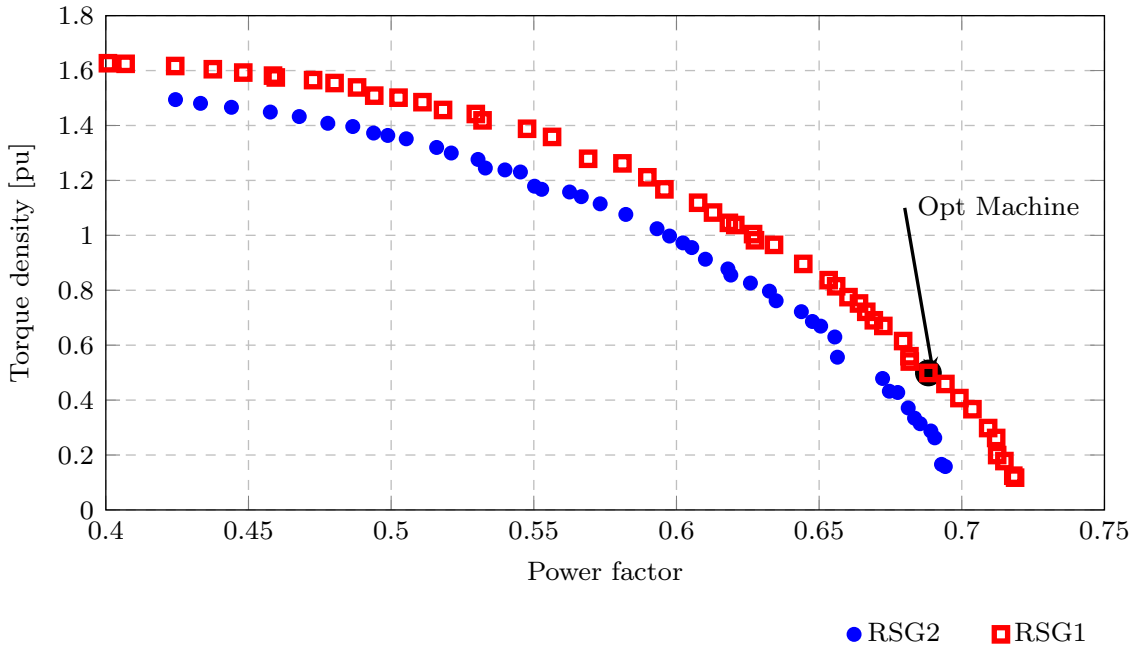

Figure (7.3) Pareto fronts of RSG1 and RSG2 of Fig.7.2 showing the 5-MW optimum point.

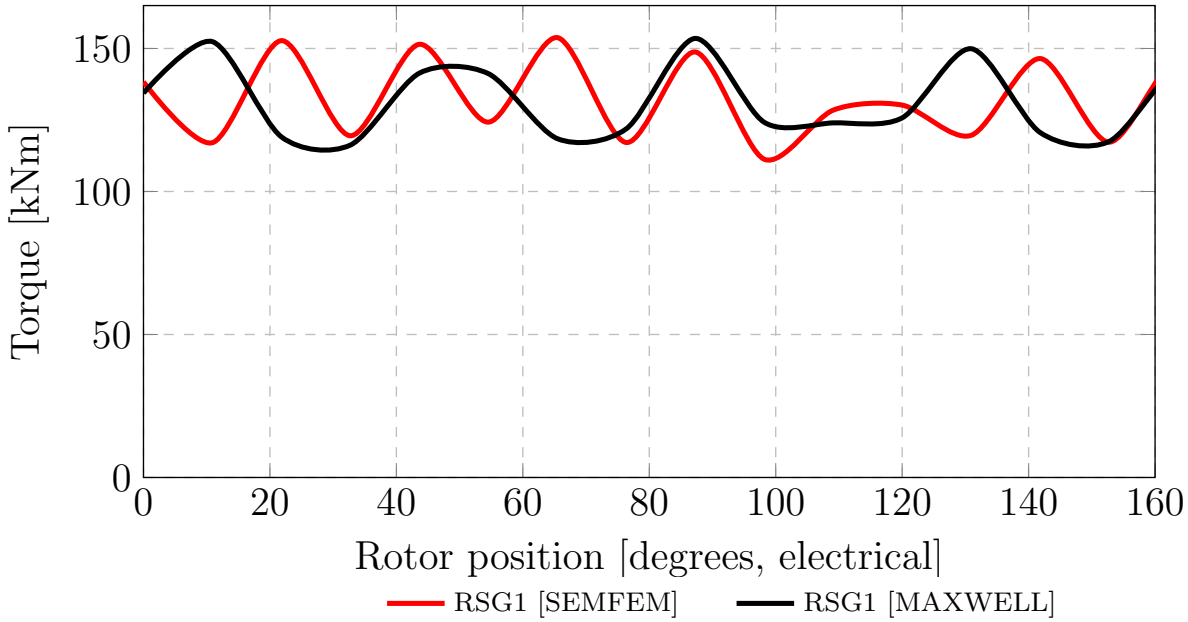

Figure (7.4) Comparison of calculated torque versus rotor position of the unskewed RSG1 using two FE packages.

Table (7.1) Optimum FEA Performance Of Unskewed RSG1

Performance parameter	*SEMFEM*	*MAXWELL*
Power out [MW]	5.09	-
Power factor	0.677	-
Efficiency [%]	97.3	-
Torque average [kNm]	132	130
Torque density [kNm/m^3]	24.9	277
Torque ripple[%]	40.8	38.2
Rotor core loss [kW]	9.33	8.8
Stator core loss [kW]	26.0	24.8
Total core loss [kW]	35.4	33.6

7.3. Design Optimization of High Slot Number RSG3

Given that RSG1 in the initial design in Section 7.2 did not meet the criteria in (6.14), we further investigated the effect of a higher stator slot number on the performance of the RSG. For this, we considered RSG3 with a 16/120 pole/slot combination and used the rotor of RSG1, as shown in Fig. 7.5(a). Previous studies have shown that a higher stator slot number can be beneficial in improving machine performance [21].

The optimization of RSG3 in this section was done using the same method as described in Section 6.3. Fig. 7.6 shows the torque versus power factor Pareto front of RSG3, also showing the efficiency color-gradient distribution (red – maximum; blue – minimum). From this Pareto front, an optimum machine was chosen, as in Fig. 7.6. The optimum dimensions of RSG3 are given in Table 7.2.

In addition, Fig. 7.7 shows the torque versus rotor position of RSG1 and RSG3. The overall performance results of RSG3 are also given in Table 7.3, to be compared with those of RSG1 in Table 7.1. From this it is shown that the increase in stator slots reduced the torque ripple by 50% and increased the power factor by 5.7%. Although RSG3 had an improved performance in torque ripple and power factor, the criteria of (12) was still not met in terms of torque ripple. Also, important to note from Tables 7.1 and 7.2 is the drastic increase in stator core losses of RSG3 compared to RSG1. This is due to increased flux pulsations in the stator teeth.

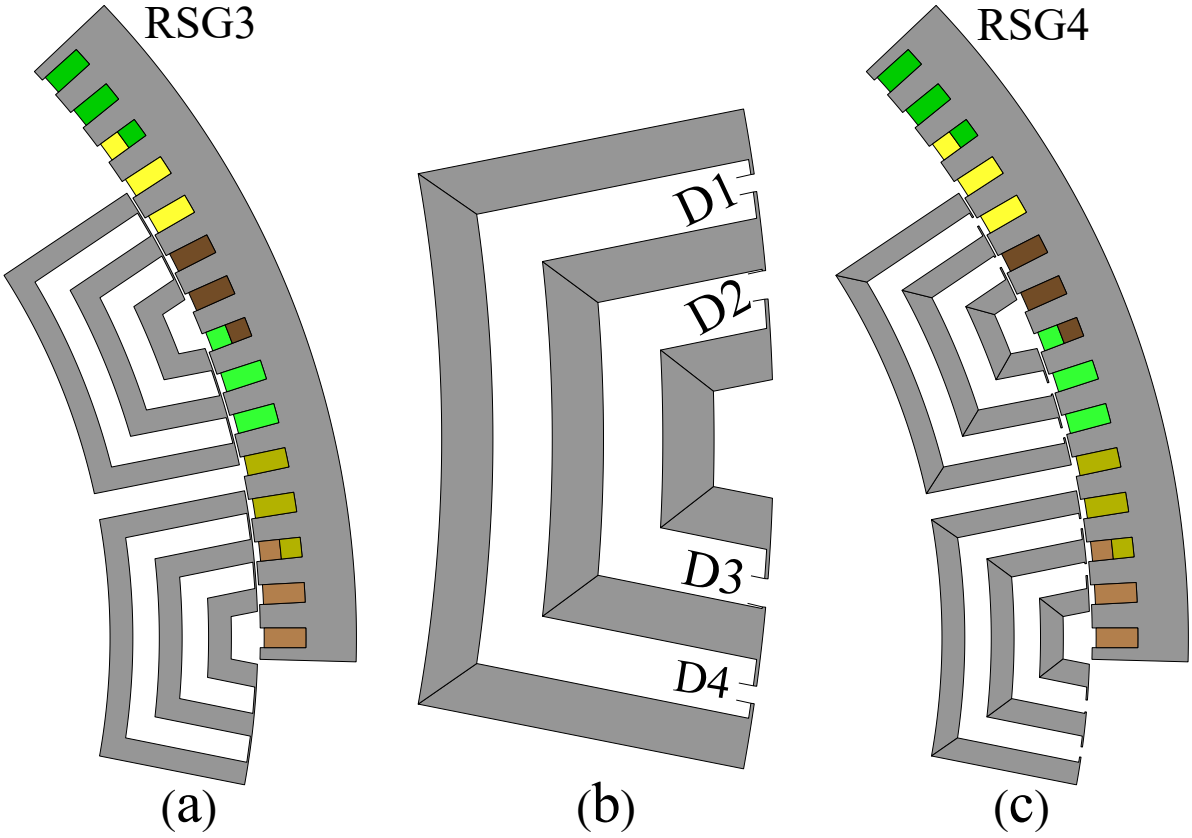

Figure (7.5) Optimized cross sections of (a) RSG3, (b) slitted rotor pole piece of RSG4 showing optimized slitted-rib variables and (c) optimized RSG4 with slitted rotor.

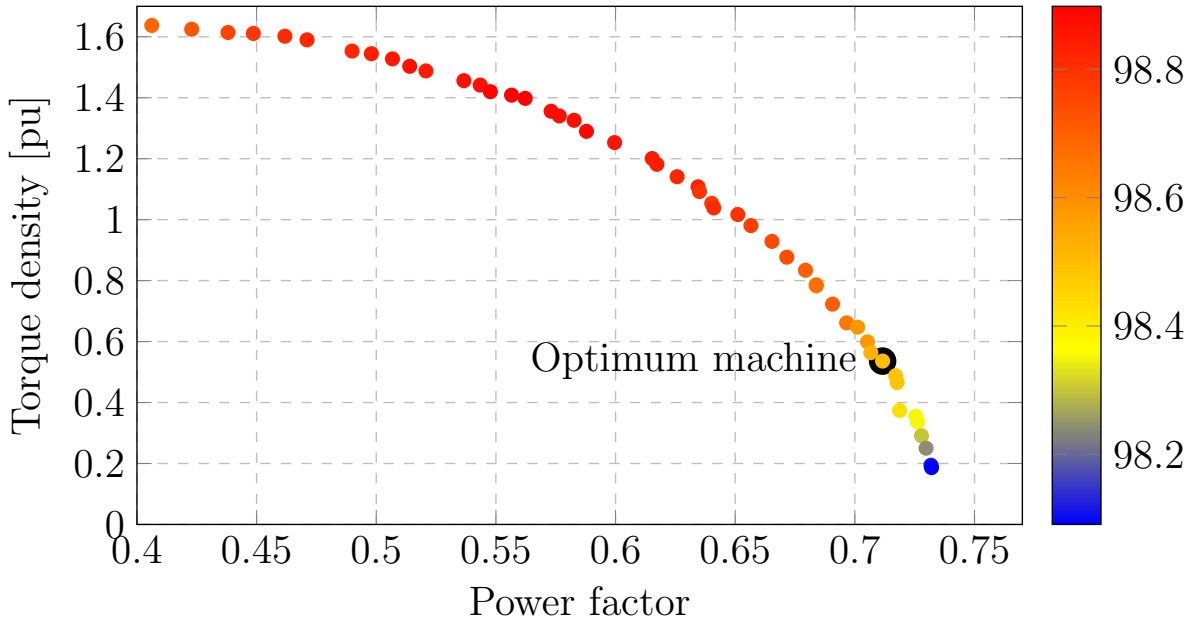

Figure (7.6) Pareto front with efficiency color-gradient distribution (red - maximum; blue – minimum) of RSG3.

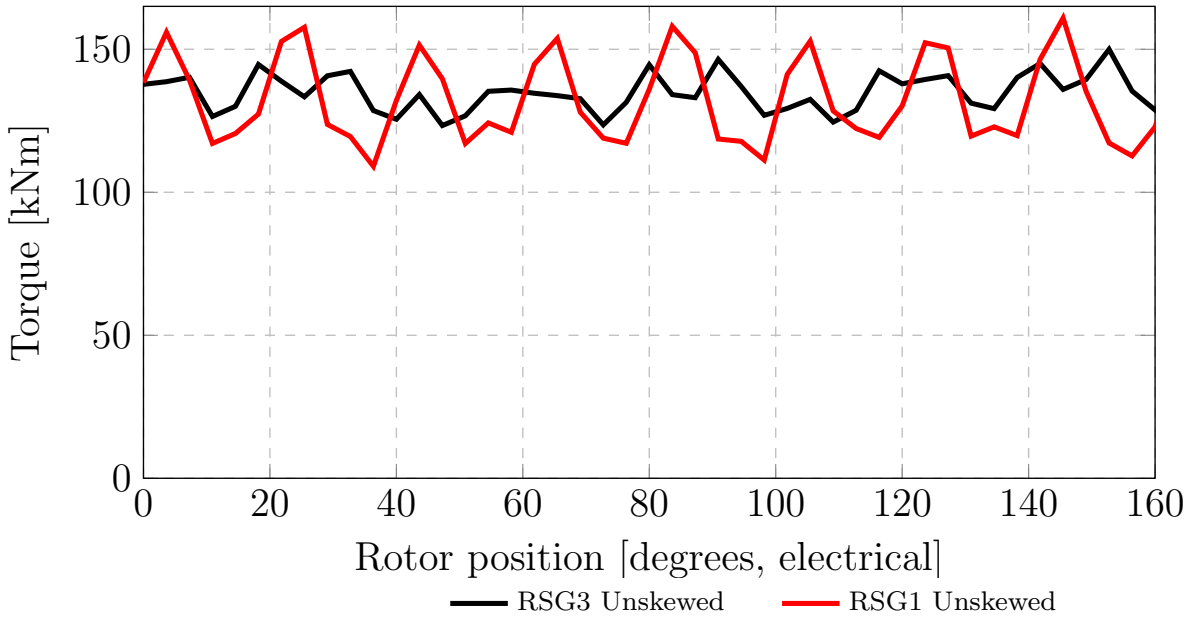

Figure (7.7) Torque versus rotor position of unskewed RSG1 and RSG3.

7.4. Optimization of Slitted-Rib Rotor RSG4

To reduce flux leakage in the rotor ribs and further improve the power factor of RSG3, we considered slitting the rotor ribs of RSG3, as shown in Fig. 7.5(b). The rib slits were optimized in terms of width and position by maximizing the power factor and minimizing the torque ripple, whilst keeping the optimum dimensions of RSG3 constant as in Fig. 7.5(a) and (c). The Pareto front result of this optimization of torque ripple versus power factor is shown in Fig. 13. As indicated in Fig. 7.8, we selected the design with the highest power factor for RSG4, with the aim to reduce torque ripple by rotor skewing while still maintaining a power factor that meets the criteria of (6.14). The optimum slit dimensions and performance of the unskewed RSG4 are given in Tables 7.2 and 7.3 respectively.

Although RSG4 showed an improvement in power factor, it still did not achieve the criteria of (6.14) due to its high torque ripple. Also, the slightly higher stator core losses remained an issue and needed to be minimized.

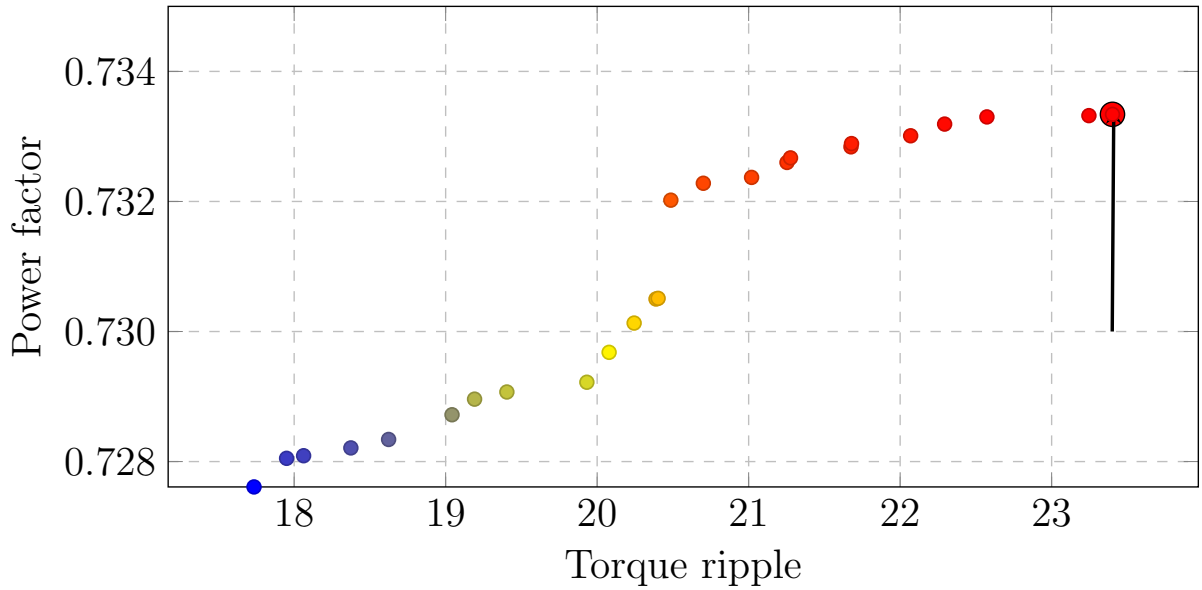

Figure (7.8) Pareto front of the slitted rotor ribs of RSG4 of Fig.7.5(c).

7.5. Optimization of High Flux Barrier Number Rotor RSG5 and RSG6

In an attempt to reduce core losses and further reduce torque ripple, we increased the number of flux barriers on the rotor from three to six, as shown in Fig. 7.9(a). The advantages of increasing the number of flux barriers in RSMs were previously documented by [53].

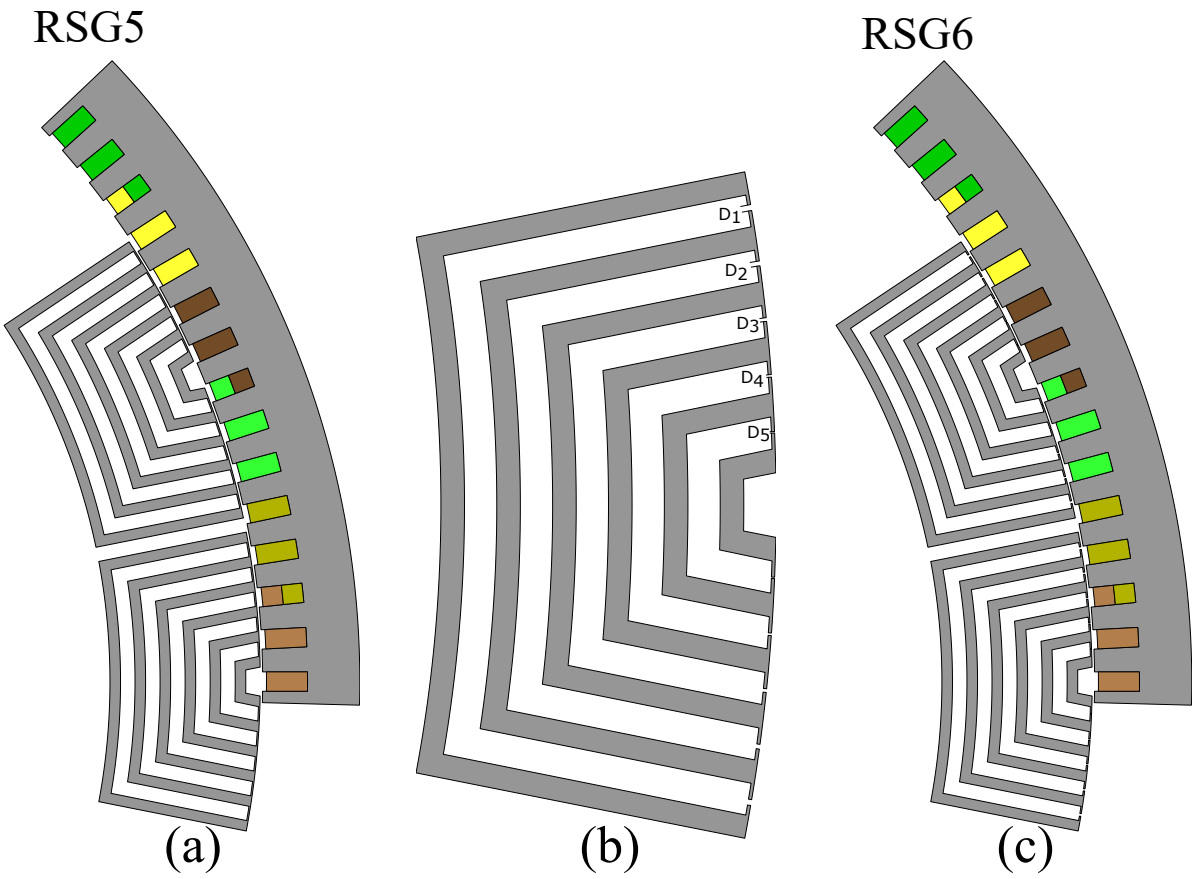

Figure (7.9) Optimized cross sections of (a) RSG5, (b) slitted rotor pole piece showing optimized variables and (c) RSG6.

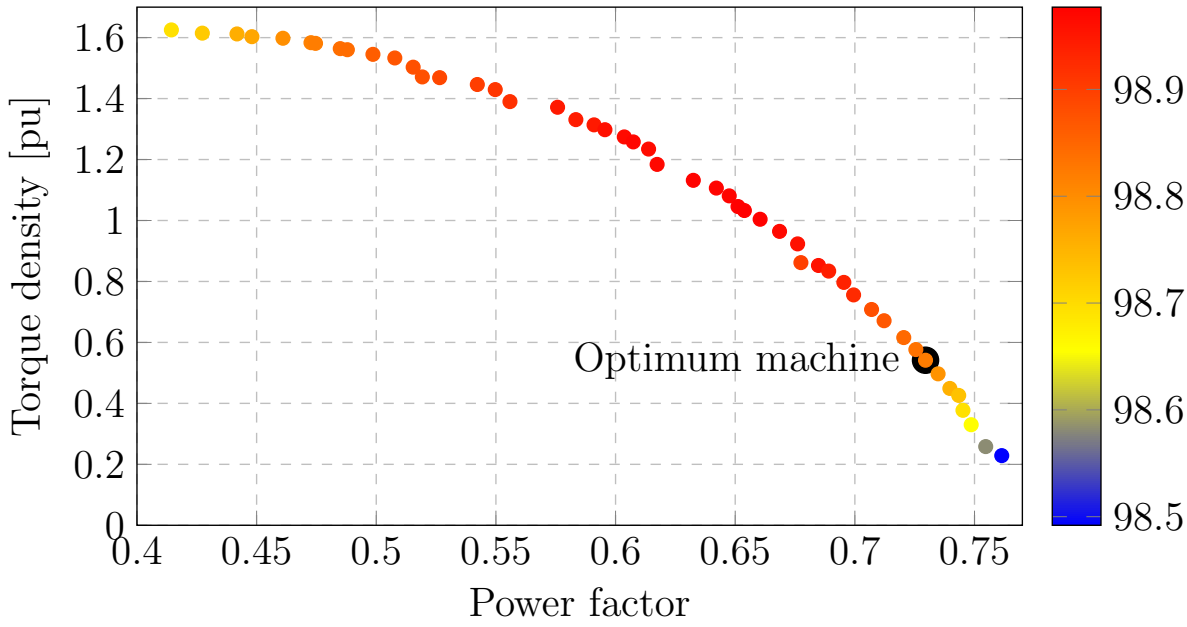

Figure (7.10) Pareto front efficiency color-gradient distribution (red - maximum; blue - minimum) of the 16/120 pole/slot combination of RSG5 in Fig. 7.9(a).

By re-optimizing the 16/120 pole/slot RSG with the higher number of rotor barriers, the Pareto front optimization result in Fig. 7.10 was obtained, showing the efficiency

color-gradient distribution and the selected RSG5 design. The optimum dimensions and performance of the unskewed RSG5 are given in Tables 7.2 and 7.3 respectively. It is evident from Table 7.3 that, by increasing the number of rotor flux barriers drastically, the stator core losses in RSG5 were reduced. The percentage torque ripple of RSG5, although much lower, was still not meeting the criteria of (6.14).

To see if the performance of RSG5 could be improved further, the method of rotor rib slitting was applied again, this time on the high flux-barrier-number rotor of RSG5 in Fig. 7.9(a). The result of this rotor slitting is shown in Fig. 7.9(b), which now is the rotor of RSG6, as shown in Fig. 7.9(c). The dimensions and optimum slit widths of RSG6 are given in Table 7.2, while its performance is given in Table 7.3. The performance results of the slitted rotor RSG6 in Table 7.3 show a very good improvement in power factor and a good reduction in core losses and torque ripple. However, the torque ripple requirement of (6.14) were still not met.

Table (7.2) Optimum Dimensions of RSG3 to RSG6

Var	Description	RSG3	RSG4	RSG5	RSG6
S_{ir}	Stator inner radius [mm]	833	835	843	843
S_{gh}	Stator yoke height [mm]	62.1	62.1	54.8	54.8
S_{sw}	Stator slot width [m]	16.7	16.7	10.1	10.1
Y	Rotor iron width [mm]	20.7	20.7	11.1	11.1
L	Rotor air width [mm]	23.7	23.7	15.7	15.7
R_{ib}	Rib height [mm]	1.65	1.65	1.60	1.60
R_{ir}	Rotor inner radius [mm]	680	680	684	684
D_1	Slit $width_1$ [mm]	-	8.09	-	2.36
D_2	Slit $width_2$ [mm]	-	13.04	-	2.35
D_3	Slit $width_3$ [mm]	-	13.0	-	1.49
D_4	Slit $width_4$ [mm]	-	7.99	-	1.22
D_5	Slit $width_5$ [mm]	-	-	-	1.0

Table (7.3) Performance of Unskewed RSG3 to RSG6

Performance Parameter	RSG3	RSG4	RSG5	RSG6
Power out [MW]	5.10	5.24	5.10	5.10
Power factor	0.723	0.736	0.735	0.746
Efficiency [%]	98.5	98.5	98.8	98.9
Torque average [kNm]	130	134	130	131
Torque density [kNm/m^3]	24.3	25.3	24.7	24.6
Torque ripple[%]	20.4	23.4	14.5	11.4
Rotor core loss [kW]	4.53	3.69	5.03	4.27
Stator core loss [kW]	41.4	43.3	22.4	20.8
Total core loss [kW]	45.9	47.0	27.4	25.0

7.6. Reduction in Torque Ripple

In order to meet the set criteria, minimizing torque ripple to below 5%, a well-known technique of rotor-skewing was used. It was previously shown to reduce the torque ripple of RSMs [40,54]. For this, RSG1 to RSG6 are skewed and their performance are compared. An optimum skew angle of 2.5° mechanical was found across all five machines. Fig. 7.12 shows the overall skewed performance of RSG1 and RSG3 to RSG6. From this it is clear that RSG6 complies with all the requirements of (6.14). Finally, Fig. 7.11 shows the high torque quality of RSG6 in comparison to that of the unskewed RSG1 and RSG3.

Table 7.4 gives the optimum skewed results of RSG6 in comparison to the 5-MW designs of [5] and [6] as shown in Fig. 7.13. This shows the superior performance of the proposed epoxy-casted RSG6, with its higher torque density and lower active mass. Also, the AJ value of RSG6 given in Table IV is within specification.

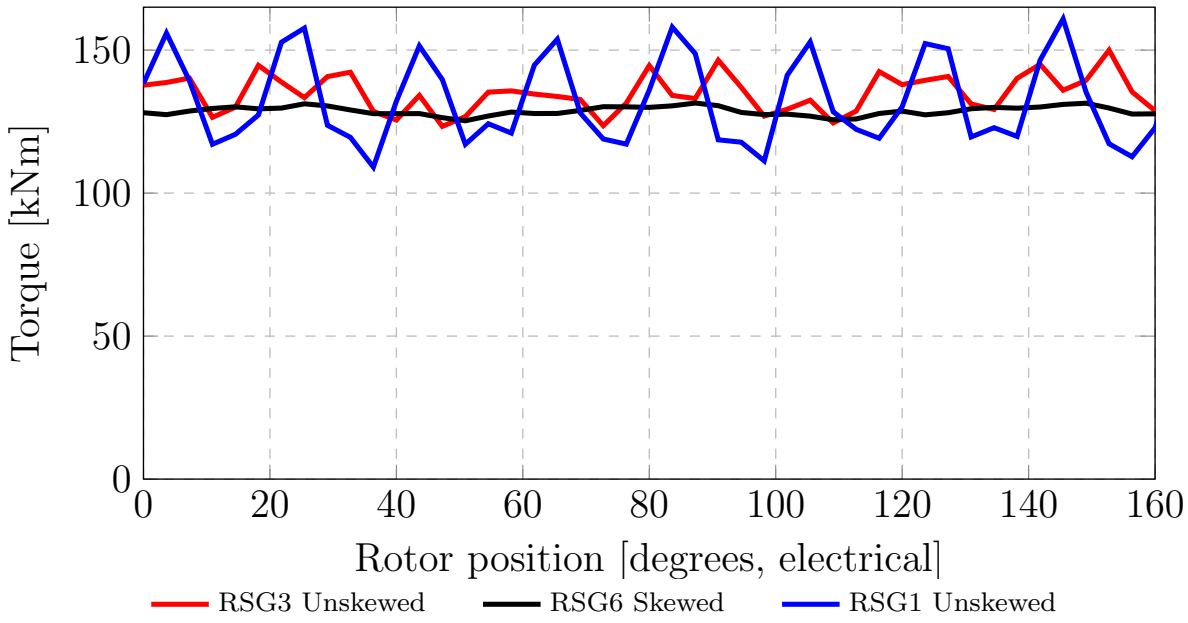

Figure (7.11) Torque ripple comparison of the unskewed RSG1 and RSG3, and the skewed RSG6 versus rotor position.

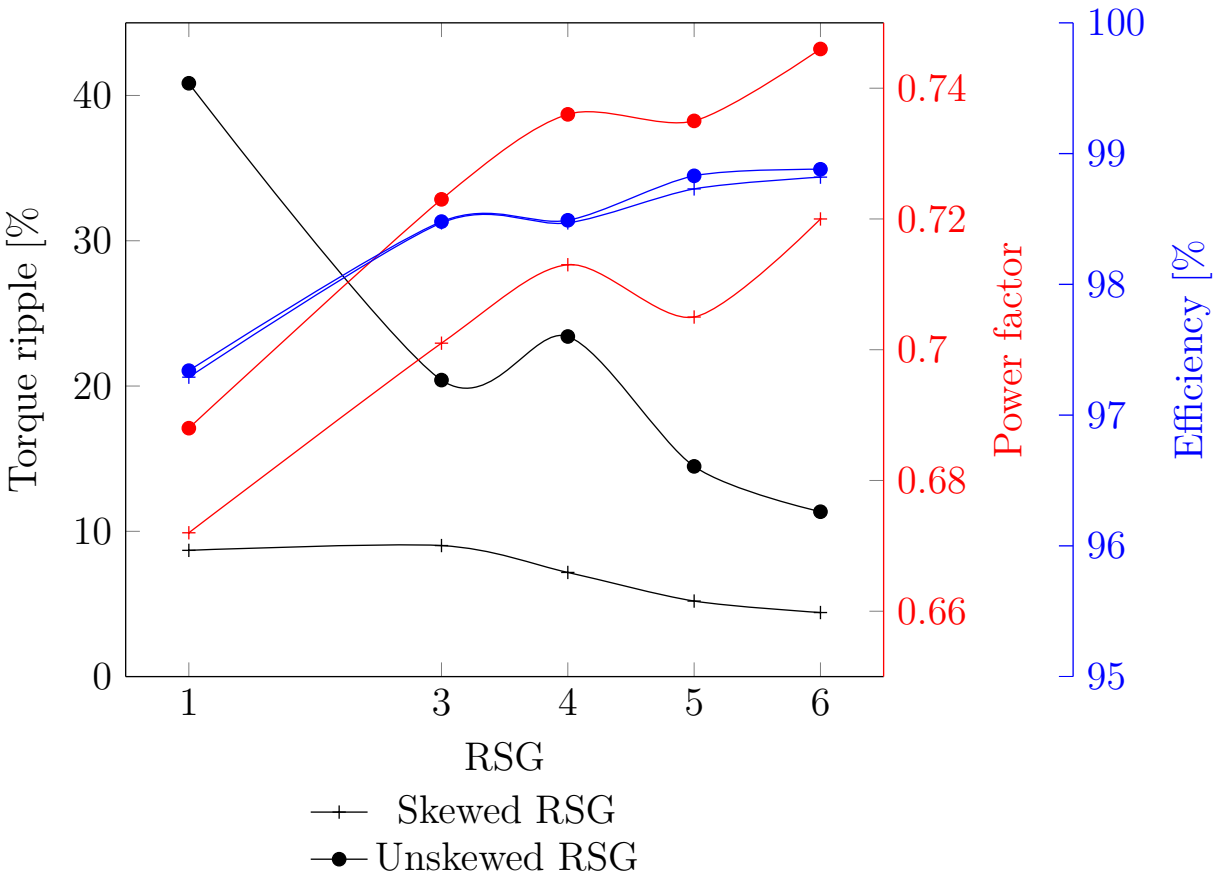

Figure (7.12) Performance of unskewed and skewed RSG1 and RSG3 to RSG6.

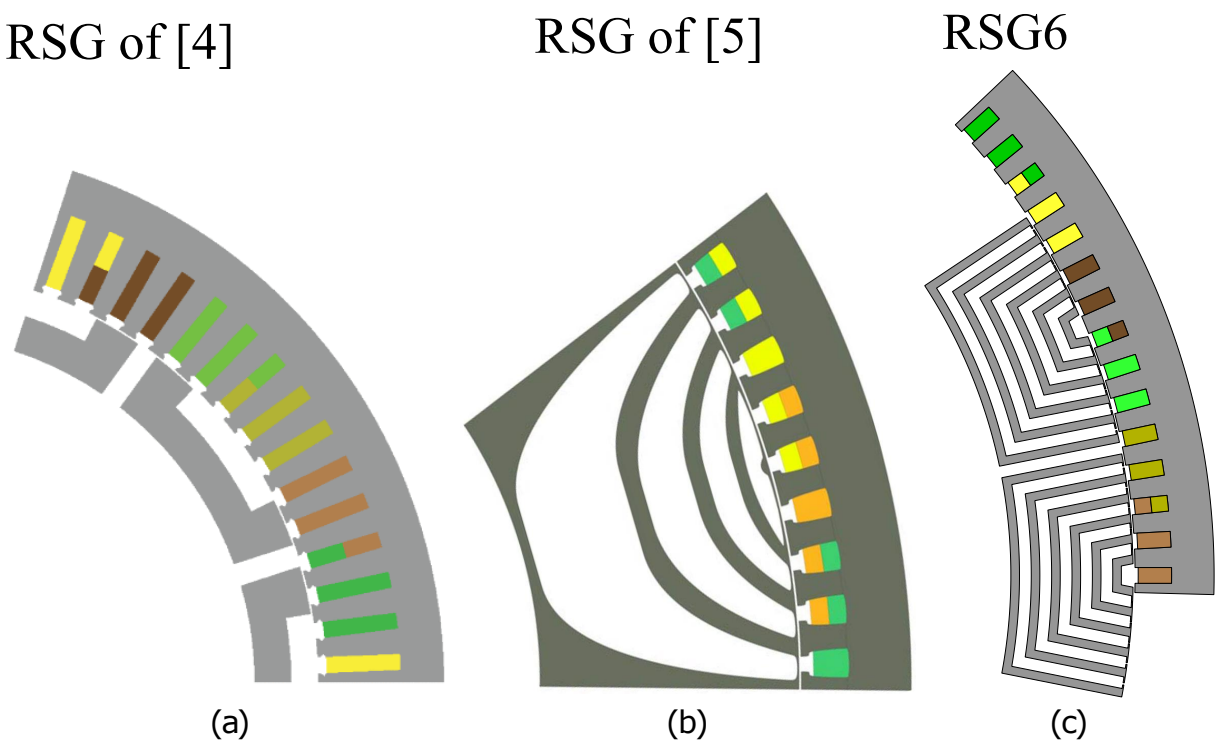

Figure (7.13) Cross-sections of 5-MW RSG designs of (a) the split-pole RSG of [6], (b) 10-pole generator of [5] and (c) RSG6.

Table (7.4) Performance of Skewed RSG6, RSG of [5] and RSG of [6]

Performance parameter	RSG of [6]	RSG of [5]	RSG6
Power out [MW]	5.03	5.05	5.0
Power factor	0.65	0.85	0.72
Efficiency [%]	98.2	98.0	98.8
Torque average [kNm]	97.9	98.4	128.1
Torque density [kNm/m^3]	18.6	18.7	24.2
Torque ripple [%]	4.82	-	4.41
Current angle [°]	63.46	73.4	78.1
Current density [A/mm^2]	1.41	4.5	4.2
Poles	10	10	16
Slots per pole	7.5	9	7.5
Fill factor	0.6	0.35	0.6
Stator diameter [m]	1.89	1.89	1.89
Stack length [m]	1.89	1.89	1.89
Air-gap [r/min]	3	2.5	2.5
Speed [mm]	500	500	375
Rotor core loss [kW]	-	-	4.60
Stator core loss [kW]	-	-	21.02
Total core loss [kW]	-	-	25.62
$L_d - L_q$ [mH]	-	-	20.93
L_d/L_q	-	5.06	7.77
AJ [A^2/m^3]	-	-	10.5×10^{10}
Active mass [t]	19.4	14.8	12.4

7.7. Mechanical feasibility

The epoxy-casted reluctance rotor in Figs. 2.6 and 2.7 is not a standardized manufacturing method of electric machine rotors. The majority of rotors have their active material directly connected to the shaft, resulting in direct torque transfer. In the proposed machine, each pole piece is held in place by the epoxy, which will experience brittle failure if overloaded. The mechanical analysis described in this section is done with the help of a colleague, Stefan Botha.

7.7.1. Stress Estimation

The stresses experienced by each rotor pole piece have two major components, namely the inducted torque of (3.3) and the radial electromagnetic attraction between the rotor and stator, given by

$$F_r = \frac{1}{2}\frac{B^2}{\mu_0}\tau l, \tag{7.1}$$

where the force is dependent on the air-gap flux density B at a pole piece and the air-gap area that consists of the axial length of the core l and the tangential length of the magnetic material at the air-gap, τ. The minor force that the rotor also experiences is the centrifugal force due to rotation as

$$F = \sum m\omega^2 r, \tag{7.2}$$

with ω being the rotational speed, m being the element mass and r being the distance to the center of the mass. The additional stress that is caused by thermal expansion and from Poisson's ratio is very small in comparison to the two major stresses, but should be included. The total stress that an element will experience is easily described by the three-dimensional Von Mises stress, which includes surface shear [55]. The maximum stress distribution that the rotor pole piece experiences can be seen in Fig. 7.14(a).

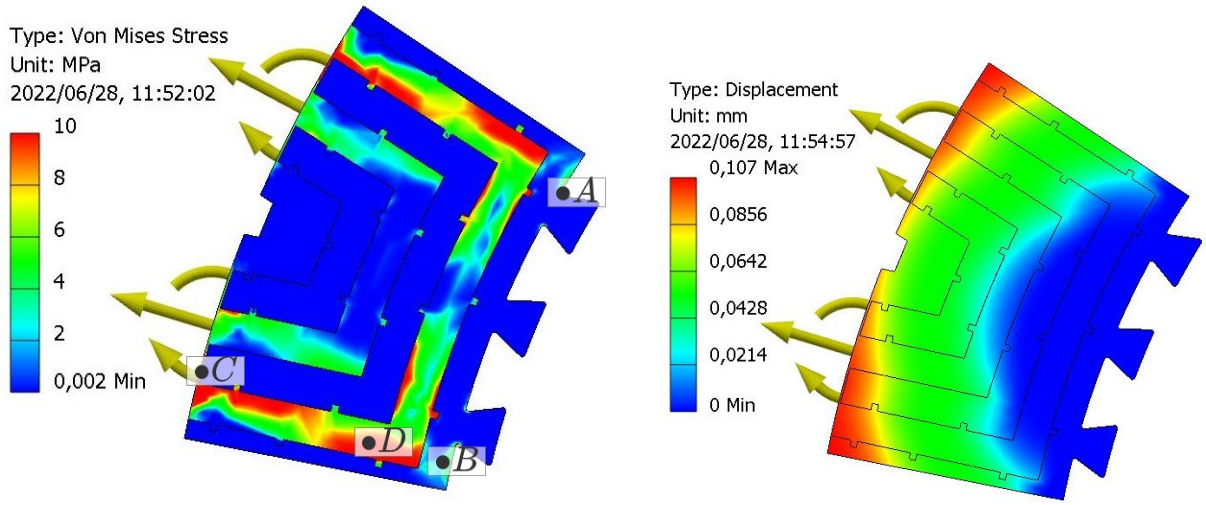

(a) (b)

Figure (7.14) 3D FEA of a single pole piece of RSG1 at (a) maximum stress and (b) deflection at maximum stress.

The Von Mises stress at a specific point must be modified further in specific areas where stress concentrations will occur. The epoxy dovetail is an example of where a notch increase factor has to be used, as described by [55].

7.7.2. Deflection at the Air-gap

Maintaining a constant air-gap distance is crucial in the stable operation of the machine. Using the three dimensional stress estimated in the previous section, the elastic strain in the radial direction is

$$\epsilon_r = \frac{\delta}{l} = \sum \frac{1}{E}[\sigma_r - \nu(\sigma_t + \sigma_z)], \tag{7.3}$$

with σ denoting the stress, δ being the total elongation over the length l, and E and ν being the Young's modulus and Poisson's ratio of each of the materials respectively. The total change in air-gap length depends on the deflection of both the rotor and stator. Using

FEA software the deflection can be visualized and compared to the analytical calculation as can be seen in Fig. 7.14(b).

The maximum deflection occurs at the maximum stress state, and the rotor deflects around 0.13 mm in the radial direction at maximum load, which is acceptable for a machine with an air-gap diameter of 1.6 m.

7.7.3. Failure Analysis

The primary concern in the analysis is the failure of the epoxy under constant cyclical stress and thermal loading. The epoxy is a brittle material that is subjected to uncertainties during the manufacturing process, such as mixing ratio and appropriate surface contact. The more conservative approach is the Brittle Coulomb-Mohr (BCM) failure theory for the epoxy and the distortion energy for the laminations [55, 56]. The epoxy will experience the most stress in a combined shear and tensile loading, which is determined in the previous section. For the electrical steel and housing, the fatigue strength should be considered as the machine experiences a large number of loading cycles. The endurance modifiers are given by [57]. Using the modified Goodman failure criteria, the safety factor becomes

$$Safety\ \ Factor = \frac{S_e}{\sigma_a} + \frac{S_y}{\sigma_m}, \tag{7.4}$$

where σ_a and σ_m are the alternating and mean stress respectively, with S_e and S_y being the Marin factors for fatigue and yield strength. If the machine is built from the proposed commercial epoxy and laminations as shown in Table 7.5, then Table 7.6 highlights the achieved safety factors for the machine in both analytical and 3D FEA approaches. The safety factor for the infinite cycles loading at max stress satisfies the basic requirements, and the pole piece is not expected to fail during operation under normal conditions.

Table (7.5) Material Properties of Epoxy and Electrical Steel

Parameter	S_{ut}	S_y	E	ν	Unit
M400-50A electrical steel	400	280	220000	0.3	MPa
EpoxAcast 670HT epoxy	31	21	2289	0.38	MPa

Table (7.6) Safety Factors For Specific Portions of The Pole Piece in Fig. 7.14

Parameter	Analytical SF	3D FEA SF
Epoxy dovetail (a)	6.4	6.98
Epoxy base (b)	11	11.7
Surface of lamination (c)	46	52.1
Lamination corner (e)	42	43.2

7.7.4. Design Optimization of a Small Scale Epoxy-Casted RSG (SE-RSG)

To test and prove design ideas, it is common practice to create a scaled prototype that mimics the features of bigger machines. In the previous sections in this chapter, large scale E-RSGs are proposed and designed to find the best possible E-RSG that suits the set criteria in the optimization chapter. In this section, a small scale, sub-2 kW E-RSG (SE-RSG) is designed. The design makes use of a 16/72 pole/slot combination with an overlapping stator winding configuration similar to that of RSG1 in Fig. 7.2a. The design optimization used for this design follows the same optimization techniques described in Chapter 6. Fig. 7.15 indicates the pareto front with efficiency color-gradient distribution (red - maximum; blue - minimum) of SE-RSG. From these results we selected a maximum (Max) torque density design shown in Fig. 7.16a, the compromise design in Fig. 7.16b and the maximum power factor design in Fig. 7.16c. Where the compromise design is a design which does not necessarily have the best torque or best power factor but is still acceptable. The results of these three machines are given in Table 7.7. An important factor to note is that these designs are done to give an indication of how the smaller machine design of E-RSG would perform. Hence, as it can be seen in the performance results, the SE-RSGs do not meet the criteria set in the design optimization chapter. Therefore, in order to further achieve an optimum design, SE-RSG2, the designs of Fig. 7.16 would require further modifications. Such modifications may include rotor skewing, the use of multi-flux barriers (which might be a question due to the 72 slots but worth exploring) and rotor rib slitting. The latter would have a significant impact on the improvement of torque ripple and power factor.

Based on the findings in Table. 7.7, the maximum torque density design (SE-RSG1), a torque density of 11.68 Nm/m^3 is obtained. However, the subsequent power factor of less than 0.5 makes this design unsuitable for wind generator drives. The compromise design (SE-RSG2), with a power factor of 0.61 is deemed acceptable. Moreover, there is still an option to improve this based on the variations done for the larger machines which proved to have a significant impact on E-RSG as shown in this chapter.

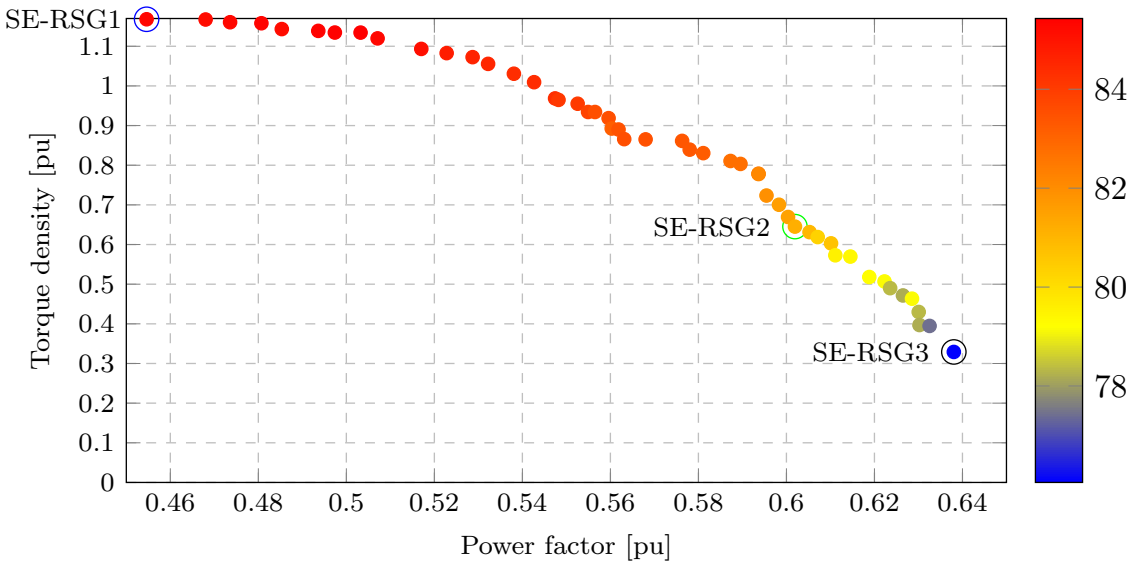

Figure (7.15) Pareto front with efficiency color-gradient distribution (red - maximum; blue - minimum) of SE-RSG.

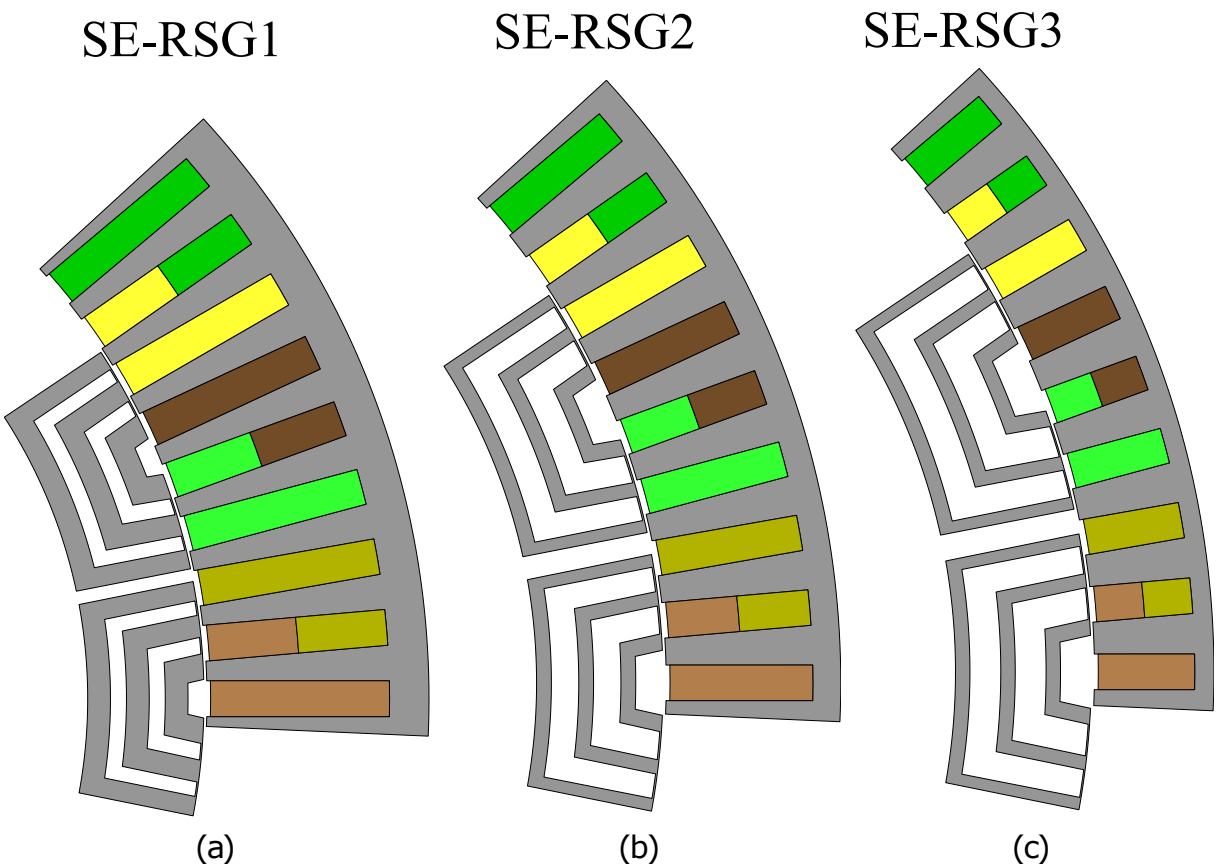

Figure (7.16) Cross- section of design optimized machine designed for (a) a maximum torque density, (b) Compromise design between torque density and power factor and (c) maximum power factor.

Table (7.7) Main Dimensions and Performance Results of Considered SE-RSG

Performance parameter	SE-RSG1	SE-RSG2	SE-RSG3
Power out [kW]	2.65	1.4	0.662
Power factor	0.45	0.61	0.64
Efficiency [%]	85.3	81.6	76.1
Torque average [Nm]	77.53	42.8	21.8
Torque density [kNm/m^3]	11.68	6.45	3.29
Torque ripple [%]	48	40	32
Current angle [°]	50.3	61.3	61.3
Current density [A/mm^2]	6	6	6
Fill factor	0.45	0.45	0.45
Stator diameter [mm]	260	260	260
Stack length [mm]	125	125	125
Air-gap [mm]	0.45	0.45	0.45
Speed [r/min]	375	375	375
Rotor core loss [W]	8.22	5.46	3.25
Stator core loss [W]	54.3	19.8	10.1
Total core loss [W]	62.52	25.3	13.3
$L_d - L_q$ [mH]	151	182	203.3
L_d/L_q	2.94	3.92	4.54

7.8. Chapter Summary

In this chapter, the design and optimization of a 16/72 and 16/120 epoxy-casted RSGs for medium speed wind generators are designed and analyzed on a 5-MW power level. The designs are done with a variation of six different rotor geometries in order to achieve the best optimum design that satisfied the set criteria in the design chapter. The design optimizations are carried out using *VisualDoc* and a multi-objective optimization algorithm, NSGA-II. Multiple rotor modifications are made including rotor rib slitting and multi flux barriers in order to obtain the optimal E-RSG design. Furthermore, the RSGs are verified using *ANSYS Maxwell* in order to confirm the results obtained in *SEMFEM*. The final design (RSG6) proved to reach all the design criteria set in the optimization chapter.

The design optimization of a 16/72 pole/slot medium-speed sub-2 kW E-RSG is done using the same optimization techniques described in Chapter 6. This is done as a representation to examine how a smaller scale to that of E-RSG would perform on a sub-100 Nm D-160 frame. The compromise design can still further be improved to reduce the high torque ripple obtained which is not acceptable for wind power applications. Furthermore, techniques to improve such a design can follow that of the above E-RSG designs to have an acceptable power factor and in turn improve the machine efficiency.

Chapter 8

Conclusions and recommendations

8.1. Conclusions

8.1.1. S-RSG and T-RSG Performance

With the aim of achieving very large (between 10 and 15 MW) medium-speed geared wind generators, a salient 16-pole, triple three-phase non-overlapping winding reluctance synchronous generator (RSG) is proposed and investigated in this thesis. The performance investigation is done (as proof of concept) on a sub-100 Nm torque level in a small D160 machine frame. From the performance results of a near-optimum generator design, the following conclusions are drawn.

The power factor performance of the classical single three-phase winding 16-pole RSG is found to be very poor at sub-0.3. This low power factor will significantly increase the cost of the drive converter and therefore will make this generator option unsuitable for wind generator drives.

To improve converter fault tolerance, the proposed triple converter-fed, triple three-phase winding 16-pole RSG was shown to have the best performance with a 20° phase shift in the phase currents of the three three-phase sets of the generator. This current phase shift was shown to theoretically cancel all sub-MMF as well as higher-order MMF harmonics in the machine.

The triple three-phase winding RSG with a 20° current phase shift shows a dramatic improvement in all aspects of performance compared to that of the single three-phase winding RSG. First, the torque density of the generator improves by 22% and the core losses reduce by 20%. The most significant improvements, however, are the almost doubling of the power factor and a 69% reduction in the torque ripple of the generator.

The power factor of 0.55 and the torque density of 6.5 kNm/m^3 of the proposed machine are reasonable, considering the small D160 frame-size, 16-pole machine. However, both these results are still on the low side and must be improved further by design optimization, and then evaluated on a large (10 to 15 MW) power level. The 7.5% torque ripple found for the unskewed proposed machine is very promising, considering that no special design effort such as complex rotor flux barriers was made to reduce it.

8.1.2. Epoxy-casted RSG (E-RSG) Performance

In an effort to further improve power factor and torque density, this thesis considered six further RSG structures in the design of a 5 MW, epoxy-casted rotor reluctance synchronous wind generator. Various modifications such as the use of a fractional slot winding, in combination with higher slot numbers, increased rotor flux barriers and rotor skewing, were made in order to achieve an optimum RSG that met the set criteria for large-power, high-pole number RSMs. Based on the findings, the following observations were made. Compared to the previous designs of [6] and [5] with equal volumes, the final epoxy-casted RSG design achieved a higher torque density with lower active mass. An acceptable power factor of 0.72, an efficiency 98.8%, and a torque density of 24 kNm/m^3 and were obtained, respectively, from the final optimized RSG design. These results are considered very good for a 16-pole RSM.

An acceptable torque ripple of 4.4% was achieved. Further improvement in the power factor was shown by means of rotor rib slitting. Finally, a mechanical feasibility study of the proposed epoxy-casted reluctance rotor verified the robustness of this type of rotor for large generator.

8.2. Recommendations

The following are some suggestions for potential areas of research that may be pursued as a result of this study:

1. To build and practically test the 16/18 pole/slot, sub-2 kW RSG (T-RSG) when power-fed by the triple three-phase converters.

2. Modify the 16/72 pole/slot, sub-2 kW epoxy-casted RSG (SE-RSG) according to the techniques described in Chapter 7. Find an optimum machine. Build and test the conceptual design.

3. Investigate the proposed epoxy-casted RSG (RSG6) using ferrite magnets (which are currently much cheaper than Neodymium magnets) in the rotor. This could potentially increase the power factor above 0.8.

4. Performance analysis and comparison of the optimum epoxy-casted RSG (RSG6) to other existing machine topologies such as the wound-field machines on the same volume.

Bibliography

[1] Y. Guo, H. Wang, and J. Lian, "Review of integrated installation technologies for offshore wind turbines: Current progress and future development trends," *Energy Conversion and Management*, vol. 255, p. 115319, 2022.

[2] J. Esch, "High-power wind energy conversion systems: State-of-the-art and emerging technologies," *Proceedings of the IEEE*, vol. 103, no. 5, pp. 736–739, 2015.

[3] IECRE, "V164-9.5 mw rotor nacelle assembly with rated output power of 9.525 mw and load modes down to 9.0 m," in *ECRE-IEC System for Certification to Standards Relating to Equipment for use in Renewable Energy Application*, 2018.

[4] P. Roshanfekr, S. Lundmark, T. Thiringer, and M. Alatalo, "A synchronous reluctance generator for a wind application-compared with an interior mounted permanent magnet synchronous generator," in *7th IET International Conference on Power Electronics, Machines and Drives (PEMD 2014)*. IET, 2014, pp. 1–5.

[5] E. Howard and M. J. Kamper, "Reluctance synchronous wind generator design optimisation in the megawatt, medium speed range," in *2017 IEEE Energy Conversion Congress and Exposition (ECCE)*. IEEE, 2017, pp. 1864–1871.

[6] J. Dippenaar and M. J. Kamper, "A robust 5 mw split-pole reluctance synchronous wind generator," in *2020 International Conference on Electrical Machines (ICEM)*, vol. 1. IEEE, 2020, pp. 1841–1847.

[7] A. Fratta, G. Troglia, A. Vagati, and F. Villata, "Evaluation of torque ripple in high performance synchronous reluctance machines," in *Conference Record of the 1993 IEEE Industry Applications Conference Twenty-Eighth IAS Annual Meeting*. IEEE, 1993, pp. 163–170.

[8] A. Vagati, "The synchronous reluctance solution: a new alternative in ac drives," in *Proceedings of IECON'94-20th Annual Conference of IEEE Industrial Electronics*, vol. 1. IEEE, 1994, pp. 1–13.

[9] T. Lipo, A. Vagati, L. Malesani, and T. Fukao, "Synchronous reluctance motors and drives," in *IEEE IAS*, vol. 92, 1992.

[10] G. Pellegrino, T. M. Jahns, N. Bianchi, W. L. Soong, and F. Cupertino, "The rediscovery of synchronous reluctance and ferrite permanent magnet motors: tutorial course notes," 2016.

[11] J. Kostko, "Polyphase reaction synchronous motors," *Journal of the American Institute of Electrical Engineers*, vol. 42, no. 11, pp. 1162–1168, 1923.

[12] E. Armando, P. Guglielmi, G. Pellegrino, M. Pastorelli, and A. Vagati, "Accurate modeling and performance analysis of ipm-pmasr motors," *IEEE Transactions on Industry Applications*, vol. 45, no. 1, pp. 123–130, 2009.

[13] M. Degano, M. Di Nardo, M. Galea, C. Gerada, and D. Gerada, "Global design optimization strategy of a synchronous reluctance machine for light electric vehicles," 2016.

[14] N. Bianchi, "Synchronous reluctance and interior permanent magnet motors," in *2013 IEEE Workshop on Electrical Machines Design, Control and Diagnosis (WEMDCD)*. IEEE, 2013, pp. 75–84.

[15] M. Gamba, G. Pellegrino, and F. Cupertino, "Optimal number of rotor parameters for the automatic design of synchronous reluctance machines," in *2014 international conference on electrical machines (ICEM)*. IEEE, 2014, pp. 1334–1340.

[16] M. Degano, E. Carraro, and N. Bianchi, "Selection criteria and robust optimization of a traction pm-assisted synchronous reluctance motor," *IEEE Transactions on Industry Applications*, vol. 51, no. 6, pp. 4383–4391, 2015.

[17] R. R. Moghaddam, F. Magnussen, and C. Sadarangani, "Theoretical and experimental reevaluation of synchronous reluctance machine," *IEEE Transactions on Industrial Electronics*, vol. 57, no. 1, pp. 6–13, 2009.

[18] G. Pellegrino, A. Vagati, P. Guglielmi, and B. Boazzo, "Performance comparison between surface-mounted and interior pm motor drives for electric vehicle application," *IEEE Transactions on Industrial Electronics*, vol. 59, no. 2, pp. 803–811, 2011.

[19] A. Vagati, M. Pastorelli, G. Francheschini, and S. C. Petrache, "Design of low-torque-ripple synchronous reluctance motors," *IEEE Transactions on industry applications*, vol. 34, no. 4, pp. 758–765, 1998.

[20] T. Matsuo and T. A. Lipo, "Rotor design optimization of synchronous reluctance machine," *IEEE Transactions on Energy Conversion*, vol. 9, no. 2, pp. 359–365, 1994.

[21] D. Staton, T. Miller, and S. Wood, "Maximising the saliency ratio of the synchronous reluctance motor," in *IEE Proceedings B (Electric Power Applications)*, vol. 140, no. 4. IET, 1993, pp. 249–259.

[22] G. Dajaku, S. Spas, X. Dajaku, and D. Gerling, "An improved fractional slot concentrated winding for low-poles induction machines," in *2016 XXII International Conference on Electrical Machines (ICEM)*. IEEE, 2016, pp. 114–119.

[23] K. S. Garner and M. J. Kamper, "Reducing mmf harmonics and core loss effect of non-overlap winding wound rotor synchronous machine (wrsm)," in *2017 IEEE Energy Conversion Congress and Exposition (ECCE)*. IEEE, 2017, pp. 1850–1856.

[24] L. Alberti and N. Bianchi, "Design and tests on a fractional-slot induction machine," in *2012 IEEE Energy Conversion Congress and Exposition (ECCE)*. IEEE, 2012, pp. 166–172.

[25] O. Moros, D. Gerling, and H. Schäfer, "New 30-teeth/14-poles concentrated winding for use in induction machines," in *4. Tagung Elektrische Antriebstechnologie für Hybrid-und Elektrofahrzeuge, Haus der Technik*, 2013, vol. 131, pp. 352–361.

[26] H.-J. Kim, D.-J. Kim, and J.-P. Hong, "Characteristic analysis for concentrated multiple-layer winding machine with optimum turn ratio," *IEEE transactions on magnetics*, vol. 50, no. 2, pp. 789–792, 2014.

[27] L. Alberti and N. Bianchi, "Theory and design of fractional-slot multilayer windings," *IEEE Transactions on Industry Applications*, vol. 49, no. 2, pp. 841–849, 2013.

[28] V. Dmitrievskii, V. Prakht, and V. Kazakbaev, "Ultra premium efficiency (IE5 energy-efficiency class) synchronous reluctance motor with fractional slot winding," in *2018 XIII International Conference on Electrical Machines (ICEM)*. IEEE, 2018, pp. 1015–1020.

[29] J. Jürgens, A. Brune, and B. Ponick, "Electromagnetic design and analysis of a salient-pole synchronous machine with tooth-coil windings for use as a wheel hub motor in an electric vehicle," in *2014 International Conference on Electrical Machines (ICEM)*. IEEE, 2014, pp. 744–750.

[30] J. Li, D.-W. Choi, D.-H. Son, and Y.-H. Cho, "Effects of mmf harmonics on rotor eddy-current losses for inner-rotor fractional slot axial flux permanent magnet synchronous machines," *IEEE Transactions on Magnetics*, vol. 48, no. 2, pp. 839–842, 2012.

[31] U. B. Akuru and M. J. Kamper, "Contemporary wind generators," in *2014 International Conference on the Eleventh industrial and Commercial Use of Energy*. IEEE, 2014, pp. 1–8.

[32] E. Aydin, "Determination of best drive train technology for future onshore wind turbines as a function of the output power," *Master's thesis, The Department of Electrical Engineering of the Eindhoven University of Technology*, 2013.

[33] S. Schmidt and A. Vath, "Comparison of existing medium-speed drive train concepts with a differential gearbox approach," *European Wind Energy Association*, pp. 179–186, 2012.

[34] S. Gerber, "Part 1: What is semfem?¶." [Online]. Available: http://www0.sun.ac.za/semfem/v3/tut_p1.html

[35] [Online]. Available: http://www.vrand.com/wp-content/uploads/2018/05/New-Features-in-VisualDOC-8.0.pdf

[36] W. T. Villet and M. J. Kamper, "Variable-gear EV reluctance synchronous motor drives—an evaluation of rotor structures for position-sensorless control," *IEEE Transactions on Industrial Electronics*, vol. 61, no. 10, pp. 5732–5740, 2013.

[37] J. H. Potgieter and M. J. Kamper, "Calculation methods and effects of end-winding inductance and permanent-magnet end flux on performance prediction of nonoverlap winding permanent-magnet machines," *IEEE Transactions on Industry Applications*, vol. 50, no. 4, pp. 2458–2466, 2013.

[38] M. J. Kamper, "Design optimisation of cageless flux barrier rotor reluctance synchronous machine," Ph.D. dissertation, Stellenbosch: Stellenbosch University, 1996.

[39] S. Gerber, J. Strauss, and P. Randewijk, "Evaluation of a hybrid finite element analysis package featuring dual air-gap elements," in *The XIX International Conference on Electrical Machines-ICEM 2010*. IEEE, 2010, pp. 1–6.

[40] X. B. Bomela and M. J. Kamper, "Effect of stator chording and rotor skewing on performance of reluctance synchronous machine," *IEEE Transactions on Industry Applications*, vol. 38, no. 1, pp. 91–100, 2002.

[41] G. N. Vanderplaats, "Numerical optimization techniques for engineering design, vanderplaats research & development," *Inc., Colorado Springs, CO*, p. 30, 1999.

[42] J. Sienz, M. Luege, and F. Fuerle, "Continuous optimization in aerospace structures," *Encyclopedia of Aerospace Engineering*, 2010.

[43] N. Bianchi and S. Bolognani, "Design optimisation of electric motors by genetic algorithms," *IEE Proceedings-Electric Power Applications*, vol. 145, no. 5, pp. 475–483, 1998.

[44] Y. Duan and D. M. Ionel, "A review of recent developments in electrical machine design optimization methods with a permanent-magnet synchronous motor benchmark study," *IEEE Transactions on Industry Applications*, vol. 49, no. 3, pp. 1268–1275, 2013.

[45] X. Wang, T. D. Strous, D. Lahaye, H. Polinder, and J. A. Ferreira, "Modeling and optimization of brushless doubly-fed induction machines using computationally efficient finite-element analysis," *IEEE Transactions on Industry Applications*, vol. 52, no. 6, pp. 4525–4534, 2016.

[46] U. B. Akuru and M. J. Kamper, "Formulation and multiobjective design optimization of wound-field flux switching machines for wind energy drives," *IEEE Transactions on Industrial Electronics*, vol. 65, no. 2, pp. 1828–1836, 2017.

[47] A. Tessarolo, F. Luise, P. Raffin, and V. Venuti, "Multi-objective design optimization of a surface permanent-magnet slotless alternator for small power wind generation," in *2011 International Conference on Clean Electrical Power (ICCEP)*. IEEE, 2011, pp. 371–376.

[48] Y. Del Valle, G. K. Venayagamoorthy, S. Mohagheghi, J.-C. Hernandez, and R. G. Harley, "Particle swarm optimization: basic concepts, variants and applications in power systems," *IEEE Transactions on evolutionary computation*, vol. 12, no. 2, pp. 171–195, 2008.

[49] K. Schittkowski, "The nonlinear programming method of wilson, han, and powell with an augmented lagrangian type line search function," *Numerische Mathematik*, vol. 38, no. 1, pp. 83–114, 1982.

[50] C. Singh and D. Sarkar, "Practical considerations in the optimisation of induction motor design," in *IEE Proceedings B (Electric Power Applications)*, vol. 139, no. 4. IET, 1992, pp. 365–373.

[51] D. F. Shanno, "Conditioning of quasi-newton methods for function minimization," *Mathematics of computation*, vol. 24, no. 111, pp. 647–656, 1970.

[52] M. J. Powell, "An efficient method for finding the minimum of a function of several variables without calculating derivatives," *The computer journal*, vol. 7, no. 2, pp. 155–162, 1964.

[53] M. Palmieri, M. Perta, F. Cupertino, and G. Pellegrino, "Effect of the numbers of slots and barriers on the optimal design of synchronous reluctance machines," in *2014 international conference on optimization of electrical and electronic equipment (OPTIM)*. IEEE, 2014, pp. 260–267.

[54] T. Hubert, M. Reinlein, A. Kremser, and H.-G. Herzog, "Torque ripple minimization of reluctance synchronous machines by continuous and discrete rotor skewing," in *2015 5th International Electric Drives Production Conference (EDPC)*. IEEE, 2015, pp. 1–7.

[55] R. Budynas and J. Nisbett, "Shigley's mechanical engineering design," *Mechanical Engineering*, vol. 1, p. 0904435, 2019.

[56] R. C. Hibbeler, *Statics and Mechanics of Materials, eBook*. Pearson Higher Ed, 2018.

[57] J. Marin, *Mechanical behavior of engineering materials*. Prentice-Hall, 1962.